Computational Study of the Structural Phase Transitions and Pressure Dependent Electronic Structure of ZnO

Mahlaga Phineas Molepo

A thesis submitted to the Faculty of Science,

University of the Witwatersrand,

in fulfilment of the requirements for the degree of

Doctor of Philosophy.

School of Physics,

University of the Witwatersrand,

Johannesburg.

May 2, 2012

Declaration

I declare that this thesis is my own, unaided work. It is being submitted for the Degree of Doctor of Philosophy at the University of the Witwatersrand, Johannesburg. It has not been submitted before for any degree or examination at any other University.

Mahlaga Phineas Molepo

$\underline{2^{nd}}$ day of MAY 2012

Abstract

We use first-principles calculations based on density functional theory to study the structural properties and pressure-induced solid-solid phase transitions of ZnO. Both the local-density approximation (LDA) and the PBE96 form of the generalized gradient approximation (GGA) are employed together with the projector augmented wave (PAW) method to mimic the electron-ion interaction. The electronic structure is investigated by the HSE hybrid functional and a partially self-consistent GW approximation. We consider the wurtzite (B4), rocksalt (B1), zinc blende (B3), CsCl (B2), PbO (B10), NaTl (B32), WC (B_h), BN (B_k), NiAs ($B8_1$) and AsTi (B_i) modifications of ZnO. The calculated structural properties in the B4, B3, B1 and B2 phases compare acceptably well with those found in previous theoretical studies, as is the transition pressure between them. We find that the B4 phase is the most preferred low-pressure candidate in ZnO while the B2 phase is favorable at high pressures. Apart from the previously reported B4→B1→B2 phase transition, our study reveals other possible paths for a transition from B4 to B2 phase with the B_k, B_h, B10, and $B8_1$ structures as intermediate phases. It is found that the HSE and the GW approach offer a significant improvement to the prediction of band-gaps in ZnO. The band-gaps are found to increase with increasing pressure leading to the structural phase transitions.

To all my grandparents

Acknowledgements

First and foremost, I would like to express my sincere gratitude to my supervisor Professor Daniel P. Joubert for introducing me to this exciting field of computational material physics. Thank you for your courageous support, guidance and a research project that was challenging and educative.

I would also like to acknowledge the financial support provided by South Africa's National Institute for Theoretical Physics (NITheP), National Research Foundation (NRF) and the University of the Witwatersrand.

The Center for High Performance Computing (CHPC) is acknowledged for providing a computational platform to perform some of the computations in this thesis.

I am grateful to my parents, brothers, the Molepo and Rachidi families for being my pillars of strength and greatest gift.

Special thanks to my colleagues Mohammed Suleiman and Faris Mohammed for their valuable assistance with python programming, and sharing the skill with me.

Last but not least, I thank all friends and colleagues in the School of Physics for the useful discussions and stress relieving jokes at hard times.

Publications

Part of this work has been published:

1. Mahlaga P. Molepo and Daniel P. Joubert, **Computational study of the structural phases of ZnO,** [*Phys. Rev. B* **84**, *094110 (2011)*].

The following papers are in preparation:

2. Pressure Dependence of the Band Gap of ZnO: A hybrid density functional Study.

3. Computational Study of the Pressure Dependent Electronic Structure of ZnO by GW Approach.

4. Structural Phases of ZnO: A hybrid density functional Study.

Contents

List of Figures

List of Tables

Chapter 1

Introduction

Zinc oxide (ZnO) is a group IIB - VIA semiconductor with a variety of technological applications including thin film-based electronic and electro-optic devices, chemical sensors, catalysts, and conductive solar cell window layers. The technological importance has been motivating detailed investigations of the structural and electronic properties of ZnO as well as application-oriented researches. There is also continuing interest in its high-pressure behavior in the areas of geophysics, condensed matter and materials physics [3, 4].

Most physical properties of solids virtually depend on structure and interatomic distances. Since application of pressure can vary these distances considerably more than, say, temperature, it provides an extremely powerful means of examining the relationship between structure and properties. This leads to a better insight and understanding of the underlying phenomena, and also an improved design of materials for technological applications. Pressure is a clean variable in a sense that it can induce large changes in structure and properties without altering the chemical composition or thermal energy of the system. This makes high-pressure systems particularly submissive to computational study. The studies of the pressure behavior of physical

properties of materials may provide an additional valuable information about these properties [5].

With recent progress in computational strategies and performance, computer simulations are increasingly used by theorists to understand properties of matter and make specific predictions for real materials and experimentally observable phenomena. This has been exploited by *ab initio* (first principles) simulations using density functional theory (DFT). The main merit of first principles calculations is their predictive power, as they demand little *a priori* experimental data. The advent of DFT and the invention of *ab initio* pseudopotentials have made it feasible to predict with a fair level of accuracy, ground state structural and electronic properties as well as pressure-induced structural phase transitions; even under extreme physical conditions which are not yet easily attainable in experimental laboratories.

In this study we perform first principles electronic structure calculations for different structures of ZnO. We consider the NaTl (B32), PbO (B10), WC (B_h), BN (B_k), NiAs ($B8_1$) and AsTi (B_i) modifications in addition to the previously studied [6, 7] wurtzite (B4), rocksalt (B1), zinc blende (B3) and CsCl (B2) structures. Crystal structures for these polymorphs are shown in appendix B. The objective is to predict the equilibrium structural and electronic properties including lattice parameters, bulk moduli, stabilities and density of states for these structures. We also predict the phase transitions between the structures and construct a detailed structural phase diagram for ZnO. This work is based on density functional theory within the local density and generalized gradient approximations (LDA and GGA).

Although methods such as LDA and GGA of DFT are well capable of determining accurately the aforementioned structural properties, DFT has its own challenges. One of the main problems is related to the character of the Kohn-Sham states. The band

structure obtained from Kohn-Sham eigenvalues cannot, in principle, be associated with quasiparticle addition and removal energies [8]. The errors in doing so tends to be systematic. The so-called band-gap problem of DFT is the best known example of such errors. This applies to semiconductors and insulators in which the band gap is severely underestimated. A more sophisticated method of improving the band gap involves addition of a certain amount of exact exchange to the DFT exchange, constructing a hybrid functional [9]. However, a viable alternative is to switch from the density functional theory to a many body approach such as the quasiparticle GW, a post DFT method pertinent for examination of the excited states in solids. The GW approach is used in this work to investigate the pressure behavior of the band gap in ZnO. Both these methods will be discussed in the later sections.

1.1 Synopsis

Based on above ultimate targets, this thesis is arranged as follows. Chapter 2 is devoted to a review of the theoretical framework upon which the main part of the thesis is based. In particular, a description of density functional theory with the most popular approximations of exchange correlation energy and hybrid density functionals has been given. Next in chapter 3, various methods of calculation used to solve the electron-ion interactions in solids are discussed, with emphasis on the projector augmented wave method as employed in this study. An outline of the basic calculations and background behind the desired properties of interest in this thesis is given in chapter 4. Chapter 5 is devoted to a description of the most successful method of approximation used to examine the excited states and electronic structure of the system under study. Chapter 6 focuses on the structural properties and the crystallographic phase transitions for the ZnO system under high pressure, based on the

theoretical techniques and methods described in chapters 2 and 3. An analysis of the pressure-dependent electronic structure of ZnO is presented in chapter 7, and comparison with results from other studies is made where possible. Finally, a summary and conclusions for this study are given in chapter 8.

Chapter 2

Density Functional Theory and Techniques

Density functional theory (DFT) is primarily a theory for investigating the electronic structure in condensed matter, and is increasingly important for quantitative studies of molecules and other finite systems. Like most quantum chemical approaches, the ultimate aim of DFT is the approximate solution of the many-body time-independent, Schrödinger equation for the electronic subsystem

$$\left\{ -\frac{\hbar^2}{2m} \sum_j \nabla_j^2 + \sum_j V_{ext}\left(\mathbf{r}_j\right) + \frac{1}{2} \sum_{j \neq i} \frac{e^2}{\mid \mathbf{r}_j - \mathbf{r}_i \mid} - E \right\} \Phi\left(\mathbf{r}_1, ...\mathbf{r}_N\right) = 0 \qquad (2.1)$$

where

$$V_{ext}\left(\mathbf{r}_j\right) = -\sum_i \frac{Z_i e^2}{\mid \mathbf{r}_j - \mathbf{R}_i \mid}, \qquad (2.2)$$

is the external potential acting on electron j, due to nuclei of charges Z_i. Here i and j denote the N electrons in the system, e is the charge of an electron while $\mathbf{R}_i$ and Z_i are the coordinates and atomic numbers of the nuclei. The first term of Eq. (2.1) in brackets describes the kinetic energy, while the second and third terms describe the electron-nucleus attraction and the electron-electron repulsion energies respectively [10, 11]. The electronic density distribution $n(\mathbf{r})$ and the total electronic energy E, for given locations $\mathbf{R}_i$ of the nuclei are the most important characteristics of the ground state electronic structure.

The electronic wavefunction Φ is a very complicated quantity that cannot be probed experimentally and that depends on $4N$ variables, i.e. three spatial variables and one spin variable for each of the N electrons. Thus, the main objective of DFT is to replace Φ and the associated Schrödinger equation by the electronic density as the basic variable. DFT has attracted the interest of physicists and chemists primarily for the following reasons [11]:

(*i*) The density $n(\mathbf{r})$, as a function of three variables is a much simpler quantity to deal with both conceptually and practically than the $4N$-dimensional wavefunction Φ.

(*ii*) Computational simplicity.

(*iii*) Its capability to handle infinite periodic systems (no N-dependence) and non-periodic systems of a large number of atoms.

2.1 The Thomas-Fermi Model

The Thomas-Fermi (TF) model developed by Thomas [12] and Fermi [13] in 1927 is a predecessor to density functional theory. They calculated the energy of an atom by representing the kinetic energy of a system of electrons as an explicit functional

of the electronic density, idealized as non-interacting electrons in a homogeneous gas with density equal to the local density at any given point and neglected exchange and correlation among the electrons. However, Dirac [14] in 1930, extended the TF model by formulating the local approximation for exchange still in use today. This leads to the energy functional for electrons in an external potential $v(\mathbf{r})$

$$\begin{aligned} E_{TFD}[n] &= C_1 \int d^3r n(\mathbf{r})^{(\frac{5}{3})} + \int d^3r V_{ext}(\mathbf{r}) n(\mathbf{r}) + C_2 \int d^3r n(\mathbf{r})^{(\frac{4}{3})} \\ &\quad + \frac{1}{2} \int d^3r d^3r' \frac{n(\mathbf{r}) n(\mathbf{r}')}{|\mathbf{r} - \mathbf{r}'|}, \end{aligned} \tag{2.3}$$

where the first term is the local approximation to the kinetic energy with $C_1 = \frac{3}{10}(3\pi^2)^{(\frac{2}{3})} = 2.871$ in atomic units, the third term is the local exchange with $C_2 = -\frac{3}{4}(\frac{3}{\pi})^{(\frac{1}{3})}$ and the last term is the classical electrostatic Hartree energy [15]. The functional $E[n]$ in Eq. (2.3) can be minimized for all possible $n(\mathbf{r})$ in order to find the ground state density and energy subject to a constant total number of electrons

$$\int d^3r n(\mathbf{r}) = N. \tag{2.4}$$

Using the method of Lagrange multipliers, the solution can be found by constrained minimization of the functional

$$\Omega_{TF}[n] = E_{TF}[n] - \mu \left\{ \int d^3r n(\mathbf{r}) - N \right\}, \tag{2.5}$$

where the Lagrange multiplier μ is the chemical potential. For small variations of the density $\delta n(\mathbf{r})$, the condition for a stationary point is

$$\int d^3r \left\{\Omega_{TF}\left[n\left(\mathbf{r}\right)+\delta n(\mathbf{r})\right]-\Omega_{TF}\left[n\left(\mathbf{r}\right)\right]\right\} \longrightarrow \int d^3r \left\{\frac{5}{3}C_1 n\left(\mathbf{r}\right)^{\frac{2}{3}}+V(\mathbf{r})-\mu\right\}\delta n(\mathbf{r})$$
$$= 0, \tag{2.6}$$

where $V(\mathbf{r}) = V_{ext}(\mathbf{r}) + V_{Hartree}\left(\mathbf{r}\right) + V_x\left(\mathbf{r}\right)$ is the total potential [15]. Since Eq. (2.6) must be satisfied for any function $\delta n(\mathbf{r})$ and then replacing C_1, it follows that the functional is stationary if and only if the density and potential satisfy the Thomas-Fermi relation

$$\frac{1}{2}\left(3\pi^2\right)^{\left(\frac{2}{3}\right)} n(\mathbf{r})^{\left(\frac{2}{3}\right)} + V(\mathbf{r}) - \mu = 0. \tag{2.7}$$

Although this was an important step, the Thomas-Fermi-Dirac theory remained rather inaccurate for most applications. The largest source of error was in the representation of the kinetic energy, followed by errors in the exchange energy, and due to the complete neglect of electron correlation. However it sets up the basis for the later developments of DFT, which has been the best choice for electronic structure calculations in condensed matter physics during the past three decades, and has also been accepted by quantum chemists because of its computational advantages as compared to traditional Hartree-Fock based methods.

2.2 Hohenberg-Kohn Theorems

Although DFT has its conceptual roots in the Thomas-Fermi model [12, 13], it was put on a firm theoretical footing by Hohenberg and Kohn (HK) in their seminal paper [16] of 1964. The two theorems proven in this paper are disarmingly simple

and almost trivial but they represent the major theoretical pillars on which all modern day density functional theories are erected.

The first HK theorem states that *for any system of interacting electrons in a general external potential* $V_{ext}(\mathbf{r})$, *the groundstate electron density* $n(\mathbf{r})$ *uniquely determines* $V_{ext}(\mathbf{r})$ *to within a constant:*

$$n(\mathbf{r}) \longrightarrow V_{ext}(\mathbf{r}). \tag{2.8}$$

The HK theorem applies to non-degenerate groundstates only. To prove this theorem, Hohenberg and Kohn began by considering two different external potentials $V_{ext}^{(1)}(\mathbf{r})$ and $V_{ext}^{(2)}(\mathbf{r})$ which differ by more than a constant but give the same groundstate density $n(\mathbf{r})$. These external potentials have the associated Hamiltonians, $\hat{H}^{(1)}$ and $\hat{H}^{(2)}$ with different groundstate wavefunctions, $\Phi^{(1)}$ and $\Phi^{(2)}$ which are hypothesized to have the same $n(\mathbf{r})$. Since $\Phi^{(2)}$ is not the ground state of $\hat{H}^{(1)}$, then by the Rayleigh Ritz variational principle

$$E^{(1)} = \langle \Phi^{(1)} \mid \hat{H}^{(1)}\Phi^{(1)} \rangle < \langle \Phi^{(2)} \mid \hat{H}^{(1)}\Phi^{(2)} \rangle \tag{2.9}$$

where

$$\langle \Phi^{(2)} \mid \hat{H}^{(1)}\Phi^{(2)} \rangle = \langle \Phi^{(2)} \mid \hat{H}^{(2)}\Phi^{(2)} \rangle + \int d^3r [V_{ext}^{(1)}(\mathbf{r}) - V_{ext}^{(2)}(\mathbf{r})] n(\mathbf{r}), \tag{2.10}$$

so that

$$E^{(1)} < E^{(2)} + \int d^3r [V_{ext}^{(1)}(\mathbf{r}) - V_{ext}^{(2)}(\mathbf{r})] n(\mathbf{r}). \tag{2.11}$$

The strict inequality follows for all non-degenerate groundstates from the variational

principle. Similarly, on considering $E^{(2)}$,

$$E^{(2)} < E^{(1)} + \int d^3r[V_{ext}^{(2)}(\mathbf{r}) - V_{ext}^{(1)}(\mathbf{r})]n(\mathbf{r}). \tag{2.12}$$

Adding the inequalities (2.11) and (2.12) gives the contradictory inequality

$$E^{(1)} + E^{(2)} < E^{(1)} + E^{(2)}, \tag{2.13}$$

hence the desired result is established: there cannot be two different external potentials differing by more than a constant that yield the same non-degenerate ground state electron density. Therefore the density uniquely determines the external potential to within a physically irrelevant additive constant [11, 15].

Despite the appeal of this result, it is clear from the above reasoning that at this level no prescription has been given to solve the many-particle problem in the presence of $V_{ext}(\mathbf{r})$. However, this HK theorem provided confidence that it is sensible to seek prescriptions for many-particle physics based on the density rather than the complicated wavefunction.

In the second theorem, HK showed that there exists a universal functional $F_{HK}[n]$ such that, for a given external potential $V_{ext}(\mathbf{r})$, the actual ground state energy E and density $n(\mathbf{r})$ are obtained by minimizing the energy functional

$$E[n] = F_{HK}[n] + \int d^3r V_{ext}(\mathbf{r})n(\mathbf{r}) \tag{2.14}$$

with respect to variations in electron density subject to the constraint of constant number of electrons

$$N = \int d^3r n(\mathbf{r}). \tag{2.15}$$

in the system. The functional $F_{HK}[n]$ in Eq. (2.14) includes all the internal energies, kinetic ($T[n]$) and potential ($E_{int}[n]$), of the interacting electron system and must be universal (i.e. same for all electron systems), independent of the external potential

$$F_{HK}[n] = T[n] + E_{int}[n]. \tag{2.16}$$

Here, HK considered a system with the ground state density $n_0[\mathbf{r}]$ associated with an external potential $V_{ext}(\mathbf{r})$. The HK functional for this system is equal to the expectation value of the Hamiltonian $\hat{H}$ in the unique ground state, which has the wavefunction Φ

$$E_0 = E_{HK}[n_0] = \langle \Phi \mid \hat{H}\Phi \rangle. \tag{2.17}$$

On considering a different trial density $n'(\mathbf{r})$, which necessarily corresponds to a different wavefunction Φ'; it follows that the energy E' of this state is greater than E_0, since

$$E_0 = \langle \Phi \mid \hat{H}\Phi \rangle \leq \langle \Phi' \mid \hat{H}\Phi' \rangle = E' \tag{2.18}$$

with $\hat{H} = \hat{T} + \hat{V} + \hat{U}$, so that

$$E_0 \leq \langle \Phi' \mid \left(\hat{T} + \hat{V} + \hat{U}\right) \Phi' \rangle = E', \tag{2.19}$$

where $\hat{T}$, $\hat{V}$ and $\hat{U}$ are the kinetic energy, external potential and interaction energy operators respectively. Thus the energy given by Eq. (2.14) for the correct ground state $n_0[\mathbf{r}]$ is indeed lower than the value of this expression evaluated for any other trial density $n'(\mathbf{r})$ [15]. The equality sign holds only if Φ'=Φ**.** This result means that the exact ground state density and energy would be found by minimizing the total

energy (Eq. (2.14)) of the system with respect to variation in the density function $n(\mathbf{r})$, provided the functional $F_{HK}[n]$ was known. Unfortunately, the HK theorems do not provide any guidance at all how this functional that delivers the ground state energy should be constructed. Moreover, they apply to non-degenerate states only. However, these theorems remain the major pillars of modern DFT [17]. An alternative and improved definition of the functional F was given by Levy [18] and Lieb [19] and that is the subject of the next section.

2.3 The Constrained Search Approach

Following the idea of Levy and Lieb (LL) [18,19], one first considers the energy of the class of many-particle wavefunctions Φ that give rise to the same density $n(\mathbf{r})$. For any wavefunction, the total energy can be written as

$$E = \langle \Phi \mid (\hat{T} + \hat{U})\Phi \rangle + \int d^3 r V_{ext}(\mathbf{r}) n(\mathbf{r}). \tag{2.20}$$

On minimizing this energy over that particular class of wavefunctions with the same density, a unique lowest energy for that density can be defined

$$E_{LL} = \min_{\Phi \to n(\mathbf{r})} \langle \Phi \mid (\hat{T} + \hat{U})\Phi \rangle + \int d^3 r V_{ext}(\mathbf{r}) n(\mathbf{r})$$

$$\equiv F_{LL}[n] + \int d^3 r V_{ext}(\mathbf{r}) n(\mathbf{r}), \tag{2.21}$$

where

$$F_{LL}[n] = \min_{\Phi \to n(\mathbf{r})} \langle \Phi \mid \left(\hat{T} + \hat{U}\right) \Phi \rangle \tag{2.22}$$

defines the Levy-Lieb functional.

Thus Eq. (2.22) clarifies the meaning of a functional and provides a way to make an operational definition: *the minimum of the sum of kinetic plus interaction energies for all possible wavefunctions having the same density* $n(\mathbf{r})$ [15]. It is worth noting that the HK definition of the functional (Eq. (2.14)) applies only to ground state densities that can be generated by some external potential; this is called "*V-representability*". In contrast, the LL definition (Eq. (2.22)) applies to a broader class of densities derivable from a wavefunction Φ_N for N electrons including degenerate states. This is termed "*N-representability*" [17]. Despite its elegance in appearance and strength in formal power, the constrained-search approach, like the HK theorems does not give any method to find the functional.

2.4 The Kohn-Sham Approach

In the year following the 1964 seminal paper of Hohenberg and Kohn, Kohn and Sham [20] provided a procedure by which we can approximate the functional and hence solve for the ground state energy and density. Kohn and Sham suggested a single-particle kinetic energy functional $T_s[n]$, which is the kinetic energy of *non-interacting* electrons (i.e. electron-electron interactions turned off) in their ground state under the effect of an external potential such that their ground state density is $n(\mathbf{r})$. If $\psi_i(\mathbf{r})$ are the single-particle eigenfunctions of this single-particle external potential then $n(\mathbf{r})$ is defined as

$$n(\mathbf{r}) = \sum_{i=1}^{N} |\psi_i(\mathbf{r})|^2 , \tag{2.23}$$

and

$$T_s[n] = \sum_{i=1}^{N} \int d^3r \frac{\hbar^2}{2m} \left|\nabla \psi_i(\mathbf{r})\right|^2 . \tag{2.24}$$

This is not the true kinetic energy $\left\langle \hat{T} \right\rangle$ of an interacting system whose ground state density is $n(\mathbf{r})$, but in the final optimized description it is much closer to $\left\langle \hat{T} \right\rangle$ than the Thomas-Fermi kinetic energy is [21]. It was shown [20] that the energy functional $E[n]$ (Eq. (2.14)) can be written as the sum of large external potential energy, single-particle kinetic energy and Hartree potential energy terms, plus a remainder E_{xc}:

$$E\left[n\right] = \int V_{ext}\left(\mathbf{r}\right) n\left(\mathbf{r}\right) d^3r + \langle \Phi \mid T_s[n] \mid \Phi \rangle + \frac{e^2}{2} \int \frac{n\left(\mathbf{r}\right) n\left(\mathbf{r}'\right)}{\mid \mathbf{r} - \mathbf{r}' \mid} d^3r d^3r' + E_{xc}\left[n\right]. \tag{2.25}$$

E_{xc} is termed the exchange-correlation energy, which includes the physical effects of a potential and a kinetic character:

$$E_{xc}\left[n\right] = \langle \Psi \mid \hat{T} + \hat{V} \mid \Psi \rangle - \langle \Phi \mid \hat{T} + \hat{V} \mid \Phi \rangle. \tag{2.26}$$

Here, Ψ is the interacting groundstate wavefunction which yields the density and Φ is the non-interacting Kohn-Sham wavefunction for the density. The single particle eigenfunctions in Eq. (2.24) must satisfy the famous Kohn-Sham equations [20, 22]:

$$\left[-\frac{\hbar^2}{2m} \nabla^2 + v_{eff}\left(\mathbf{r}\right) \right] \psi_i(\mathbf{r}) = \epsilon_i \psi_i(\mathbf{r}), \tag{2.27}$$

where ϵ_i is a Lagrange multiplier ensuring normalization. The effective one-electron potential comprises external, Hartree and exchange-correlation terms:

$$v_{eff}\left(\mathbf{r}\right) = v\left(\mathbf{r}\right) + e^2 \int \frac{n\left(\mathbf{r}'\right)}{\mid \mathbf{r} - \mathbf{r}' \mid} d^3r' + v_{xc}\left(\mathbf{r}\right) \tag{2.28}$$

where the exchange-correlation potential, v_{xc}, is given formally by the functional derivative

$$v_{xc}(\mathbf{r}) = \frac{\delta E_{xc}}{\delta n(\mathbf{r})}. \tag{2.29}$$

The Kohn-Sham equations represent a mapping of the interacting many-electron system onto a system of non-interacting electrons moving in an electron potential due to all other electrons [1]. Thus, Kohn and Sham provided a recipe for solving the ground state energy of a many-body electron system within an effective one-electron framework provided the exchange and correlation functional is known. The major challenge within DFT is that the exact functional for exchange and correlation $E_{xc}[n]$ is unknown except for the free electron gas. This, however, is only a small contribution to the total electron energy [23]. There are different types of approximations involved in a DFT calculation for the unknown $E_{xc}[n]$ functional. The successful and widely used approximations are the local density and the generalized gradient, and these we present in the next two sections respectively. In addition, we present in the last section, hybrid functionals that contains an admixture of Hartree-Fock energy and DFT energy in the exchange part of the exchange-correlation functional.

2.5 Local Density Approximation

The Local Density Approximation (LDA) (or more generally the Local Spin Density Approximation (LSDA)), proposed by Kohn and Sham is the basis of all the approximate exchange-correlation functionals and hence the most widely used approximation in physics. The E_{xc} is calculated assuming that in the vicinity of the point $\mathbf{r}$ the properties of the inhomogeneous electron gas of density $n(\mathbf{r})$ can be ap-

proximated by those of a *uniform electron gas* of that density. This is a system in which electrons move on a positive background charge distribution such that the total ensemble is electrically neutral [10, 17]. The number of electrons N as well as the volume V of the gas are considered to approach infinity, while the electron density, i.e., N/V remains finite, and is uniform or constant over space. Accordingly, within the LDA the exchange-correlation energy is expressed as

$$E_{xc} \approx E_{xc}^{LDA} = \int n(\mathbf{r})\epsilon_{xc}[n(\mathbf{r})]d^3r, \tag{2.30}$$

where ϵ_{xc} indicates the exchange and correlation energy per particle of a uniform electron gas calculated at the local density. The corresponding exchange-correlation potential of Eq. (2.28) then becomes

$$v_{xc}^{LDA}(\mathbf{r}) = \frac{\delta E_{xc}^{LDA}}{\delta n(\mathbf{r})} = \epsilon_{xc}[n(\mathbf{r})] + n(\mathbf{r})\frac{\partial \epsilon_{xc}(n)}{\partial n}. \tag{2.31}$$

The function $\epsilon_{xc}(n)$ can be divided into exchange and correlation energy contributions,

$$\epsilon_{xc}(n) = \epsilon_x(n) + \epsilon_c(n). \tag{2.32}$$

The exchange part is already known, given by the Dirac exchange-energy functional [14],

$$\epsilon_x(n) = C_x n(\mathbf{r})^{1/3}, \tag{2.33}$$

with $C_x = -\frac{3}{4}(\frac{3}{\pi})^{1/3}$ in atomic units ($a.u.$), so that

$$\epsilon_x(n) = -\frac{3}{4}\sqrt[3]{\frac{3n(\mathbf{r})}{\pi}}. \tag{2.34}$$

The correlation energy ϵ_c has been calculated to great accuracy by Ceperly and Alder [24] with Quantum Monte Carlo simulations of the uniform electron gas. Expressions for the energy correlation of the uniform electron gas are known only in extreme limits of high and low densities. In the high-density limit ($r_s \to 0$), also known as the weak-coupling limit, the correlation energy is expressed as

$$\epsilon_c(n) = c_0 \ln r_s - c_1 + c_2 r_s \ln r_s + \ldots \quad (r_s \to 0) \tag{2.35}$$

from many-body pertubation theory. The parameter r_s introduced here is the radius of a sphere with constant charge density and a total charge of one electron, also known as the Wigner-Seitz radius. The constants $c_0 = 0.031091$ and $c_1 = 0.046644$ are known. For the low-density ($r_s \to \infty$) limit, also known as the strong coupling limit:

$$\epsilon_c(n) = -\frac{d_0}{r_s} + \frac{d_1}{r_s^{3/2}} + \ldots \quad (r_s \to \infty). \tag{2.36}$$

The constants d_0 and d_1 in Eq. (2.36) can be estimated from the Madelung electrostatic and zero-point vibrational energies of the Wigner crystal, respectively [11, 25, 26]. It was shown by Perdew and Wang [27] that both limits (2.35) and (2.36) are embraced by the expression:

$$\epsilon_c(n) = -2c_0(1+\alpha_1 r_s) \ln \left[1 + \frac{1}{2c_0\left(\beta_1 r_s^{1/2} + \beta_2 r_s + \beta_3 r_s^{3/2} + \beta_4 r_s^2\right)} \right] \tag{2.37}$$

where

$$\beta_1 = \frac{1}{2c_0}\exp(-\frac{c_1}{2c_0}), \quad \beta_2 = 2c_0\beta_1^2 \tag{2.38}$$

in Hartree units. The coefficients $\alpha_1 = 0.21370$, $\beta_3 = 1.6382$, and $\beta_4 = 0.49294$ were found by fitting to accurate Quantum Monte Carlo correlation energies of Ceperly and Alder [24] for $r_s = 2$, 5, 10, 20, 50, and 100 in units of Bohr radii.

The LSDA is thus a first-principles approximation in the sense that its parameters are not fitted empirically to calculated or experimental results for any system other than the one in which its form is exact. It is by construction, exact for a uniform system, and a good approximation for systems of slowly-varying density. However, the LSDA also provides moderate accuracy for real electronic systems of rapidly-varying densities, which are beyond its obvious range of validity. For four decades after its proposal, it remains a popular approximation for realistic solid-state calculations, although it seriously overestimates the atomization energies of molecules and solids [21]. Despite its limited accuracy, the LSDA's reliability in calculations is attributed to its first-principles character and that it obeys the correct sum rule for the exchange-correlation hole, which together permit a controlled extrapolation from a system of slowly-varying electron density to any real electronic system [1].

2.6 Generalized Gradient Approximation

Many attempts have been made to improve upon the accuracy of LSDA. The logical first step in that direction was the suggestion of using not only the information about the density at a particular coordinate $\mathbf{r}$ but to supplement the density with information about the *gradient* of the charge density, $\nabla n(\mathbf{r})$ in order to account for the non-homogeneity of the true electron density [17]. The gradient expansion approxi-

mation (GEA) suggested in the original work of Kohn and Sham [20] was found by considering the LSDA as the first term of a Taylor expansion of the $E_{xc}[n_\uparrow, n_\downarrow]$ about the uniform density, and adding corrections to the next term in the density gradients. However, the GEA does not lead to consistent improvements over the LSDA as it violates the sum rules and other relevant conditions and, is actually often less accurate than LSDA [28, 29]. The basic problem is that gradients in real materials are so large that the expansion breaks down [15].

A variety of remedies called *generalized-gradient approximations* (GGA's) have been proposed for functions that modify the behavior of large gradients such that the desired properties are preserved. The basic idea of GGA's is to express the exchange-correlation energy in the form

$$E_{xc}^{GGA}[n_\uparrow, n_\downarrow] = \int d^3r f\left(n_\uparrow(\mathbf{r}), n_\downarrow(\mathbf{r}), \nabla n_\uparrow(\mathbf{r}), \nabla n_\downarrow(\mathbf{r})\right) \tag{2.39}$$

where the function f is chosen by some set of criteria. Like the ϵ_{xc}^{unif} of Eq. (2.30), f must be a parametrized analytic function, in order to facilitate practical applications. In comparison with LSDA, GGA's greatly advance the accuracy, especially for molecular binding energies [30], which are severely overestimated by LSDA. In the solid state, the GGA's expand and soften bonds, leading to larger lattice constants that are sometimes more and sometimes less accurate than those of LSDA [21]. Typically, GGA's favor density inhomogeneity more than LSDA does.

A first-principles numerical GGA has been constructed [31] by starting from the second-order density-gradient expansion for the exchange correlation hole surrounding an electron in a system of slowly varying density, then cutting off its spurious long-range parts to satisfy sum rules on the exact hole that the LSDA respects. An analytic fit to this numerical GGA is the functional proposed in 1991 by Perdew and Wang

(PW91) [27], designed to satisfy several other exact conditions. Although PW91 functional incorporates some density inhomogeneity while retaining many of the best features of LSDA, its own shortcomings are well documented [31]: This concerns in particular (i) a long derivation that depends on a mass of detail, (ii) a complicated, nontransparent and overparameterized analytic function f, (iii) its parameters are not seamlessly meshed [32] and they lead to spurious wiggles in the exchange-correlation potential, (iv) PW91 does not behave properly under Levy's uniform scaling to the high density limit while the numerical GGA correlation energy functional does, and (v) it describes the linear response of a uniform electron gas density less satisfactorily than does LSDA [33,34]. This problem arises because PW91 reduces to second-order gradient expansion for either small *or* slow density variations, and it illustrates that the semilocal form of Eq. (2.39) is too restrictive to reproduce all the known behaviors of the exact functional [31].

The GGA form employed in this thesis is due to Perdew, Burke and Ernzerhof (PBE) [35]. They solve the PW91 problems above with a simplified construction of a simplified GGA for exchange and correlation in which all parameters (other than those in LSDA) are fundamental constants. In their derivation, the GGA correlation function is written in the form

$$E_c^{PBE}[n_\uparrow, n_\downarrow] = \int d^3r n \left[\epsilon_c^{unif}(r_s, \zeta) + H^{PBE}(r_s, \zeta, t)\right] \tag{2.40}$$

where $r_s = (3/4\pi n)^{1/3}$ is the local Wigner-Seitz radius, $\zeta = (n_\uparrow - n_\downarrow)/n$ is the relative spin polarization and $t = |\nabla n|/2\phi k_s n$ is a dimensionless density gradient. Here $\phi(\zeta) = \frac{1}{2}\left[(1+\zeta)^{2/3} + (1-\zeta)^{2/3}\right]$ is a spin-scaling factor and $k_s = (4k_F/\pi a_0)^{1/2}$ is the TF screening wave number, with $a_0 = \hbar^2/me^2$. The gradient contribution H^{PBE} is defined as

$$H^{PBE} = \left(e^2/a_0\right)\gamma\phi^3 \ln\left\{1 + \frac{\beta}{\gamma}t^2\left[\frac{1+At^2}{1+At^2+A^2t^4}\right]\right\} \tag{2.41}$$

where

$$A = \frac{\beta}{\gamma}\left[\exp\left\{-\epsilon_c^{unif}/\left(\gamma\phi^3 e^2/a_0\right)\right\} - 1\right]^{-1}, \tag{2.42}$$

and H^{PBE} satisfies the following three conditions [35]:

(i) It tends to the correct second-order gradient expansion in the slowly varying limit $(t \longrightarrow 0)$

$$H^{PBE} \longrightarrow (e^2/a_0)\beta\phi^3 t^2, \tag{2.43}$$

where $\beta = 0.066725$.

(ii) It approaches minus the uniform electron gas correlation in the rapidly varying limit $(t \longrightarrow \infty)$,

$$H^{PBE} \longrightarrow -\epsilon_c^{unif}, \tag{2.44}$$

thus making the correlation energy vanish. This result from the correlation hole sum rule.

(iii) It must cancel the logarithmic singularity of ϵ_c^{unif} in the high-density limit, thus forcing the correlation energy to scale to a constant under uniform scaling to the high density limit.

Under uniform scaling to the high density limit, E_c^{PBE} tends to

$$-\frac{e^2}{a_0}\int d^3r n\gamma\phi^3 \ln\left[1 + \frac{1}{\chi s^2/\phi^2 + \left(\chi s^2/\phi^2\right)^2}\right] \tag{2.45}$$

where $s = |\nabla n| / 2k_F n = (r_s/a_0)^{1/2} \phi t/c$ is another dimensionless density gradient, $c = (3\pi^2/16)^{1/3} \simeq 1.2277$, and $\chi = (\beta/\gamma) c^2 \exp(-\omega/\gamma) \simeq 0.72161$.

The exchange energy E_x^{PBE} on the other hand is derived from four further conditions [35]:

(iv) E_x^{PBE} satisfies the uniform scaling condition such that for $\zeta = 0$, we have

$$E_x^{PBE} = \int d^3 r n \epsilon_x^{unif}(n) F_x(s), \tag{2.46}$$

where $\epsilon_x^{unif} = -3e^2 k_F/4\pi$ and $F_x(s)$ is the enhancement factor over local exchange, given by

$$F_x(s) = 1 + \kappa - \kappa/\left(1 + \mu s^2/\kappa\right). \tag{2.47}$$

The correct uniform gas limit is recovered when $F_x(0) = 1$.

(v) It obeys the spin-scaling relationship

$$E_x^{PBE}[n_\uparrow, n_\downarrow] = \frac{1}{2}\left(E_x[2n_\uparrow] + E_x[2n_\downarrow]\right). \tag{2.48}$$

(vi) It recovers the LSDA linear response limit, where

$$F_x(s) = 1 + \mu s^2 \tag{2.49}$$

with $\mu = \beta(\pi^2/3) \simeq 0.21951$.

(vii) It satisfies the local Lieb-Oxford bound [36],

$$\begin{aligned} E_x[n_\uparrow, n_\downarrow] &\geq E_{xc}[n_\uparrow, n_\downarrow] \\ &\geq -1.679e^2 \int d^3r n^{4/3} \end{aligned} \tag{2.50}$$

if $F_x(s) \leq 1.804$, where the value of $\kappa = 0.804$ in Eq. (2.47).

In the PBE GGA, the correct features of LSDA are retained and supplemented with the most energetically important features of gradient-corrected nonlocality. Some features of PW91 are considered less important and have been sacrificed here. These are (1) correct second-order gradient coefficients for E_x and E_c in the slowly varying limit, and (2) correct nonuniform scaling of E_x in limits where the reduced gradient s tends to infinity. It is also shown in Ref: [35], by calculations of atomization energies for small molecules, that the PBE functional yields essentially the same results as the PW91. Therefore PBE is close to PW91, except for its additional satisfaction of conditions (*iii*) and (*vi*) and its smoother potential. However, its simpler form and derivation makes it easier to understand and apply. We will see in chapter 6 that the PBE exchange-correlation yields accurate structural properties for the ZnO-phase system.

2.7 Shortcomings of LDA/GGA

Although the LDA and GGA remain the most popular methods for predicting the structural, electronic, and vibrational properties for solids in DFT, they often fail to describe systems with strongly localized d or f electrons. This failure is mainly attributed to an incomplete cancellation of the artificial Hartree self-interaction and the lack of integer discontinuity in the exchange and correlation energy upon adding

an electron. As a result, the Kohn-Sham single-particle eigenvalue band gap severely underestimates the measured quasiparticle band gaps, in particular for semiconductors and insulators. In addition, these approximations underestimate the binding energy of the localized d and f states. These states are predicted to be too delocalized and their hybridization with the anion p-derived valence states is overestimated. An alternative to the standard DFT exchange correlation functionals are the hybrid density functionals, described in the next section.

2.8 Hybrid Functionals

Hybrid functionals are a class of approximations to the exchange-correlation energy functional, that incorporates certain amounts of non-local Hartree-Fock (HF) exact exchange and local or semilocal DFT exchange energy. The construction of hybrid functionals was motivated by the complementary deficiencies of DFT and HF. For instance, band gaps predicted by DFT are too narrow, while HF predicts far too wide band gaps relative to experiment. Thus, there has been some hope that a mixture of the two methods may not only predict more accurate band gaps, but also lead to more accurate total energies, bond lengths, and vibrational frequencies [37].

2.8.1 Semiempirical hybrid functionals

The mixture of HF and DFT exchange energies is justified by the *ab initio* adiabatic connection formula (ACF) [38–40] for the correlation energy E_{xc} of Kohn-Sham (KS) DFT, conveniently expressed as

$$E_{xc} = \int_0^1 U_{xc}^{\lambda} d\lambda, \tag{2.51}$$

where λ is an interelectronic coupling strength parameter that effectively couples the interaction strength to the magnitude of the electronic charge, ($e^2 \rightarrow \lambda e^2$). U_{xc}^{λ} is the exchange correlation potential energy at intermediate coupling strength λ [41]. The adiabatic connection procedure literally connects the real interacting system (defined by $\lambda = 1$) to the noninteracting KS reference system ($\lambda = 0$). This is done through a continuum of partially interacting systems ($0 \leq \lambda \leq 1$) whilst keeping the density $n(\mathbf{r})$ fixed, hence the reason for the term "adiabatic". The λ dependence of the ACF (Eq. (2.51)) can be simply approximated by a linear interpolation resulting in

$$E_{xc} = \frac{1}{2}U_{xc}^{0} + \frac{1}{2}U_{xc}^{1}, \tag{2.52}$$

where U_{xc}^{0} and U_{xc}^{1} are the exchange-correlation potential energies of the KS reference system and the fully interacting system respectively.

Becke [9] argued convincingly that U_{xc}^{0} is the pure exchange energy of the KS slater determinant without any dynamic correlation and should be evaluated exactly. This is essentially the conventional HF exchange energy, though not exactly equal in value. On the other hand ($\lambda = 1$), Becke proposed that U_{xc}^{1} can be estimated by a LSDA

$$U_{xc}^{1} \simeq U_{xc}^{LSDA} = \int U_{xc}\left[n_{\uparrow}(\mathbf{r}), n_{\downarrow}(\mathbf{r})\right] d^{3}r, \tag{2.53}$$

resembling the conventional LSDA (Eq. (2.30)), but involving the exchange-correlation potential instead of total energy. Considering these arguments, Becke introduced the first HF/DFT hybrid scheme [9] known as the 'half-and-half' functional

$$E_{xc} = \frac{1}{2}E_x + \frac{1}{2}U_{xc}^{LSDA}, \tag{2.54}$$

which approximates Eq. (2.51) as the average of exact-exchange energy at $\lambda = 0$ and the LSDA for exchange-correlation potential energy at $\lambda = 1$.

Subsequently, this led to construction of three-parameter hybrid functionals [42] of the form

$$E_{xc} = E_{xc}^{LSDA} + a_0(E_x^{exact} - E_x^{LSDA}) + a_x\Delta E_x^{B88} + a_c\Delta E_c^{PW91}, \tag{2.55}$$

where $E_x^{exact}$is the exact exchange energy, ΔE_x^{B88} is Becke's 1988 gradient correction [43] for exchange, and ΔE_c^{PW91} is the 1991 gradient correction for correlation energy of Perdew and Wang [27]. The mixing coefficients where determined by a linear least-squares fit to the atomization energies, ionization potentials, proton affinities, and atomic energies taken from Pople's G2 test set [44], resulting in optimum values $a_0 = 0.20$, $a_x = 0.72$,and $a_c = 0.81$. Functionals of this form are therefore semiempirical.

The B3LYP functional

Becke's three-parameter Lee-Yang-Parr (B3LYP) functional [42, 45, 46] is the most popular hybrid to date. The B3LYP implementation in VASP code [37, 47] follows the formal structure of Eq. (2.55), defined as:

$$E_{xc}^{B3LYP} = 0.8E_x^{LDA} + 0.2E_x^{HF} + 0.72\Delta E_x^{B88} + 0.19E_c^{VWN3} + 0.81E_c^{LYP}. \tag{2.56}$$

Here 80% of LDA exchange is mixed with 20% of HF exchange energy and 72% of Becke's gradient correction ΔE_x^{B88} is added. In the correlation part, 81% of of the

semi-local Lee_Yang-Parr (LYP) [45] correlation energy is used. The remaining 19% of the local correlation energy is added from from the Vosko-Wilk-Nusair correlation functional III (VWN3) [48]. This is fitted to the correlation energy in the random phase approximation of the homogeneous electron gas. Despite being one of the most popular semiempirical hybrid functionals, the B3LYP functional fails to obtain the homogeneous electron gas limit [47].

2.8.2 Parameter-free Hybrid Functionals

Efforts to reduce the degree of empiricism in Becke's hybrid functionals were made by Ernzerhof and co-workers [49–51]. Hybrid functionals such as PBE0 [52, 53] and the recently developed HSE03 [54,55], which reproduce the homogeneous electron gas limit are motivated by their work. Contrary to Becke's functionals, these functionals do not contain any empirical parameters fitted to specific properties, and are widely applicable both to solid state physics as well as to quantum chemistry.

The PBE0 functional

The "parameter-free" PBE0 hybrid functional is constructed by mixing 25% of exact HF exchange energy with 75% of the popular PBE GGA [35] exchange. The correlation part of the PBE functional is completely used to describe the electron correlation energy. The resulting exchange correlation energy then assumes the following form:

$$E_{xc}^{PBE0} = \frac{1}{4}E_x + \frac{3}{4}E_x^{PBE} + E_c^{PBE}, \tag{2.57}$$

where the mixing coefficient ($\frac{1}{4}$) is determined by pertubation theory [51].

The non-local Fock exchange energy operator E_x recently implemented within the PAW formalism [56] can be expressed in real space as

$$E_x = \frac{e^2}{2} \sum_{\mathbf{k}n,\mathbf{q}m} 2w_{\mathbf{k}} f_{\mathbf{k}n} \times 2w_{\mathbf{q}} f_{\mathbf{q}n} \times \int\int d^3r d^3r' \frac{\phi^*_{\mathbf{k}n}(\mathbf{r})\phi_{\mathbf{k}n}(\mathbf{r})\phi^*_{\mathbf{q}m}(\mathbf{r}')\phi_{\mathbf{q}n}(\mathbf{r}')}{\mid \mathbf{r} - \mathbf{r}' \mid}. \quad (2.58)$$

Here, $\{\phi_{\mathbf{k}n}(\mathbf{r})\}$ is the set of one-electron Bloch states of the system and $\{f_{\mathbf{k}n}\}$ is the corresponding set of (possibly fractional) occupational numbers. The sums over $\mathbf{k}$ and $\mathbf{q}$ run over all chosen $\mathbf{k}$-points for Brillouin zone sampling, whereas the sums over m and n run over all bands at these k-points. The k-point weights $w_{\mathbf{k}}$ sum to unity and the factor 2 accounts for the doubly occupied one-electron states in a closed-shell system [57].

The corresponding nonlocal Fock exchange potential is written as

$$\begin{aligned} V_x(\mathbf{r},\mathbf{r}') &= -e^2 \sum_{\mathbf{q}m} 2w_{\mathbf{q}} f_{\mathbf{q}m} \frac{\phi^*_{\mathbf{q}m}(\mathbf{r}')\phi_{\mathbf{q}n}(\mathbf{r}')}{|\mathbf{r} - \mathbf{r}'|}, \\ &= -e^2 \sum_{\mathbf{q}m} 2w_{\mathbf{q}} f_{\mathbf{q}m} e^{-i\mathbf{q}.\mathbf{r}'} \frac{u^*_{\mathbf{q}m}(\mathbf{r}')u_{\mathbf{q}n}(\mathbf{r}')}{\mid \mathbf{r} - \mathbf{r}' \mid} e^{i\mathbf{q}.\mathbf{r}} \end{aligned} \quad (2.59)$$

where $u_{\mathbf{q}m}(\mathbf{r})$ is the cell periodic part of the Bloch state, $\phi_{\mathbf{k}n}(\mathbf{r})$, at $\mathbf{k}$-points $\mathbf{q}$, with band index m. Using the decomposition of Bloch states, $\phi_{\mathbf{q}m}$, in plane waves, Eq. (2.59) can be rewritten as

$$V_x(\mathbf{r},\mathbf{r}') = \sum_{\mathbf{k}} \sum_{\mathbf{G}\mathbf{G}'} e^{i(\mathbf{k}+\mathbf{G}).\mathbf{r}} V_{\mathbf{k}}(\mathbf{G},\mathbf{G}') e^{-i(\mathbf{k}+\mathbf{G}').\mathbf{r}'}, \quad (2.60)$$

where $V_{\mathbf{k}}(\mathbf{G},\mathbf{G}')$ is the Fock exchange potential in reciprocal space [58], given by the expression

$$
\begin{aligned}
V_{\mathbf{k}}(\mathbf{G},\mathbf{G}') &= \langle \mathbf{k}+\mathbf{G} \left| \hat{V}_x \right| \mathbf{k}+\mathbf{G}' \rangle \\
&= -\frac{4\pi e^2}{\Omega} \sum_{m\mathbf{q}} 2 w_{\mathbf{q}} f_{\mathbf{q}m} \times \sum_{\mathbf{G}\mathbf{G}''} \frac{C^*_{\mathbf{q}m}(\mathbf{G}'-\mathbf{G}'') C_{\mathbf{q}m}(\mathbf{G}-\mathbf{G}'')}{\mid \mathbf{k}-\mathbf{q}+\mathbf{G}'' \mid^2}. \quad (2.61)
\end{aligned}
$$

This allows faster convergence of the exact exchange energy with respect to the **k**-points for periodic systems or with respect to the supercell size for isolated systems.

Previous studies [53, 59] have shown that the PBE0 functional offers significant improvement with respect to standard PBE calculations for finite systems. This is ascribed to the fact that the use of certain portion of exact exchange reduces the self-interaction error [60] of DFT. For infinite systems, i.e. under periodic boundary conditions, the calculation of exact exchange energy in real space is still very expensive largely due to the slow decay of the exchange interaction with distance.

The HSE functional

To avoid the computational expense of the exact exchange, Heyd and co-workers [54] proposed to eliminate the long-range part of the HF exchange by applying a screened Coulomb potential only to the exchange interaction so as to reduce the domain over which the real space integrals have to be evaluated. Accordingly, an error function is used to split the Coulomb operator into short-range and long-range components:

$$
\frac{1}{r} = S_\mu(r) + L_\mu(r) = \frac{1-\mathrm{erf}(\mu r)}{r} + \frac{\mathrm{erf}(\mu r)}{r}, \quad (2.62)
$$

where $r = |\mathbf{r}-\mathbf{r}'|$, $1-\mathrm{erf}(\mu r)$ is the complementary error function, and μ is the range-separation parameter that defines a characteristic distance $(2/\mu)$ beyond which the short-range interactions become negligible. The screened exchange-correlation

energy hybrid functional proposed by Heyd and co-workers is given by

$$E_{xc}^{HSE} = \frac{1}{4}E_x^{sr,\mu} + \frac{3}{4}E_x^{PBE,sr,\mu} + E_x^{PBE,lr,\mu} + E_c^{PBE}. \tag{2.63}$$

The electronic correlation is completely described by the correlation part of the standard PBE density functional as in the PBE0 functional, while the exchange component of the electron-electron interaction is split into a short-range (sr) and long-range (lr) parts.

The decomposed Coulomb operator (Eq. (2.62)) is used together with Eq. (2.58) to obtain the short-range Fock exchange energy in real space,

$$\begin{aligned} E_x^{sr,\mu} &= \frac{e^2}{2}\sum_{\mathbf{k}n,\mathbf{q}m} 2w_{\mathbf{k}}f_{\mathbf{k}n} \times 2w_{\mathbf{q}}f_{\mathbf{q}n} \times \int\int d^3r d^3r\prime \frac{1-\mathrm{erf}(\mu\,|\mathbf{r}-\mathbf{r}'|)}{|\mathbf{r}-\mathbf{r}'|} \\ &\quad \times\phi^*_{\mathbf{k}n}(\mathbf{r})\phi_{\mathbf{k}n}(\mathbf{r})\phi^*_{\mathbf{q}m}(\mathbf{r}')\phi_{\mathbf{q}n}(\mathbf{r}'), \end{aligned} \tag{2.64}$$

and the short-range Fock exchange potential in reciprocal space is represented by

$$\begin{aligned} V_{\mathbf{k}}^{sr,\mu}(\mathbf{G},\mathbf{G}') &= \langle \mathbf{k}+\mathbf{G} \left| \hat{V}_x^{sr,\mu} \right| \mathbf{k}+\mathbf{G}' \rangle \\ &= -\frac{4\pi e^2}{\Omega}\sum_{m\mathbf{q}} 2w_{\mathbf{q}}f_{\mathbf{q}m} \times \sum_{\mathbf{G}\mathbf{G}''} \frac{C^*_{\mathbf{q}m}(\mathbf{G}'-\mathbf{G}'')C_{\mathbf{q}m}(\mathbf{G}-\mathbf{G}'')}{\mid \mathbf{k}-\mathbf{q}+\mathbf{G}''^2 \mid} \\ &\quad \times(1-e^{-|\mathbf{k}-\mathbf{q}+\mathbf{G}''|^2/4\mu^2}). \end{aligned} \tag{2.65}$$

When comparing Eq. (2.61) and Eq. (2.65), it is clear that the complete Fock exchange potential differs with the short-range Fock potential by a factor $1-e^{-|\mathbf{k}-\mathbf{q}+\mathbf{G}''|^2/4\mu^2}$ in the latter, representing the complementary error function in reciprocal space [57].

In order to optimize computational ease and accuracy, it has been shown that

the optimum range-separation parameter μ is approximately 0.3 and 0.2 Å^{-1} in the context of HSE03 [54] and HSE06 [55, 61] respectively. For $\mu = 0$, it can be seen from Eq. (2.62) that the long-range term becomes zero and the short-range term then equals the full Coulomb operator. The opposite is the case for $\mu \to \infty$. Thus, the HSE functional (Eq. (2.63)) reduces to a PBE0 functional and a standard PBE functional in the limits $\mu = 0$ and $\mu \to \infty$ respectively.

The HSE functional has been proven to yield better results (compared to PBE GGA) in agreement with experiment for a variety of solids including metals, semiconductors and insulators [47, 57, 62–66]. These include the electronic structure, vibrational, and thermodynamic properties for the materials. In this work, we employ the HSE06 hybrid functional to calculate the energy band-gaps for the low pressure phases of ZnO and investigate the extent to which it improves upon the standard DFT functionals within the framework of the plane wave PAW formalism. The results will be compared with those obtained by a more relevant GW approach (discussed in chapter 5).

Chapter 3

Pseudopotentials and the PAW Method

Apart from considering electron-electron interaction, an attempt to solve the Kohn-Sham equations for a crystalline material requires a good description of electron-ion interactions and choice of a basis set to express the single-particle wavefunctions. In this chapter we describe the basic ideas behind the methods of solving the Kohn-Sham equations (Eq. (2.27)), using plane wave basis sets and approximating the ion cores with pseudopotentials. Moreover, an extension of the pseudopotential approximation, known as the projector augmented wave method is discussed in detail as it is employed in this thesis.

3.1 Bloch Theorem and Plane Wave Basis Sets

Plane-wave pseudopotential methods start by representing a real system by a 3-dimensional periodic supercell, that allows the use of Bloch's theorem to simplify the task of solving the Kohn-Sham equation. Bloch's theorem reduces the infinite number

of one-electron wavefunctions in the real system to only the number of electrons in a chosen supercell. According to this theorem, the Bloch state consists of a cell periodic part and a plane-wave part:

$$\psi_{\mathbf{k}}(\mathbf{r}) = \exp[i\mathbf{k}\cdot\mathbf{r}] f_{\mathbf{k}}(\mathbf{r}). \tag{3.1}$$

The first term is the plane-wave part and the second term is the cell periodic part. The whole expression itself is already wavelike, being the eigenstate of a one-particle Schrödinger equation. The cell periodic part $f_{\mathbf{k}}(\mathbf{r})$, is invariant under translation by a lattice vector $\mathbf{R}$

$$f_{\mathbf{k}}(\mathbf{r}) = f_{\mathbf{k}}(\mathbf{r}+\mathbf{R}),$$

and it can be expanded in terms of a discrete plane-wave basis set whose wave vectors are the reciprocal lattice vectors of the crystal,

$$f_{\mathbf{k}}(\mathbf{r}) = \sum_{\mathbf{G}} c_{\mathbf{k},\mathbf{G}} \exp[i\mathbf{G}\cdot\mathbf{r}], \tag{3.2}$$

where $\mathbf{G}$ are the reciprocal lattice vectors [1]. Therefore each electronic wavefunction can be written as a sum of plane-waves,

$$\psi_{\mathbf{k}}(\mathbf{r}) = \sum_{\mathbf{G}} c_{\mathbf{k},\mathbf{G}} \exp[i(\mathbf{k}+\mathbf{G})\cdot\mathbf{r}]. \tag{3.3}$$

Thus, the problem of solving the Kohn-Sham equations has now been mapped onto one of calculating a finite number of electronic wavefunctions in the unit cell, at an - in principle - infinite number of $\mathbf{k}$ points within the first Brillouin zone of a periodic cell. Obviously, it is not desirable to solve the electronic problem for an

infinite number of Bloch states. Nearby $\mathbf{k}$ vectors carry very similar information. Therefore, it should be possible to reproduce the required physical properties to the desired numerical accuracy by using the wavefunctions at a finite number of $\mathbf{k}$ points in the first Brillouin zone [67].

3.1.1 The k vector and the Brillouin zone

The $\mathbf{k}$ vector plays a fundamental role in the electronic structure of a solid. It is the propagation vector (in reciprocal space) associated with the plane-wave part of the wavefunction. From Bloch theorem, it follows that there is a particular class of vectors $\mathbf{k}$ such that the phase factor $\exp[i\mathbf{k}\cdot\mathbf{r}] = 1$, and thus the wavefunction is in phase in all periodic replicas of the unit cell. The set of the three smallest independent such vectors is sufficient to determine all the reciprocal lattice vectors, in the same way as with the primitive vectors in real space [67].

The *first Brillouin zone* or simply the Brillouin zone (BZ), for short, is the cell in reciprocal space, of volume $\Omega_R = \mathbf{b}_1\cdot(\mathbf{b}_2 \times \mathbf{b}_3) = (\mathbf{2\pi})^3/\Omega$ defined by the primitive reciprocal lattice vectors. The BZ is purely constructed from the reciprocal lattice and thus only follows from the translational symmetry of the 14 Bravais lattices. In two and three dimensions, symmetry can be exploited to reduce the portion of the BZ that has to be sampled in the determination of the electron density. This requires the concept of the *irreducible wedge* of the BZ (IBZ), which is the minimal portion that contains all the necessary information to describe the whole BZ. Details about symmetry and the construction of the IBZ can be found in references [67] and [68].

Methods such as Monkhorst-Pack [69] are used to obtain an accurate approximation for the electronic potential and the total energy of an insulator or a semiconductor by calculating the electronic states at a very small number of special $\mathbf{k}$-points. For

metallic systems, a dense set of **k** points is required to define the Fermi surface precisely and to reduce the magnitude of the error in the total energy, which may arise due to the inadequacy of the **k**-point sampling. The computed total energy converges as the **k** points increase so that the error due to the finite **k**-point sampling can be made as small as needed. In principle, a converged electronic potential and total energy can always be obtained provided that the computational time is available to calculate the wave functions at a sufficiently dense set of **k** points [1].

3.1.2 Plane wave cutoff

The Fourier series in Eq. (3.3) is in principle, infinite. However the coefficients $c_{\mathbf{k},\mathbf{k}+\mathbf{G}}$ are associated with plane waves of kinetic energy $(\hbar^2/2m)\,|\mathbf{k}+\mathbf{G}|^2$. The plane waves with a smaller kinetic energy are typically more important than those with large kinetic energy. Introduction of an energy cutoff of the discrete plane-wave basis set produces a finite basis set. This energy cutoff will lead to an error in the total energy of the system, but it is possible to reduce the error magnitude by increasing the size of the basis set by allowing a larger energy cutoff. In principle, the cutoff energy should be increased until the calculated total energy converges within the required tolerance [1].

The advantage of using plane-wave basis sets for the electronic wave functions is that the Kohn-Sham equations take a particularly simple form. Substitution of Eq. (3.3) into the Kohn-Sham equation (Eq. (2.27)), and integrating over **r** gives

$$\sum_{\mathbf{G}'}[\frac{\hbar^2}{2m}\left|\mathbf{k}+\mathbf{G}\right|^2\delta_{\mathbf{G}\mathbf{G}'}+v_{ion}(\mathbf{G}-\mathbf{G}')$$
$$+v_H(\mathbf{G}-\mathbf{G}')+v_{xc}(\mathbf{G}-\mathbf{G}')]c_{k,\mathbf{k}+\mathbf{G}'}$$
$$= \varepsilon_{\mathbf{k}}c_{\mathbf{k},\mathbf{k}+\mathbf{G}'}. \tag{3.4}$$

Thus, the reciprocal space representation of the kinetic energy is diagonal, and the various potential contributions are described in terms of their Fourier components. The usual method of solving Eq. (3.4) is by diagonalization of the Hamiltonian matrix whose elements $H_{\mathbf{k}+\mathbf{G},\mathbf{k}+\mathbf{G}'}$ are given by the terms in the brackets above.

The size of the matrix is determined by the cutoff energy $(\hbar^2/2m)\left|\mathbf{k}+\mathbf{G}_c\right|^2$ and will be intractably large for systems that contain both valence and core electrons. This is because a very large number of plane waves are required to accurately describe the rapidly oscillating wavefunctions of electrons in the core region. To overcome this problem, plane-wave basis sets are practically always used in conjunction with the pseudopotential approximation, as discussed in the next section.

3.2 Pseudopotential Approximation

It is well known that most physical properties of solids depend more on the valence electrons than on the core electrons [1]. The pseudopotential approximation takes advantage of this by replacing the real potential arising from the nuclear charge and the core electrons by a weaker pseudopotential, within a core region of radius $\mathbf{r}_c$ as illustrated schematically in Figure 3.1.

This pseudopotential acts on a set of pseudo wavefunctions rather than the true valence wavefunctions. The valence wavefunctions oscillate rapidly in the region oc-

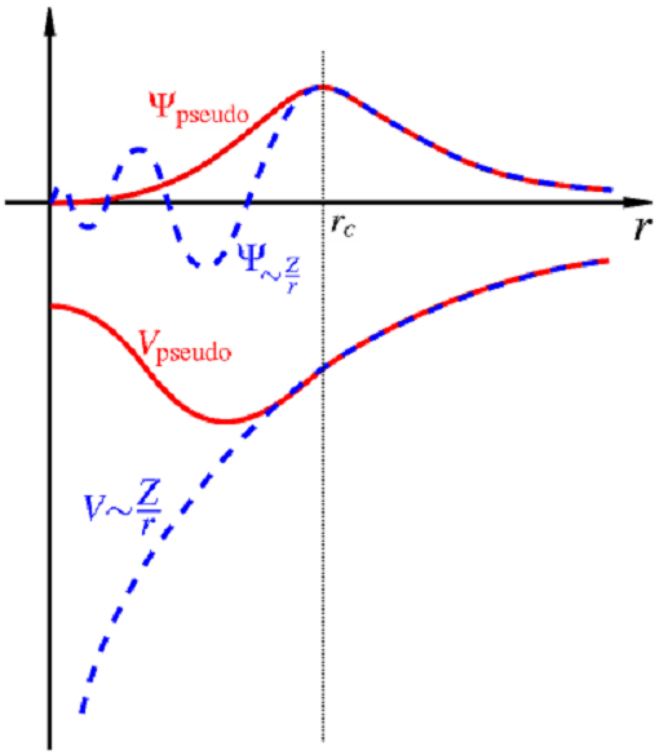

Figure 3.1: Schematic illustration of an all-electron (dashed lines) and pseudoelectron (solid lines) valence wavefunctions and potentials. The radius at which all-electron and pseudoelectron values match is designated $\mathbf{r}_c$. From Ref. [1].

cupied by the core electrons due to the strong ionic potential in this region. These oscillations are necessary to maintain the orthogonality between the valence wavefunctions and the core wavefunctions.

Most pseudopotentials used in electronic structure calculations are generated from all-electron density-functional calculations for spherical atoms. Several methods of pseudopotential generation exist. For norm conserving pseudopotentials, the pseudopotential must obey several criteria. These are:

(i) The total core charge produced by the pseudo wavefunctions must be the same as that produced by the atomic wavefunctions to ensure that the pseudo atom produces the same scattering properties as the ionic core.

(*ii*) Pseudo-electron eigenvalues must be the same as the valence eigenvalues obtained from the atomic wavefunctions.

(*iii*) Pseudo wavefunction as well as its first and second derivative must be continuous at the core radius and must also be non-oscillatory.

To obtain the exchange-correlation energy accurately it is necessary that outside the core region the real and pseudo wavefunctions be identical so that both wavefunctions generate identical charge densities. Generation of a pseudopotential that satisfies

$$\int_0^{R_c} \Psi_{AE}^{*}(\mathbf{r})\,\Psi_{AE}(\mathbf{r})\,d\mathbf{r} = \int_0^{R_c} \Psi_{ps}^{*}(\mathbf{r})\,\Psi_{ps}(\mathbf{r})\,d\mathbf{r} \tag{3.5}$$

where $\Psi_{AE}(\mathbf{r})$ is the all electron wavefunction and $\Psi_{ps}(\mathbf{r})$ is the pseudo wavefunction, guarantees the equality of the all electron and pseudo wavefunctions outside the core region. Moreover, as pointed out by Hamann *et al.* [70], this assures that the first order energy dependence of the scattering from the ion core is correct, so that the scattering is accurately described over a wide range of energy. In practice this is achieved using a *non-local* pseudopotential which uses a different potential for each angular momentum component of the pseudopotential. Pseudopotentials of this type are known as *ab initio* or *norm-conserving* pseudopotentials and are the most *transferable* since they are capable of describing the scattering properties of an ion in a variety of atomic environments.

Non-local pseudopotential can be expressed [70] as

$$v^{ps}(\mathbf{r},\mathbf{r}') = \bar{v}(\mathbf{r})\,\delta(\mathbf{r}-\mathbf{r}') + \sum_L \left[\; Y_L(\mathbf{r})\left[v_l^{ps}(\mathbf{r}) - \bar{v}(\mathbf{r})\right]\frac{\delta(|\mathbf{r}|-|\mathbf{r}'|)}{|\mathbf{r}|^2}Y_L^{*}(\mathbf{r}')\;\right], \tag{3.6}$$

were Y_L are spherical harmonics and L denotes a combined angular momentum quantum number (l, m), $\bar{v}(\mathbf{r})$ is a local potential that is typically chosen to cancel the most expensive (in computational demand) non-local terms, i.e. those that correspond to the highest physically relevant angular momentum $l > l_{\max}$. The pseudopotential given in Eq. 3.6 is non-local as it depends on two position arguments, $\mathbf{r}$ and $\mathbf{r}'$ and it is computationally expensive. In practice, substantial savings in computer time and storage can be achieved by using a separable form of the pseudopotential [71]:

$$v^{ps} \approx \sum_{i,j} \mid v^{ps}\tilde{\phi}_i\rangle \left[\left\langle \tilde{\phi}_j \mid v^{ps} \mid \tilde{\phi}_i \right\rangle\right]^{-1}_{i,j} \langle\tilde{\phi}_j \mid v^{ps}. \tag{3.7}$$

where i and j are composite indices containing the atomic-site index R, the angular momentum quantum numbers l, m and an additional index α. The index α distinguishes partial waves with otherwise identical indices R,l,m, as more than one partial wave per site and angular momentum is allowed.

Thus Eq. (3.7) replaces the projection onto spherical harmonics Y_L used in the non-local form of Eq. (3.6) by a projection onto angular momentum dependent functions $\mid v^{ps}\tilde{\phi}_i\rangle$. The validity of this equation can be easily shown by applying an arbitrary wavefunction $\mid \tilde{\Psi}\rangle = \sum_i \mid \tilde{\phi}_i\rangle c_i$ to both sides and its form is exact if one chooses a complete set of pseudo partial waves $\mid \tilde{\phi}_i\rangle$. The advantage of the separable form is that $\langle\tilde{\phi}v^{ps} \mid$ is treated as one function, so that expectation values are reduced to combinations of simple scalar products $\langle\tilde{\phi}_i v^{ps} \mid \tilde{\Psi}\rangle$.

3.3 Ultrasoft Pseudopotentials

Early developments of accurate norm-conserving pseudopotentials quickly showed that the potentials for first row elements such as Lithium turn out to be extremely

hard [72]. A pseudopotential is considered *hard* when many plane waves are needed to represent the pseudo-wavefunctions, and *soft* when it requires a small number of plane waves for accurate representation of pseudo-wavefunctions.

Various schemes have been suggested to improve convergence properties of norm-conserving pseudopotentials [73]. Despite the best attempts [74, 75] to optimize their performance for the first row elements, it has not been possible to develop soft norm-conserving pseudopotentials. Vanderbilt [76] proposed a radical departure from the concept of norm-conservation. This involves relaxing the norm-conservation constraint in order to generate *ultrasoft pseudopotentials* (USP).

In Vanderbilt's USP approach the total energy is written as

$$\begin{aligned} E &= \sum_{occ} \langle \psi_j \mid T + v^{NL} \mid \psi_j \rangle + \int d^3 r v^L(\mathbf{r})\, n(\mathbf{r}) + \\ &\quad \frac{1}{2} \int d^3 r d^3 r' \frac{n(\mathbf{r})\, n(\mathbf{r}')}{\mid \mathbf{r} - \mathbf{r}' \mid} + E_{xc}[n] + E_{ii}, \end{aligned} \tag{3.8}$$

where $n(\mathbf{r})$ is the electron density, T is the kinetic energy operator, $E_{xc}[n]$ is the exchange and correlation energy, E_{ii} is the ion-ion interaction energy, and the ψ_j are the pseudo-wavefunctions. The pseudopotential contains a local part $v^L(\mathbf{r})$ and a fully non-local separable part given by

$$v^{NL} = \sum_{mn} D^{(0)}_{nm} \mid \beta_n \rangle \langle \beta_m \mid , \tag{3.9}$$

where the functions β_m as well as the coefficients $D^{(0)}_{nm}$ characterize the pseudopotential and differ for different atomic species. For simplicity, one atomic species is considered. The β_m are represented in an angular expansion, *i.e.* spherical harmonics multiplied by radial functions which vanishes outside the core region. The indices n

and m in Eq. (3.9) run over the total number N_β of such functions [77].

The electron density $n(\mathbf{r})$ in Eq. (3.8) is given by the square of the pseudo-wavefunctions plus an augmentation inside the spheres.

$$n(\mathbf{r}) = \sum_{occ} \left[\mid \psi_j(\mathbf{r}) \mid^2 + \sum_{mn} Q_{nm}(\mathbf{r}) \langle \psi_j \mid \beta_n \rangle \langle \beta_m \mid \psi_j \rangle \right], \tag{3.10}$$

where the $Q_{nm}(\mathbf{r})$ are augmentation functions determined during pseudopotential generation and are strictly localized in the core regions. Thus, the electron density in Eq. (3.10) is separated into a *soft* delocalized contribution given by the squared moduli of the wavefunctions, and a new *hard* contribution localized at the cores while it is still quadratic in the wavefunctions

The norm-conserving condition is relaxed by introducing a generalized orthonormality condition

$$\langle \psi_j \mid S \mid \psi_j \rangle = \delta_{ij}, \tag{3.11}$$

where S is a Hermitian overlap operator given by

$$S = 1 + \sum_{nm} q_{nm} \mid \beta_n \rangle \langle \beta_m \mid , \tag{3.12}$$

with $q_{nm} = \int d^3r Q_{nm}(\mathbf{r})$. This orthonormality condition (3.11) is consistent with the conservation of the charge $\int d^3r \; n(\mathbf{r}) = N$.

Applying the variational principle to Eqs. (3.8) to (3.10) under condition (3.11), yields

$$H \mid \psi_j \rangle = \varepsilon_j S \mid \psi_j \rangle \tag{3.13}$$

where

$$H = T + v_{xc}(\mathbf{r}) + v_H(\mathbf{r}) + v^L(\mathbf{r}) + \sum_{mn} D_{nm} \mid \beta_n \rangle \langle \beta_m \mid . \tag{3.14}$$

The new coefficients D_{nm} are the $D_{nm}^{(0)}$ with a screening term

$$D_{nm} = D_{nm}^{(0)} + \int d^3 r v_{eff}(\mathbf{r}) Q_{nm}(\mathbf{r}), \tag{3.15}$$

where $v_{eff}(\mathbf{r})$ denotes the effective local potential, given by the local pseudopotential $v^L(\mathbf{r})$ plus the exchange correlation $v_{xc}(\mathbf{r})$ and Hartree $v_H(\mathbf{r})$ potentials [78].

Besides being much softer than their norm-conserving counterparts, the USP have another advantage. The generation algorithm for the USP guarantees good scattering properties and their energy derivatives at several energies spanning the range of occupied states, and the transferability can be systematically improved by increasing the number of such energies.

3.4 The PAW Method

The PAW method is a generalization of ideas from both Vanderbilt-type ultrasoft-pseudopotential (USPP) [76] and the linear-augmented-plane-wave (LAPW) [79] methods. This method was first proposed by Blöchl, and the formal relationship between the USPP and the PAW method has been derived by Kresse and Joubert [80]. One of its main goals was to introduce energy and potential independent basis sets that were as accurate as the previously used augmented basis sets in LAPW method. Moreover, this method was required to match the efficiency of the pseudopotential approach for molecular dynamics simulations and to be an exact theory with easily controlled convergence. The most important feature of this method is its retention of core electron

behavior in a computationally efficient manner.

At the root of the PAW method lies a linear transformation [81]

$$T = 1 + \sum_i \left(\mid \phi_i \rangle - \mid \tilde{\phi}_i \rangle \right) \langle \tilde{p}_i \mid , \tag{3.16}$$

with the following quantities as basic ingredients:

(i) ϕ_i are the all-electron (AE) partial waves obtained by radially integrating the Schrödinger equation

$$\left(-\frac{1}{2}\nabla^2 + v_{at} - \epsilon_i^1 \right) \mid \phi_i \rangle = 0 \tag{3.17}$$

for the atomic AE potential v_{at} and a set of energies ϵ_i^1. These are chosen to describe the physically relevant states, i.e., those from the valence region, reasonably well.

(ii) $\tilde{\phi}_i$ are the pseudo (PS) partial waves obtained as solutions of the Schrödinger equation

$$\left(-\frac{1}{2}\nabla^2 + w_i(r) - \epsilon_i^1 \right) \mid \tilde{\phi}_i \rangle = 0 \tag{3.18}$$

for the energy of the corresponding AE partial waves and the PS potential $w_i(r)$. This PS potential $w_i(r)$ is defined for each AE partial wave, as

$$w_i(r) = \tilde{v}_{at}(r) + c_i k(r), \tag{3.19}$$

were $\tilde{v}_{at}(r)$ is the atomic PS potential and $k(r) = \exp[-(r/r_k)^\lambda]$ is the cutoff function. The free coefficient c_i is determined such that the PS partial wave $\tilde{\phi}_i$ coincides with the corresponding AE partial wave ϕ_i outside the augmentation region.

(*iii*) $\tilde{p}_i$ is the projector function for each PS partial wave $\tilde{\phi}_i$; calculated as

$$\mid \tilde{p}_i\rangle = \left(-\frac{1}{2}\nabla^2 + \tilde{v}_{at} - \epsilon_i^1\right) \mid \tilde{\phi}_i\rangle. \tag{3.20}$$

These projector functions must be modified in such a way that they satisfy the condition $\langle \tilde{p}_i \mid \tilde{\phi}_j\rangle = \delta_{ij}$, which is then imposed iteratively beginning with the lowest partial wave.

This transformation (Eq. 3.16) maps the AE wavefunctions Ψ_n with their complete nodal structure onto nodeless pseudo (PS) wavefunctions $\tilde{\Psi}_n$. That is

$$\begin{aligned} \mid \Psi_n\rangle =& \mid \tilde{\Psi}_n\rangle + \sum_i \left(\mid \phi_i\rangle - \mid \tilde{\phi}_i\rangle\right) \langle \tilde{p}_i \mid \tilde{\Psi}_n\rangle \\ =& \mid \tilde{\Psi}_n\rangle + \sum_R \left(\mid \Psi_R^1\rangle - \mid \tilde{\Psi}_R^1\rangle\right), \end{aligned} \tag{3.21}$$

where

$$\mid \Psi_R^1\rangle = \sum_{i\epsilon R} \mid \phi_i\rangle\langle \tilde{p}_i \mid \tilde{\Psi}_n\rangle \tag{3.22}$$

and

$$\mid \tilde{\Psi}_R^1\rangle = \sum_{i\epsilon R} \mid \tilde{\phi}_i\rangle\langle \tilde{p}_i \mid \tilde{\Psi}_n\rangle. \tag{3.23}$$

The PS wavefunctions $\tilde{\Psi}_n$ are the variational parameters, instead of the AE wavefunctions. In the PAW context, an AE wavefunction is a full one-electron Kohn-Sham wavefunction, and is not to be confused with a many-electron wavefunction. The index i refers to partial waves that belong to the atomic site **R,** the angular momentum quantum numbers $L = (l, m)$, and an additional index k refers to the reference energy

$\epsilon_{k,l}$. With such a transformation, the nodeless PS wavefunctions can be expanded in convenient plane-wave basis sets, and all physical properties can be evaluated after reconstructing the related AE wavefunctions.

3.4.1 Expectation values

Since the PS wavefunctions play the role of the variational parameters in the PAW method, physical quantities must be expressed as the expectation values of the PS wavefunctions. Accordingly, the expectation value of some operator A can be obtained as

$$\langle A \rangle = \sum_n f_n \langle \tilde{\Psi}_n \mid \tilde{A} \mid \tilde{\Psi}_n \rangle, \tag{3.24}$$

where n is the band index and f_n is the occupation of the valence state. Using Eq. (3.16), the PS operator can be written in the form

$$\tilde{A} = A + \sum_{i,j} \mid \tilde{p}_i \rangle \left(\langle \phi_i \mid A \mid \phi_j \rangle - \langle \tilde{\phi}_i \mid A \mid \tilde{\phi}_j \rangle \right) \langle \tilde{p}_j \mid . \tag{3.25}$$

The first part is an operator that directly acts on the PS wavefunction and is evaluated either in real or reciprocal space. The remaining two parts contain the projectors and the expectation value of the operator either between the AE or the PS partial waves [81].

Furthermore, there is an additional freedom to add an arbitrary operator of the form

$$B - \sum_{i,j} \mid \tilde{p}_i \rangle \langle \tilde{\phi}_i \mid B \mid \tilde{\phi}_j \rangle \langle \tilde{p}_j \mid \tag{3.26}$$

to the right side of Eq. (3.25), with no change in the expectation values. For example,

the problem of the singularity of the nuclear electrostatic potential can be alleviated by adding a term of the form (3.26) to the PS electrostatic potential obtained from Eq. (3.25).

The expressions for physical quantities in the PAW method follow from Eqs. (3.16) and (3.25). For example, the charge density is given by [80, 81]

$$n\left(\mathbf{r}\right)=\tilde{n}\left(\mathbf{r}\right)+n^{1}\left(\mathbf{r}\right)-\tilde{n}^{1}\left(\mathbf{r}\right), \tag{3.27}$$

where $\tilde{n}$ is the soft PS charge density calculated directly from the PS wavefunctions on a plane-wave grid:

$$\tilde{n}\left(\mathbf{r}\right)=\sum_{n}f_{n}\langle\tilde{\Psi}_{n}\mid\mathbf{r}\rangle\langle\mathbf{r}\mid\tilde{\Psi}_{n}\rangle. \tag{3.28}$$

The quantities n^1 and $\tilde{n}^1$ are the onsite charge densities, treated on a radial support grid. They are defined as

$$n^{1}\left(\mathbf{r}\right)=\sum_{(i,j)}\rho_{ij}\langle\phi_{i}\mid\mathbf{r}\rangle\langle\mathbf{r}\mid\phi_{j}\rangle, \tag{3.29}$$

and

$$\tilde{n}^{1}\left(\mathbf{r}\right)=\sum_{(i,j)}\rho_{ij}\langle\tilde{\phi}_{i}\mid\mathbf{r}\rangle\langle\mathbf{r}\mid\tilde{\phi}_{j}\rangle. \tag{3.30}$$

Here ρ_{ij} are the occupancies of each augmentation channel (i,j) calculated from the PS wavefunctions applying the projector functions:

$$\rho_{ij}=\sum_{n}f_{n}\langle\tilde{\Psi}_{n}\mid\tilde{p}_{i}\rangle\langle\tilde{p}_{j}|\tilde{\Psi}_{n}\rangle. \tag{3.31}$$

For a complete set of projectors the charge density $n^1\left(\mathbf{r}\right)$ is exactly the same as $\tilde{n}$

within the augmentation spheres.

3.4.2 The PAW total energy

Like the charge density, the total energy can be divided into three terms,

$$E = \tilde{E} + E^1 - \tilde{E}^1. \tag{3.32}$$

which are given by

$$\begin{aligned} \tilde{E} &= \sum_n f_n \langle \tilde{\Psi}_n \mid -\frac{1}{2}\Delta \mid \tilde{\Psi}_n \rangle + E_{xc}\left[\tilde{n} + \hat{n} + \tilde{n}_c\right] + E_H\left[\tilde{n} + \hat{n}\right] \\ &\quad + \int \upsilon_H\left[\tilde{n}_{Zc}\right]\left[\tilde{n}\left(\mathbf{r}\right) + \hat{n}\left(\mathbf{r}\right)\right] d\mathbf{r} + U(\mathbf{R}, Z_{ion}), \end{aligned} \tag{3.33}$$

$$\begin{aligned} \tilde{E}^1 &= \sum_{(i,j)} \rho_{ij} \langle \tilde{\phi}_i \mid -\frac{1}{2}\Delta \mid \tilde{\boldsymbol{\phi}}_j \rangle + E_{xc}\left[\tilde{n}^1 + \hat{n} + \tilde{n}_c\right] + E_H\left[\tilde{n}^1 + \hat{n}\right] \\ &\quad + \int_{\Omega_r} \upsilon_H\left[\tilde{n}_{Zc}\right]\left[\tilde{n}^1\left(\mathbf{r}\right) + \hat{n}\left(\mathbf{r}\right)\right] d\mathbf{r}, \end{aligned} \tag{3.34}$$

$$\begin{aligned} E^1 &= \sum_{(i,j)} \rho_{ij} \langle \phi_i \mid -\frac{1}{2}\Delta \mid \boldsymbol{\phi}_j \rangle + E_{xc}\left[n^1 + n_c\right] \\ &\quad + E_H[n^1] + \int_{\Omega_r} \upsilon_H\left[n_{Zc}\right] n^1\left(\mathbf{r}\right) d\mathbf{r}. \end{aligned} \tag{3.35}$$

where υ_H is the electrostatic potential of the charge density n, $E_H[n]$ is its electrostatic energy, and $U(\mathbf{R}, Z_{ion})$ is the electrostatic energy of point charges Z_{ion} in a uniform

electrostatic background [80].

The expression $\tilde{E}$ denotes the energy due to the smooth functions evaluated in Fourier space or real space grid, $\tilde{E}^1$ denotes the energy evaluated only in the spheres on radial grids, and E^1 the energy in the spheres with the full functions.

3.4.3 Advantages of PAW method

The PAW method has several advantages over other approaches mainly because of its all-electron nature. Vanderbilt's USP approach has been widely used, however it requires the determination of a number of parameters. The choice of these parameters is critical as they influence the results, and therefore this requires extensive tests in order to obtain an accurate and highly transferable pseudopotential. In Blöchl's PAW method, the construction of datasets is easier because the pseudization of the augmentation charges is avoided, i.e., the PAW method works directly with the full AE wavefunctions and AE potentials. In addition, the PAW method has the advantage that the total energy expression is less complex and can therefore be expected to be more efficient.

In the pseudopotential approach, a pseudopotential constructed from an isolated atom is not guaranteed to be accurate for a molecule. In contrast, the converged results of the PAW method do not depend on a reference system such as an isolated atom, because the PAW uses the full density and potential. Also, the plane-wave convergence is more rapid than in norm-conserving pseudopotentials and should in principle be equivalent to that of ultrasoft pseudopotentials [82].

Chapter 4

Outline of Calculations

This chapter deals with the various mathematical and physical aspects involved in the calculation of ground state properties of materials within density functional theory and basis sets described in chapter 3. We discuss in particular, the basic procedure followed before attempting any structural prediction, the ground state properties and the equation of state used to determine the phase diagram of the ZnO system under study.

Calculations described here were performed using a density functional code, Vienna Ab Initio Simulation Package (VASP) [83, 84]. The electron-ion interaction was described by the projector-augmented wave (PAW) method [80, 81] with plane wave basis functions. The exchange-correlation energy functional was approximated by both the local-density and generalized-gradient approximations.

4.1 Convergence Tests

Since we compare energies of different structures having different unit cell volumes and Brillouin shapes, convergence with respect to energy cutoff and the number of

k-points is necessary. For all the calculations reported in this work, the basis set contains plane waves up to an energy cutoff of 400 eV.

An appropriate choice of the **k**-points set is important for achieving balance between accuracy and efficiency. There are an infinite number of **k**-points in the first Brillouin zone for which the Kohn-Sham Hamiltonian must be solved, depending on the nature of the system under study. Semiconducting and insulating systems require an order of magnitude less **k**-points than metallic systems. In addition, for metallic systems, the number of **k**-points also depends on the smearing method in use. In this study we use the tetrahedron method with Blöchl corrections. This method converges rapidly with the number of **k**-points and requires only minimal interference of the user, and is known to yield accurate total energies and a good account for the electronic density of states in bulk materials [83].

For cubic structures, special **k**-points were generated using the equally spaced standard Monkhorst-Pack grids [69]. Monkhorst-Pack grids are now the most widely used because they lead to a uniform set of points determined by a simple formula valid for any crystal

$$\mathbf{k}_{n_1,n_2,n_3} \equiv \sum_{i}^{3} \frac{2n_i - N - 1}{2N} \mathbf{G}_i, \tag{4.1}$$

where the $\mathbf{G}_i$ are the primitive vectors of the reciprocal lattice, $n_i = 1, 2, ..., N$. The set of points defined by Eq. (4.1) is a uniform grid in **k** that is a scaled version of the reciprocal lattice which does not include the gamma (Γ) point. However this method is known to have problems for many non-cubic lattices, and thus Γ centered grids were used to generate special points for hexagonal structures.

The Brillouin zone sampling was carried out using different number of k-points within the irreducible part of the zone, at a fixed energy cutoff for each of the struc-

tures. The total energy was considered converged when the energy difference is within 1 meV per atom, since further increase of the k-point density had no significant effect on the desired properties.

4.2 Bulk Modulus

The bulk modulus for a solid under compression, at volume V and temperature T is defined as

$$\begin{aligned} B &= -V\left(\frac{\partial P}{\partial V}\right)_T \\ &= V\left(\frac{\partial^2 E}{\partial V^2}\right)_T - TV\left(\frac{\partial\left(\alpha B\right)}{\partial V}\right)_T + \frac{V}{2}\sum_i \hbar\left(\frac{\partial^2 \nu_i}{\partial V^2}\right)_T, \end{aligned} \tag{4.2}$$

where $P = -\left(\frac{\partial E}{\partial V}\right)_T$ is the applied pressure, E is the internal energy, α is the thermal expansivity and ν_i is a vibrational frequency. The last two terms in Eq. (4.2) are the finite temperature and zero point corrections, respectively. In most cases, these corrections are small and usually negligible [85].

4.3 Equation of State

Knowledge of the equation of state (EOS) [the pressure, volume, temperature (P-V-T) relation], based on either calculation or measurement, is of primary importance in both basic and applied sciences. It depends on the nature of the interatomic interactions and thus provides insight into the nature of the solid-state. At the same time it determines the values of fundamental thermodynamic parameters [86]. There exists several approximations for describing the form of the isothermal P-V relation.

The form of the total energy versus distance between atoms is qualitatively different for different classes of solids. This has led to a variety of forms for EOS of solids in the literature. The starting point for many equations of state for solids is that the bulk modulus pressure derivative,

$$B' = \left(\frac{\partial B}{\partial P}\right)_T \tag{4.3}$$

is found to change little with pressure. If we take $B' = B'_0$ to be a constant, then

$$B(P) = B_0 + B'_0 P \tag{4.4}$$

where B_0 is the bulk modulus evaluated at zero pressure. This may be equated with Eq. (4.2) and rearranged as

$$\frac{dV}{V} = -\frac{dP}{B_0 + B'_0 P}. \tag{4.5}$$

Upon integration, one obtains the Murnaghan [87] equation of state for pressure

$$P(V) = \frac{B_0}{B'_0}\left(\left(\frac{V_0}{V}\right)^{B'_0} - 1\right), \tag{4.6}$$

or equivalently, for volume

$$V(P) = V_0\left(1 + B'_0\frac{P}{B_0}\right)^{-1/B'_0}. \tag{4.7}$$

Substituting Eq. (4.6) into $E = E_0 - \int P dV$ then results in the Murnaghan equation of state for energy

$$E(V) = E_0 + \frac{B_0 V}{B'_0}\left(\frac{(V_0/V)^{B'_0}}{B'_0 - 1} + 1\right) - \frac{B_0 V_0}{B'_0 - 1}. \tag{4.8}$$

Although it is well known and extensively used, the Murnaghan EOS for solids has increasing accuracy only when $P \longrightarrow 0$ as it is obtained by integrating a linearized bulk modulus-pressure relation (Eq. (4.4)).

In this study, our results are based upon the third-order Birch-Murnaghan isothermal EOS proposed by Francis Birch [88]. It is given by

$$P = \frac{3}{2}B_0\left[\left(\frac{V_0}{V}\right)^{\frac{7}{3}} - \left(\frac{V_0}{V}\right)^{\frac{5}{3}}\right]\left\{1 + \frac{3}{4}\left(B_0' - 4\right)\left[\left(\frac{V_0}{V}\right)^{\frac{2}{3}} - 1\right]\right\}. \tag{4.9}$$

Again, $E\left(V\right)$ is found by integration of the pressure:

$$E\left(V\right) = E_0 + \frac{9V_0B_0}{16}\left\{\left[\left(\frac{V_0}{V}\right)^{\frac{2}{3}} - 1\right]^3 B_0' + \left[\left(\frac{V_0}{V}\right)^{\frac{2}{3}} - 1\right]^2\left[6 - 4\left(\frac{V_0}{V}\right)^{\frac{2}{3}}\right]\right\}. \tag{4.10}$$

This is known to give a realistic estimation of the bulk modulus (B_0) and its pressure derivative (B_0') at equilibrium [89]. The equilibrium bulk properties V_0, B_0, and B_0' as well as the total energy at equilibrium are determined using LDA and GGA functionals by fitting the total energy as a function of unit cell volume data into the third-order Birch-Murnaghan EOS (Eq. (4.10)). These data are obtained from a set of volumes over a range of values around equilibrium. A set of curves representing the equations of state of different phases may be used to predict the transition pressures between the phases.

4.4 Cohesive Energy

The cohesive energy of a solid is the energy required in order to rip it apart into separate constituent atoms. By itself, this energy does not have much significance and

bears no relation to the practical strengths of solids. Practical strength is regulated by resistance to flow and fracture [90]. Experimentally, the cohesive energy is deduced from thermochemical data, as the enthalpy of formation.

In electronic structure calculations, the cohesive energy E_{coh} is computed as the energy difference between the atomic and the bulk ground states. For ZnO, E_{coh} is expressed as

$$E_{coh}(ZnO) = E_{ZnO}^{solid} - (E_{Zn}^{atom} + E_{O}^{atom}). \tag{4.11}$$

The quantities in this expression are evaluated per unit cell. The energy calculations for both the isolated atoms and crystal are performed at the same level of accuracy in order to obtain accurate values for $E_{coh}(ZnO)$. The cohesive energy makes it possible to address the question of how crystals choose their equilibrium structure. In studying this quantity, one can therefore tell which structure is the most stable at equilibrium.

4.5 Structural Phase Transformations

Application of pressure on a solid may induce a change of structure which may occur when the atoms reconstruct to form a new lattice, for example, when graphite transforms into diamond or an amorphous solid changes into a crystalline form. The stability of a particular crystal structure is defined by means of its Gibbs free energy

$$G(P,T) = E_{coh}(P) + PV - TS, \tag{4.12}$$

where E_{coh}, V, and S are the cohesive energy, volume, and total entropy (dominated by the vibrational entropy) of a material at absolute temperature T. When we com-

pare two possible crystal structures, we are interested in the change in Gibbs free energy between the two structures:

$$\Delta G(P,T) = \Delta E_{coh} + P\Delta V - T\Delta S. \tag{4.13}$$

A phase transition occurs when the Gibbs free energy is equal in both phases at the same pressure [25]. In solids, the first two terms tend to be much larger than the entropic contribution from the last term in this expression. Moreover our calculations are performed effectively at zero temperature, so the thermodynamical potential that has to be considered is the change in enthalpy

$$\Delta H(P) = \Delta E_{coh} + P\Delta V. \tag{4.14}$$

The phase transition pressures are then given by the pressures at which the enthalpy $H(P)$ curves for the phases under study cross. The preferred crystal structure is the one with the lowest enthalpy above the transition pressure.

An interesting consequence of Eq. (4.14) is that two crystal structures with different cohesive energies can have the same enthalpy if $\Delta E_{coh} = -P\Delta V$. Also, for any point on the energy-volume curves, the pressure is quantified by

$$P = -\frac{\partial E_{coh}}{\partial V}. \tag{4.15}$$

Comparing this equation with the aforementioned condition, we see that two structures satisfy this condition if they share a common tangent on a plot of ΔE_{coh} as a function of V representing the equation of state for different phases of the same material. This situation is illustrated in Fig. (4.1): Suppose there are at least three

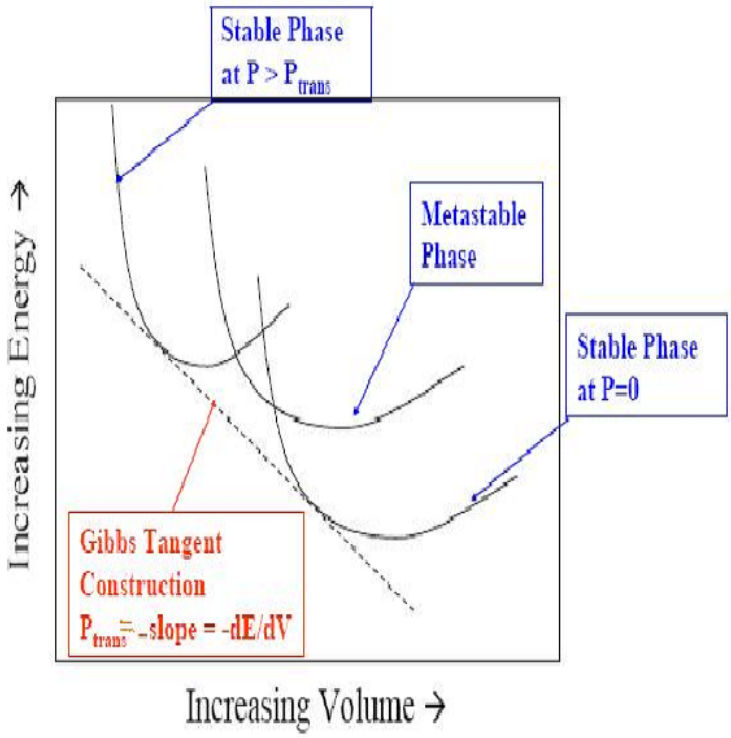

Figure 4.1: A set of energy-volume equations of state for three main phases of a fictitious material. From Ref. [2].

known phases of a particular material as shown. At ambient pressure the system is at its most stable phase with the lowest energy. The pressure, quantified by the negative of the slope $(-dE/dV)$ of the energy-volume curve, is increased until the system transforms into a more energetically favorable phase. The negative of the slope of the common tangent between the curves, $P_{trans} = -slope = -dE/dV$ is the actual transition pressure at which one phase transforms to another [85]. Each phase is defined at the points of common tangency, and any other point between the two tangent points correspond to the energies and volumes of the mixed phase at which

the two phases coexist.

Structural phase transformations are known to occur for a wide range of solids [91]. Figure (4.1) shows how it is possible to use basic quantities such as energy and volume calculated using DFT to predict the existence of pressure-induced phase transitions.

4.6 Electronic Density of States

The electronic density of states (DOS) is one of the primary quantities used to describe the electronic state of a material. It describes the number of states at each energy level that are available to be occupied by electrons. A relationship for the number of available states in a solid can be obtained by considering the electrons in a solid as a free electron gas.

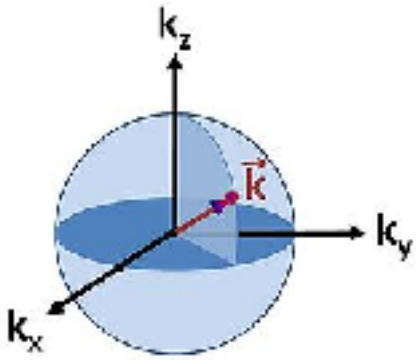

Figure 4.2: Constant energy surface **k**-space for electrons in a 3-dimensional crystalline material with isotropic effective mass.

If we choose to represent the electron state as a vector in **k**-space (Fig. (4.2)) pointing in a direction given by the components magnitudes of the basis vectors, then the energy of the electron is

$$E = \frac{\hbar^2}{2m}\left(k_x^2 + k_y^2 + k_z^2\right) = \frac{\hbar^2 \mid \mathbf{k} \mid^2}{2m}, \tag{4.16}$$

meaning that vectors of the same magnitude have the same energy forming spherical shells. Classically, all values of energy would be allowed and there would be no restriction on the number of electrons with the same value of $\mathbf{k}$. However, at atomic scales, the uncertainty and the exclusion principles come into play, which means that the wavefunction for the electron must satisfy the Schrödinger equation, subject to boundary conditions.

With the DOS the situation is complicated by energy degeneracy. That is, for some of the allowed energy levels, there are more than one possible combination of components in k-space that well give the same energy. In general, the total DOS can be expressed [92, 93] as

$$g\left(E\right) = \frac{2}{V_{BZ}} \sum_n \int_{V_{BZ}} \delta\left(E - E_n\left(\mathbf{k}\right)\right) d\mathbf{k}, \tag{4.17}$$

where V_{BZ} is the Brillouin zone volume and n is the band index. The sum of Eq. (4.17) is over all energy bands and the integral is over all k-points in the Brillouin zone, while the factor of two accounts for spin-up and spin down.

For a system such as ZnO, built out of two atom types it is desirable to express the relative contribution of the atoms to the total DOS by calculating the projected density of states for each atom. The projected DOS of the atom of type t is given by

$$g_l^t\left(E\right) = \frac{2}{V_{BZ}} \sum_n \int_{BZ} Q_l^t\left(\mathbf{k}\right) \delta\left(E - E_n\left(\mathbf{k}\right)\right) d\mathbf{k}, \tag{4.18}$$

where Q_l^t is the partial charge of atom and l is the atomic orbital index. When plots of the projected DOS are matched with the plots of the total DOS, it can be shown

which atom and which orbital delivers the biggest contribution to the total DOS of the system.

4.7 Electronic Band Structure and Band Gap

The electronic DOS condenses the properties of the electronic states for all possible positions in reciprocal space into a simple form. However, a more detailed view of a material's electronic structure is often possible by examination of its band structure from which the band gap can be evaluated. The band structure represents the energy of the available electronic states along a series of lines in reciprocal space that typically form a closed loop beginning and ending at the Γ point. Plane-wave calculations for band structure diagrams require special attention to the placement of k-points. The electronic states must be evaluated as a series of k-points spaced close together along the special directions in reciprocal space relevant for the type of lattice under study.

The properties of the band gap in semiconductors often control the applicability of these materials in practical applications. The band gap of an N electron system is defined [10, 22] as the difference between the electron affinity $A = E_i^{(0)} - E_{i+1}^{(0)} \equiv -\varepsilon_{LUMO}$ and the ionization potential $I = E_{i-1}^{(0)} - E_i^{(0)} \equiv -\varepsilon_{HOMO}$:

$$E_{gap} = I - A = \varepsilon_{LUMO} - \varepsilon_{HOMO}, \tag{4.19}$$

where HOMO and LUMO refer to highest occupied and lowest unoccupied molecular orbital respectively. This is just the difference between two single-electron removal / addition energies, so it should be addressed by many-body pertubation theory. Using Kohn-Sham (KS) DFT, E_{gap} can be evaluated through the expression

$$E_{gap} = \varepsilon_{i+1}^{KS}(N+1) - \varepsilon_i^{KS}(N), \tag{4.20}$$

where $\varepsilon_i^{KS}(N)$ is the i^{th} Kohn-Sham level of the N-electron system. $\varepsilon_{i+1}^{KS}(N+1)$ is the energy of the highest occupied KS orbital of the $N+1$ electron system, and $\varepsilon_i^{KS}(N)$ is the highest occupied KS orbital of the KS N-particle system. This expression arises from the fact that the affinity of an N electron system is the opposite of the ionization potential of the $N+1$ electrons, and that the KS HOMO level equals the negative of the actual ionization potential - being the only KS orbital energy with an explicit physical meaning [94].

For a non-interacting system with insulating ground state, the gap can be readily written in terms of its orbital energies. Therefore, for the fictitious N electron system the difference $I - A$ is calculated as

$$E_{gap}^{KS} = \varepsilon_{i+1}^{KS}(N) - \varepsilon_i^{KS}(N). \tag{4.21}$$

From Eqs. (4.20) and (4.21), we see that the actual and KS gap are related through

$$E_{gap} = (\varepsilon_{i+1}^{KS}(N) - \varepsilon_i^{KS}(N)) + (\varepsilon_{i+1}^{KS}(N+1) - \varepsilon_{i+1}^{KS}(N)) \equiv E_{gap}^{KS} + \Delta_{xc}. \tag{4.22}$$

Here, Δ_{xc} is just the difference between the energies of the $(i+1)$-th orbitals of the KS system that corresponds to the neutral and ionized electron systems [22]. This difference between the Kohn-Sham gap and the fundamental gap $\Delta_{xc} = E_{gap} - E_{gap}^{KS}$ is the consequence of a position independent derivative discontinuity in the exchange correlation potential $v_{xc}(\mathbf{r}) = \frac{\delta E_{xc}}{\delta n(\mathbf{r})}$ when the particle number changes through an integer number [8, 95]. This makes determining the fundamental gap within DFT a

very difficult task. In fact, Δ_{xc} accounts for about 80% of the LDA band gap error for typical semiconductors and insulators [94]. This result was confirmed by Knorr and Godby for a family of model semiconductors [96,97]. In the next chapter a post-DFT method will be discussed that in principle will yield the correct gap.

4.8 Charge Analysis

In order to obtain insight into electronic density reorganization upon the structural phase transitions, the electronic structure can be further studied by electron density population analysis. Determination of atomic charges in molecules and solids is ambiguous since atomic charges are not observables and, therefore not defined by quantum mechanical operator. Several methods have been proposed, some based on atomic orbitals and others based on only the charge density distribution.

Mulliken charge population analysis [98] has been widely applied when atom-centered basis functions are used in the calculation of the electronic wavefunction of the system. Although it can be a fast and useful way of determining atomic charges, the Mulliken charge method has a significant drawback arising from a weak theoretical basis. Further, the analysis is sensitive to the choice of basis set.

Recently, the Bader (or atom-in-molecule - AIM) charge analysis method [99,100] has become the method of choice. This method partitions the three-dimensional space into separate volumes, each of which is usually associated with one atom which is assigned the charge confined in the volume. The (Bader) volumes are separated by (zero flux) surfaces which are minima with respect to the electron density. The zero flux surface is defined as

$$\nabla\rho(\vec{r})\cdot\vec{n} = 0 \tag{4.23}$$

where $\rho(\vec{r})$ is the electron density and $\vec{n}$ is a a unit vector normal to the electron density surface. The Bader charge is then obtained by integrating the volume surrounded by the zero flux surface around each nucleus of the atom:

$$Q_A^{Bader} = Z_A - \int_{Bader\ vol} \rho(\vec{r}) d\vec{r} \tag{4.24}$$

where Z_A is the number of valence electrons of atom A.

Three significant advantages of the Bader analysis method are well documented [99, 101]: (i) The method has a firm theoretical basis. Properties of the atoms are obtained by integration of the proper operator within the atomic volume, and the sum of the atomic properties yields the total system property. (ii) The partitioning of the system is unbiased with respect to the method of obtaining the electron density. (iii) The electron density is an observable and results may be experimentally verified.

Despite its simplicity and the aforementioned advantages, the Bader analysis method has some disadavantages [10]: overlapping between atoms is forbidden, transferability is necessarily limited, and the chemical bond itself seems to have disappeared into thin air.

The Bader charge analysis method is employed in chapter 7 to study the amount of charge transfer upon phase transitions for different structures of ZnO.

Chapter 5

The GW Approximation

In chapter 4, it has been shown that DFT is often the best method of choice when one is interested in the ground-state properties of a many-body system. Moreover, since the solution of the Kohn-Sham (KS) equation gives the entire spectrum of single-particle states for the fictitious KS system, it is tempting to interpret the corresponding eigenvalues as excitation energies. Strictly speaking, such an interpretation is wrong: the KS wave functions and eigenvalues must be considered as mathematical tools and have no physical meaning. The only exception is the energy of the highest occupied state, which equals the chemical potential or negative of the ionization potential [95,102]. Although it is often qualitatively correct, the DFT band structure does not give reliable quantitative values for band gaps of insulators and semiconductors such as ZnO.

Nevertheless, DFT results are good ingredients for further electronic structure calculations. Starting from the pioneering work of Hybertsen and Louie [103, 104] and Godby *et al.* [105,106], KS eigenvalues and eigenfunctions are used in conjunction with Green function techniques to construct the electronic self energy in the so-called quasiparticle GW approximation [107].

5.1 Quasiparticle equations

A successful approximation for the determination of excited states is based on the quasiparticle concept and the Green's function method. The Coulomb repulsion between electrons leads to a depletion of negative charge around a given electron, and the ensemble of this electron and its surrounding charge forms a quasiparticle. Thus, a quasiparticle is simply an electron and its screening cloud. In the GW formalism, the quasiparticle (QP) energies $E^{QP}_{n\mathbf{k}}$ and wavefunctions $\Psi^{QP}_{n\mathbf{k}}$ are obtained by solving the QP equation [108]:

$$(\hat{T} + V_{n-e} + V_H)\Psi^{QP}_{n\mathbf{k}}(\mathbf{r}) + \int d^3\mathbf{r}' \sum(\mathbf{r}, \mathbf{r}', E^{QP}_{n\mathbf{k}})\Psi^{QP}_{n\mathbf{k}}(\mathbf{r}') = E^{QP}_{n\mathbf{k}}\Psi^{QP}_{n\mathbf{k}}(\mathbf{r}), \tag{5.1}$$

which is formally similar to the KS equation for the ground-state properties

$$(\hat{T} + V_{n-e} + V_H)\Psi^{DFT}_{n\mathbf{k}}(\mathbf{r}) + V_{xc}(\mathbf{r})\Psi^{DFT}_{n\mathbf{k}}(\mathbf{r}) = E^{DFT}_{n\mathbf{k}}\Psi^{DFT}_{n\mathbf{k}}(\mathbf{r}). \tag{5.2}$$

Here $\hat{T}$ is the kinetic energy operator, V_{n-e} is the potential due to the nuclei, V_H is the Hartree potential, and n and $\mathbf{k}$ the band and k-point indices. Within the GW approximation, the KS exchange-correlation potential $V_{xc}(\mathbf{r})$ is replaced by a non-local, non-Hermitian and frequency ω dependent self-energy operator $\sum$ which describes many body pertubation exchange and correlation effects beyond the Hartree approximation. The self-energy has the form

$$\sum\nolimits^{GW}_{xc}(\mathbf{r}, \mathbf{r}', \omega) = \frac{i}{2\pi}\int_{-\infty}^{\infty} e^{i\delta\omega'} G(\mathbf{r}, \mathbf{r}', \omega + \omega')W(\mathbf{r}, \mathbf{r}', \omega')d\omega', \tag{5.3}$$

where G denotes the single-particle Green's function whose poles are the desired single-particle excitation energies, and δ is an infinitesimal positive time. The Green's function can be expressed in terms of the QP wave functions and energies [104] as

$$G(\mathbf{r}, \mathbf{r}', \omega) = \sum_{n\mathbf{k}} \frac{\Psi^{QP}_{n\mathbf{k}}(\mathbf{r})\Psi^{*QP}_{n\mathbf{k}}(\mathbf{r}')}{\omega - E^{QP}_{n\mathbf{k}} - i\delta_{n\mathbf{k}}}, \tag{5.4}$$

with $\Psi^{QP}_{n\mathbf{k}}(\mathbf{r})$ and $E^{QP}_{n\mathbf{k}}$ as solutions of Eq. (5.1). The quasiparticles are assumed to interact via the dynamically screened Coulomb interaction $W(\mathbf{r}, \mathbf{r}', \omega)$, which is considerably weaker than the bare Coulomb interaction. An expression for the Coulomb interaction W is given in terms of the dielectric function in section 5.3.1.

5.2 Self-consistency in GW

GW calculations can be performed to different levels of self-consistency. By approximating the eigenstates of the QP equation (5.1) with DFT wave functions, the QP energies are calculated to first order from the diagonal matrix elements of the QP equation [103, 108]

$$E^{QP}_{n\mathbf{k}} = \mathrm{Re}\left[\langle \Psi^{QP}_{n\mathbf{k}} \left| \hat{T} + V_{n-e} + V_H + \sum(E^{QP}_{n\mathbf{k}}) \right| \Psi^{QP}_{n\mathbf{k}} \rangle\right] \tag{5.5}$$

with quantities as described in the preceding section. This equation must be solved by iteration, since it already requires the value of $E^{QP}_{n\mathbf{k}}$. An update of the QP energy ($E^{N+1}_{n\mathbf{k}}$) is then obtained from the QP energy at the previous iteration ($E^{N}_{n\mathbf{k}}$) by linear expansion of Eq. (5.5) such that

$$E^{N+1}_{n\mathbf{k}} = E^{N}_{n\mathbf{k}} + Z_{n\mathbf{k}}\,\mathrm{Re}\left[\langle \Psi^{QP}_{n\mathbf{k}} \left| \hat{T} + V_{n-e} + V_H + \sum(E^{QP}_{n\mathbf{k}}) \right| \Psi^{QP}_{n\mathbf{k}} \rangle - E^{N}_{n\mathbf{k}}\right], \tag{5.6}$$

where $Z_{n\mathbf{k}}$ is the renormalization factor. It is worth noting that the superscript N in the preceeding equation refers to the iteration number, and should not be confused with the particle number used in chapter 4. The renormalization factor is calculated as

$$Z_{n\mathbf{k}} = \left(1 - \mathrm{Re}\langle \Psi^{QP}_{n\mathbf{k}} \mid (\frac{\partial}{\partial} \sum(\omega) \mid_{E^N_{n\mathbf{k}}}) \mid \Psi^{QP}_{n\mathbf{k}} \rangle \right)^{-1}. \tag{5.7}$$

In the single-shot (non-self-consistent) GW approximation (G_0W_0), G_0 and W_0 are calculated using standard or hybrid DFT eigenvalues and eigenfunctions. The quasiparticle energies are therefore obtained using a single iteration, i.e. setting $E^1_{n\mathbf{k}} = E^{DFT}_{n\mathbf{k}}$ in Eq. (5.6). Partially self-consistent (GW_0) [109, 110] calculations are done by performing several iterations and updating the eigenvalues only in the calculation of G until self-consistency is reached. Full self-consistent (scGW) [110] are performed by updating the wavefunctions and eigenvalues in the calculation of G and W.

5.3 Numerical Implementation

The primary task of a GW calculation lies in the evaluation of the self-energy operator $\sum$ required to solve Eq. (5.1). In principle, $\sum$ should be obtained together with G in a self-consistent procedure. They are coupled together with the screened Coulomb interaction W and a vertex function Γ by a set of integral equations now popularly referred to as the "Hedin Equations" [107]. Hedin equations may be viewed as matrix multiplications over the space-spin-time coordinates, and may be expressed for notational simplicity as

$$\sum = iGW\Gamma, \quad W = v + W\chi v$$

$$\chi = -iGG\Gamma, \quad \Gamma = 1 + \frac{\delta \sum}{\delta G} GG\Gamma \tag{5.8}$$

where v denotes the bare Coulomb potential and χ the polarizability.

5.3.1 Polarizability and the dielectric matrix

The simplest implementation of GW method in VASP [108] approximates the vertex function by $\Gamma = 1$ (i.e. excludes the vertex correction), corresponding to the random phase approximation (RPA). Details about the RPA, and derivations of the dielectric function (also called *Lindhard dielectric function*) and the response function (*Linhard function*) can be found in references [111] and [112].

The screened Coulomb interaction is calculated from a matrix multiplication of the inverse dielectric function ϵ^{-1} with the bare Coulomb matrix:

$$W_{\mathbf{q}}(\mathbf{G}, \mathbf{G}', \omega) = 4\pi e^2 \frac{1}{\mid \mathbf{q} + \mathbf{G} \mid} \epsilon^{-1}_{\mathbf{q}}(\mathbf{G}, \mathbf{G}', \omega) \frac{1}{\mid \mathbf{q} + \mathbf{G}' \mid} \tag{5.9}$$

where $\mathbf{G}$ and $\mathbf{G}'$ are the reciprocal lattice vectors, and $\mathbf{q}$ stands for the wave vector in the Brillouin zone. The dielectric matrix is evaluated in the random phase approximation as

$$\epsilon_{\mathbf{q}}(\mathbf{G}, \mathbf{G}', \omega) = \delta_{\mathbf{G},\mathbf{G}'} - \frac{4\pi e^2}{\mid \mathbf{q} + \mathbf{G} \mid\mid \mathbf{q} + \mathbf{G}' \mid} \chi^0_{\mathbf{q}}(\mathbf{G}, \mathbf{G}', \omega). \tag{5.10}$$

The matrix $\chi^0_{\mathbf{q}}(\mathbf{G}, \mathbf{G}', \omega)$ is the independent particle polarizability,

$$\chi^0_{\mathbf{q}}(\mathbf{G},\mathbf{G}',\omega) = \frac{1}{\Omega}\sum_{nn'\mathbf{k}} 2w_{\mathbf{k}}(f_{n'\mathbf{k}-\mathbf{q}} - f_{n\mathbf{k}}) \times \frac{\langle \Psi_{n'\mathbf{k}-\mathbf{q}} \left| e^{-i(\mathbf{q}+\mathbf{G})\mathbf{r}} \right| \Psi_{n\mathbf{k}} \rangle \langle \Psi_{n\mathbf{k}} \left| e^{i(\mathbf{q}+\mathbf{G}')\mathbf{r}'} \right| \Psi_{n'\mathbf{k}-\mathbf{q}} \rangle}{\omega + \epsilon_{n'\mathbf{k}-\mathbf{q}} - \epsilon_{n\mathbf{k}} + i\eta \; sgn\left[\epsilon_{n'\mathbf{k}-\mathbf{q}} - \epsilon_{n\mathbf{k}}\right]}. \quad (5.11)$$

In this expression, Ω is the volume of the primitive cell, $w_{\mathbf{k}}$ is the k-point weight, a factor 2 accounts for a spin-degenerate system, $f_{n'\mathbf{k}-\mathbf{q}}$ and $f_{n\mathbf{k}}$ are the one electron occupancies of the corresponding state. $\epsilon_{n'\mathbf{k}-\mathbf{q}}$ and $\epsilon_{n\mathbf{k}}$ are the energies of the one electron states $\mid \Psi_{n'\mathbf{k}-\mathbf{q}}\rangle$ and $\mid \Psi_{n\mathbf{k}}\rangle$ respectively, and η is an infinitesimal complex shift.

In principle, the summation in Eq. (5.11) must be performed over all possible pairs of occupied and empty states, for each frequency of the chosen frequency grid. This makes the calculation of polarization matrix very time-consuming. However, spectral representation of the polarizability is used to optimize the computational procedure. Details of the implementation are given in reference [108]. Accordingly, the spectral representation is calculated as

$$\chi^S_{\mathbf{q}}(\mathbf{G},\mathbf{G}',\omega) = \frac{1}{\Omega}\sum_{nn'\mathbf{k}} 2w_{\mathbf{k}} \; sgn(\omega')\delta(\omega' + \epsilon_{n\mathbf{k}} - \epsilon_{n'\mathbf{k}-\mathbf{q}}) \times (f_{n\mathbf{k}} - f_{n'\mathbf{k}-\mathbf{q}}) \langle \Psi_{n'\mathbf{k}-\mathbf{q}} \left| e^{-i(\mathbf{q}+\mathbf{G})\mathbf{r}} \right| \Psi_{n\mathbf{k}} \rangle \times \langle \Psi_{n\mathbf{k}} \left| e^{i(\mathbf{q}+\mathbf{G}')\mathbf{r}'} \right| \Psi_{n'\mathbf{k}-\mathbf{q}} \rangle. \quad (5.12)$$

The spectral function and the imaginary part of the polarizability are related through

$$\chi^S_{\mathbf{q}}(\mathbf{G},\mathbf{G}',\omega) = \frac{1}{\pi} \operatorname{Im} \chi^0_{\mathbf{q}}(\mathbf{G},\mathbf{G}',\omega). \quad (5.13)$$

In the spectral representation, the summation is carried out over only the states that satisfy the criteria $\omega' + \epsilon_{n\mathbf{k}} - \epsilon_{n'\mathbf{k}-\mathbf{q}} = 0$ for a given frequency ω, thus evaluating the spectral function is rather efficient. The real part of the polarizability is obtained by means of a Kramers-Kronig transformation:

$$\chi^0_{\mathbf{q}}(\mathbf{G}, \mathbf{G}', \omega) = \int_0^\infty d\omega' \chi^S_{\mathbf{q}}(\mathbf{G}, \mathbf{G}', \omega) \times \left(\frac{1}{\omega - \omega' - i\eta} - \frac{1}{\omega + \omega' + i\eta}\right) \tag{5.14}$$

with frequencies ω and ω' chosen from the same set.

5.3.2 Evaluation of self-energy

A solution of the quasiparticle equation (5.5) still requires the knowledge of the frequency dependence of the self-energy $\sum(\omega)$. In the simplest implementation, the diagonal matrix elements of the self-energy matrix are calculated as

$$\begin{aligned} \langle \Psi_{n\mathbf{k}} | \textstyle\sum(\omega) | \Psi_{n\mathbf{k}} \rangle &= \frac{1}{\Omega} \sum_{\mathbf{q}\mathbf{G}\mathbf{G}'} \sum_{n'} \frac{i}{2\pi} \int_{-\infty}^{\infty} d\omega' W(\mathbf{G}, \mathbf{G}', \omega') \\ &\times \left\langle \Psi_{n\mathbf{k}} \left| e^{i(\mathbf{q}+\mathbf{G})\mathbf{r}} \right| \Psi_{n'\mathbf{k}-\mathbf{q}} \right\rangle \left\langle \Psi_{n'\mathbf{k}-\mathbf{q}} \left| e^{-i(\mathbf{q}+\mathbf{G}')\mathbf{r}'} \right| \Psi_{n\mathbf{k}} \right\rangle \\ &\times \frac{1}{\omega + \omega' - \epsilon_{n'\mathbf{k}-\mathbf{q}} + i\eta \; sgn\left[\epsilon_{n'\mathbf{k}-\mathbf{q}} - \mu\right]}, \end{aligned} \tag{5.15}$$

where μ is the Fermi energy, and W is the dynamically screened potential calculated in the random phase approximation in accord with Eq. (5.9). The Green's function required by Eq. (5.3) is never explicitly stored or evaluated [108]. The frequency grid is restricted to positive values noting that W is an even function of ω', whereas the Green's function is an odd function of ω'. Like the polarization equation (5.11), evaluation of the self energy matrix is computationally demanding.

To evaluate the self-energy with relatively simple effort, all $\mathbf{G}$ and $\mathbf{G}'$-dependent quantities in the preceding equation can be contracted in a summation over $\mathbf{G}$ and $\mathbf{G}'$,

$$\begin{aligned}\Lambda_{n\mathbf{k},n'\mathbf{k}-\mathbf{q}}(\omega') &= \frac{1}{\Omega}\sum_{\mathbf{G}\mathbf{G}'} W_{\mathbf{q}}(\mathbf{G},\mathbf{G}',\omega') \\ &\times \left\langle \Psi_{n\mathbf{k}} \left| e^{i(\mathbf{q}+\mathbf{G})\mathbf{r}} \right| \Psi_{n'\mathbf{k}-\mathbf{q}} \right\rangle \left\langle \Psi_{n'\mathbf{k}-\mathbf{q}} \left| e^{-i(\mathbf{q}+\mathbf{G}')\mathbf{r}'} \right| \Psi_{n\mathbf{k}} \right\rangle . \quad (5.16)\end{aligned}$$

The self-energy is then evaluated as a Hilbert transform of the function $\Lambda_{n\mathbf{k},n'\mathbf{k}-\mathbf{q}}(\omega')$,

$$\sum(\omega)_{n\mathbf{k},n\mathbf{k}} = \sum_{n'} \frac{i}{2\pi}\int_{-\infty}^{\infty} d\omega' \times \frac{\Lambda_{n\mathbf{k},n'\mathbf{k}-\mathbf{q}}(\omega')}{\omega+\omega'-\epsilon_{n'\mathbf{k}-\mathbf{q}}+i\eta\ sgn(\epsilon_{n'\mathbf{k}-\mathbf{q}}-\mu)}. \quad (5.17)$$

Determination of the quasiparticle energies is in fact dominated by calculation of the function Λ, and therefore savings must concern this part in order to be effective [108]. This procedure is followed if the full frequency-dependent self-energy is required.

Another approach to the self-energy reverses the order of execution in the preceding paragraph and starts from the Hilbert transform of the frequency dependent screened interaction $W_{\mathbf{q}}(\mathbf{G},\mathbf{G}',\omega')$:

$$C_{n\mathbf{k},n'\mathbf{k}-\mathbf{q}}(\mathbf{G},\mathbf{G}',\omega) = \frac{i}{2\pi}\int_{-\infty}^{\infty} d\omega' \times \frac{W_{\mathbf{q}}(\mathbf{G},\mathbf{G}',\omega')}{\omega+\omega'-\epsilon_{n'\mathbf{k}-\mathbf{q}}+i\eta\ sgn(\epsilon_{n'\mathbf{k}-\mathbf{q}}-\mu)}, \quad (5.18)$$

and ends with a final evaluation of the self-energy using a similar equation as in Eq. (5.16). Unfortunately this approach requires a Hilbert transform of the matrix $W(w')$ for each state $n'\mathbf{k}-\mathbf{q}$, which possess more elements than $\Lambda_{n\mathbf{k},n'\mathbf{k}-\mathbf{q}}(\omega')$, and

is therefore more time-consuming.

An alternative approach followed by Shishkin and Kresse [108], is to substitute $\bar{\omega} = \omega - \epsilon_{n'\mathbf{k}-\mathbf{q}}$ and carry out the Hilbert transform only once for positive and negative complex shifts as

$$C^{\pm}_{\mathbf{q}}\left(\mathbf{G},\mathbf{G}',\bar{\omega}\right) = \frac{i}{2\pi}\int_0^{\infty} d\omega' W_{\mathbf{q}}\left(\mathbf{G},\mathbf{G}',\omega'\right) \times \left(\frac{1}{\bar{\omega}+\omega' \pm i\eta} + \frac{1}{\bar{\omega}-\omega' \pm i\eta}\right). \quad (5.19)$$

In contrast to Eq. (5.18), this approach does not require to take a Hilbert transform for each state n', and is therefore expected to be more efficient. The screened two-electron integrals are defined for each matrix $C^{+}_{\mathbf{q}}\left(\mathbf{G},\mathbf{G}',\bar{\omega}\right)$ and $C^{-}_{\mathbf{q}}\left(\mathbf{G},\mathbf{G}',\bar{\omega}\right)$, as

$$\begin{aligned} S^{\pm}_{n\mathbf{k},n'\mathbf{k}-\mathbf{q}}\left(\bar{\omega}\right) &= \frac{1}{\Omega}\sum_{\mathbf{G}\mathbf{G}'} C^{\pm}_{\mathbf{q}}\left(\mathbf{G},\mathbf{G}',\bar{\omega}\right) \\ &\quad \times \left\langle \Psi_{n\mathbf{k}} \left| e^{i(\mathbf{q}+\mathbf{G})\mathbf{r}} \right| \Psi_{n'\mathbf{k}-\mathbf{q}} \right\rangle \left\langle \Psi_{n'\mathbf{k}-\mathbf{q}} \left| e^{-i(\mathbf{q}+\mathbf{G}')\mathbf{r}'} \right| \Psi_{n\mathbf{k}} \right\rangle. \quad (5.20) \end{aligned}$$

Finally, the self-energy at $\epsilon_{n\mathbf{k}}$ can be calculated as a sum of these screened two-electron integrals

$$\begin{aligned} \left\langle \Psi_{n\mathbf{k}} \left| \sum\left(\epsilon_{n\mathbf{k}}\right) \right| \Psi_{n\mathbf{k}} \right\rangle &= \sum_{n'\mathbf{k}-\mathbf{q}} sgn\left(\epsilon_{n\mathbf{k}} - \epsilon_{n'\mathbf{k}-\mathbf{q}}\right) \\ &\quad \times S^{sgn\left(\epsilon_{n'\mathbf{k}-\mathbf{q}}-\mu\right)sgn\left(\epsilon_{n\mathbf{k}}-\epsilon_{n'\mathbf{k}-\mathbf{q}}\right)}_{n\mathbf{k},n'\mathbf{k}-\mathbf{q}}\left(\left|\epsilon_{n\mathbf{k}} - \epsilon_{n'\mathbf{k}-\mathbf{q}}\right|\right). \quad (5.21) \end{aligned}$$

5.4 GW Procedure

In summary, quasiparticle GW calculations are performed by solving Eqs. (5.9) to (5.15) through matrix operations in the following order: First, the Kohn-Sham wave functions $\Psi_{n\mathbf{k}}^{DFT}$ and energies $E_{n\mathbf{k}}^{DFT}$ are produced from a self consistent DFT loop. The polarization matrix $\chi_{\mathbf{q}}^{0}(\mathbf{G},\mathbf{G}',\omega)$ is calculated according to spectral functions of Eq. (5.11). Then the dielectric matrix $\epsilon_{\mathbf{q}}(\mathbf{G},\mathbf{G}',\omega)$ is calculated in the random phase approximation by means of Eq. (5.10) and inverted. Next the screened interaction $W_{\mathbf{q}}(\mathbf{G},\mathbf{G}',\omega)$ is obtained from a matrix multiplication of the inverse dielectric function with the bare Coulomb matrix as in Eq. (5.9). This is then used to evaluate the self-energy $\sum(\omega)$ by means of Hilbert transforms through various procedures described in the previous subsection. Finally, approximate quasiparticle energies are obtained from Eqs. (5.6) and (5.7).

The success of GW approach and the effect of different degrees of self-consistency (G_0W_0, GW_0, and scGW) on determining energy band gaps has been investigated by Shishkin and Kresse [108,113,114] for a representative selection of materials including ZnO. Contrary to a widespread belief based on pseudopotential calculations, it has been demonstrated that the single-shot G_0W_0 approximation based on LDA or GGA eigenstates underestimates the gaps for practically all materials [108].

Partially self-consistent GW_0 calculations [114] yield band gaps that are in excellent agreement with experiment, with typical errors being around 3% - 5%. However, for materials with shallow d-states the band gaps are underestimated typically by 10% with the largest deviation (25%) observed for ZnO. It has been shown that this underestimation is due to an overestimation of the calculated static dielectric constant in the random phase approximation.

Unfortunately, despite its huge computational expense, the completely self-consistent

GW (scGW) approach yields consistently too large band gaps [114], except for materials with shallow d-states. van Schilfgaarde *et al.* [115] have pointed out that this is related to the neglect of the attractive Coulomb interaction between electrons and holes, which can be included in scGW calculations via vertex corrections in W.

Self-consistent GW approach with vertex corrections has been implemented in the VASP code by Shishkin and Kresse [113]. It has been demonstrated that this approach corrects the overestimation of the band gaps in the scGW approximation. An exception are again the materials with shallow d-states such as ZnO, as in the GW_0 approximation. Therefore, it is an important result that GW_0 band gaps agree very well with the vertex-corrected scGW gaps. This offers a convenient access and legitimizes the use of the less demanding but still accurate GW_0 approximation.

Chapter 6

Structural Properties and Phase Transitions in ZnO

Contrary to other IIB - VIA binary compounds which adopt different metastable structures, bulk ZnO is known to crystallize only in the hexagonal wurtzite (B4) structure under normal conditions. A number of experiments [89,116,117] have shown through different techniques, that the B4 structure transforms into a cubic rocksalt (B1) structure at a pressure in the vicinity of 9 GPa. A recent angular dispersive x-ray diffraction experiment by Liu *et al.* [118] has shown that the B1 phase of ZnO remains stable under high pressure up to 209 GPa at room temperature, being the maximum pressure achieved in any experiment on ZnO so far.

Furthermore, theoretical studies [3, 6, 7] have shown that at pressures around 260 GPa, ZnO undergoes a phase transition from the B1 to the eightfold-coordinated B2 (cubic CsCl) structure, assuming that no other structures appear first. These studies were based on the widely used DFT within the local density and generalized gradient approximations (LDA and GGA), together with Gaussian basis sets and were expected to stimulate corresponding high-pressure experimental work. On the

other hand, an atomistic calculation performed by Zaoui and Sekkal [119] predicted the transition at 305 GPa. However, most of the previous studies on high-pressure behavior of ZnO did not consider any other possible structures, except B4, B3 (cubic zinc blende), B1 and B2. Recently, Azzaz *et al.* [120] investigated the ground-state properties of ZnO on other structures such as cinnabar, d-β-tin and NiAs. First principles lattice dynamics calculation by Li *et al.* [121] also predicted a high-pressure tetragonal PbO-type (B10) structure as an intermediate phase between the B1 and the hypothetical B2 phase. We report herein the equilibrium structural properties and phase transformations for the NaTl (B32), PbO (B10), WC (B_h), BN (B_k), NiAs ($B8_1$) and AsTi (B_i) model structures of ZnO in addition to the most studied four structures. All these structures are shown in appendix B.

6.1 Structural Properties

Calculations of the total energy of ZnO were performed for each of the structures, in order to obtain the equilibrium lattice constants a_0, volume V_0, bulk modulus B_0 and its pressure derivative B_0'. These were carried out for a number of different unit cell volumes and the calculated points were fitted to the third-order Birch-Murnaghan isothermal equation of state (EOS) function [88].

6.1.1 Equilibrium lattice parameter

Table 6.1 displays the calculated lattice parameters and atomic volumes of all nine structures for both the LDA and PBE96-GGA (values shown in brackets) functionals. This table also contains results of previous first principles calculations by Uddin *et. al.* [6] for the B4, B3, B1 and B2 phases as well as experimental [89,117,122] data for

Table 6.1: Third-order Birch-Murnaghan equation-of-state lattice parameters and equilibrium atomic volume for different phases of ZnO calculated with LDA and GGA (values in brackets) functionals.

Structure	V_0 (Å^3/*atom*)	Lattice parameter (Å)		
		This work	Theory[a]	Experiments
B3	11.43 (12.43)	a_0 = 4.505 (4.634)	4.509 (4.637)	4.62[c]
B2	8.97 (9.77)	a_0 = 2.618 (2.693)	2.614 (2.689)	
B1	9.42 (10.23)	a_0 = 4.224 (4.340)	4.218 (4.334)	4.2831[b] 4.271[c] 4.280[d]
B32	9.79 (10.77)	a_0 = 5.391 (5.565)		
B4	11.44 (12.45)	a_0 = 3.209 (3.302)	3.205 (3.295)	3.2498[b] 3.2496[c] 4.2475[d]
		c = 5.128 (5.275)	5.151 (5.297)	5.2066[b] 5.2042[c] 5.2075[d]
B_h	9.55 (10.38)	a_0 = 2.943 (3.025)		
		c = 2.549 (2.618)		
B10		a_0 =3.942 (4.134)		
		c =3.042 (3.160)		
B_k	11.18 (12.04)	a_0 = 3.161 (3.240)		
		c = 5.165 (5.294)		
$B8_1$	9.53 (10.35)	a_0 = 2.975 (3.051)		
		c = 4.971 (5.135)		
B_i	9.38 (10.11)	a_0 = 2.953 (3.025)		
		c = 9.940 (10.206)		

[a]Ref. [6]
[b]Ref. [89]
[c]Ref. [117]
[d]Ref. [122]

comparison. No experimental data are available to compare for the other phases.

In general, LDA yields smaller lattice parameters and unit cell volumes as compared to experiment, meaning that the bonds in between the atoms are stronger. In contrast, GGA overestimates lattice parameters, meaning the bonds between the atoms are weaker. This is a well known feature of the GGA vs LDA approximations and we find it valid for all structures of ZnO studied here. Our LDA and GGA lattice parameters agree to about 3%. The LDA and GGA predictions for the B4, B3, B1, and B2 phases agree very well with the corresponding LDA and GGA values reported in ref. [6], obtained using Gaussian type orbitals basis sets. Smaller differences can be attributed to pseudopotentials, basis sets and other approximations intrinsic to a particular methodology. So far there are no experimental or theoretical results to compare with, for the other phases.

6.1.2 Equilibrium bulk modulus

Table 6.2 shows the bulk moduli B_0 and their pressure derivatives B_0' evaluated at zero pressure. We also compare with the results of Uddin *et. al.* [6] and experiment as in table 6.1. We find a striking agreement between our corresponding LDA and GGA bulk moduli and those of reference [6] for the B4, B3, B1 and B2 phases. The GGA is seen to decrease the bulk modulus compared to the LDA. The softening is consistent with a weaker bonding shown by larger lattice parameters and atomic volumes displayed in table 6.1. The LDA bulk moduli for the B4 and B1 phases are within the available experimental [89,117,122] data. For these phases we find values of 127.5 GPa and 204.9 GPa and which compare very well with the experimental [89,122] values of 136 GPa and 202.5 GPa respectively. The B_0' value is decreased up to 1.3 % by the GGA, except for the AsTi (B_i) structure where the LDA predicts a smaller

Table 6.2: Bulk moduli and their associated pressure derivatives for the phases of ZnO. The subscript 0 shows that the parameters are evaluated at zero pressure. PBE values are given in parentheses.

Structure	Bulk Modulus, B_0 (GPa)			B_0'
	This work	Theory[a]	Experiments	
B3	161.1	154		4.379
	(129.3)	(124)		(4.323)
B2	202.2	201		4.557
	(159.5)	(161)		(4.536)
B1	204.9	203	202.5[b] 228[c] 170[d]	4.549
	(163.4)	(163)		(4.500)
B32	159.9			4.626
	(121.1)			(4.615)
B4	159.4	155	142.6[b] 183[c] 136[d]	4.409
	(127.5)	(124)		(4.372)
B_h	190.1			4.557
	(149.9)			(4.512)
B10	51.5			6.861
	(27.2)			(8.060)
B_k	143.7			4.709
	(127.4)			(4.647)
$B8_1$	199.8			4.638
	(157.2)			(4.637)
B_i	246.9			3.523
	(198.3)			(3.817)

[a]Ref. [6]
[b]Ref. [89]
[c]Ref. [117]
[d]Ref. [122]

value (3.523) than 3.817 predicted by GGA. It is found that the B_i structure has the highest bulk modulus in both LDA and GGA functionals among all the ZnO phases considered.

6.2 Phase Stability

Cohesive energy versus volume calculations give an indication of which of the structures are the best candidates for the most stable phase. Generally, the structure with the lowest equilibrium energy is considered to be the most stable phase. In Figs. 6.1, we show the cohesive energy versus volume curves for ZnO, calculated using the PAW method within the (a) LDA and (b) PBE-GGA functionals. The ZnO cohesive energy (E_{coh}) was found by subtracting the energy of the isolated constituent atoms from the total energy per ZnO formula unit of the crystal at its equilibrium lattice constant as described in chapter 4 (Eq. 4.11).

From the curves it can be noted that the zinc blende (B3) and wurtzite (B4) phases have almost identical stabilities. In order to show the difference in the stability of the B4 and B3 structures we show plots of their total energy minima in Figs. 6.2 for the (a) LDA and (b) GGA functionals. In both cases, it can be seen that the B4 phase is the most stable at zero temperature and pressure. This behavior has also been observed in CdO by Moreno and Takechi [124], and later in MgO by Schleife *et al.* [125]. The B4 and B3 structures have the same local tetrahedral bonding geometry, but they differ only by the stacking in the [001] or [111] direction as pointed out in references [124] and [125].

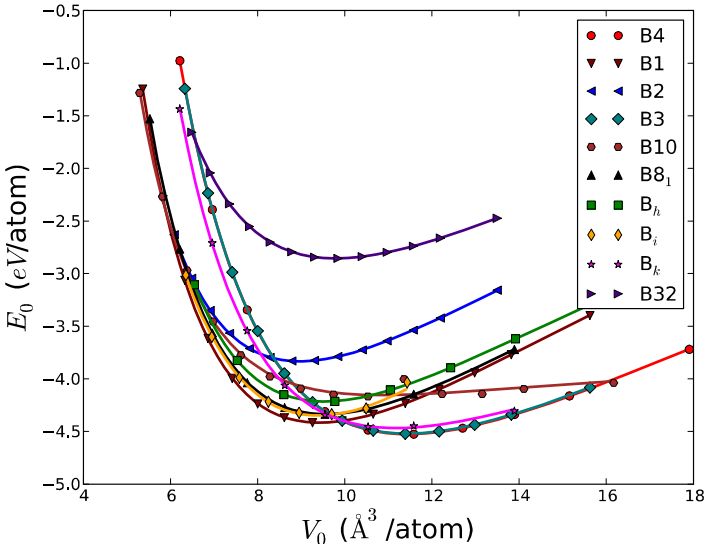

(a) LDA

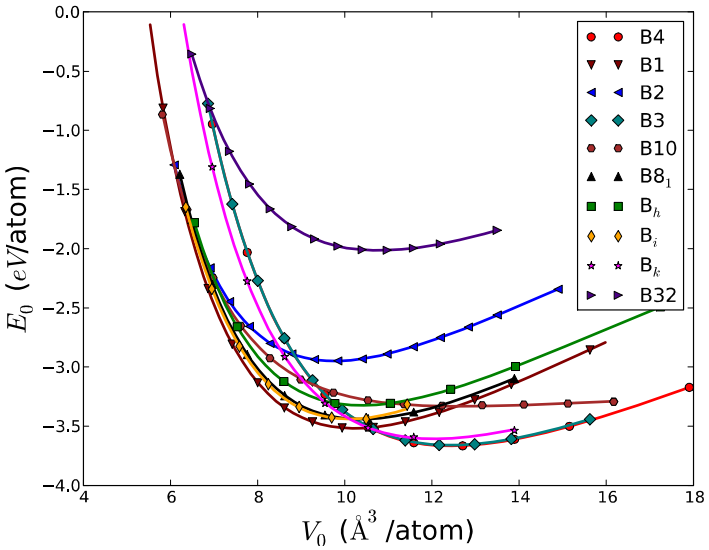

(b) GGA

Figure 6.1: Cohesive energy versus volume for the phases of ZnO with the (a) LDA and (b) GGA functionals. The curves are obtained from the third-order Birch-Murnaghan EOS fitting.

Table 6.3: Calculated equilibrium structural volumes and cohesive energy for various phases of ZnO. Both quantities are expressed per ZnO formula unit.

	This work		Other calculations [3, 120, 123]		
	LDA	GGA	LDA	GGA	
B4 (wurtzite)					
E_{coh} (eV)	9.063	7.337	9.769[a]	7.692[2]	8.835[b]
V_0 (Å^3)	22.8	24.90	22.874[a]	24.834[a]	24.906[b]
B3 (ZnS)					
E_{coh} (eV)	9.043	7.317	9.754[a]	7.679[a]	8.768[b]
V_0 (Å^3)	22.86	24.86	22.914[a]	24.854[a]	24.878[b]
B_k (BN)					
E_{coh} (eV)	8.962	7.216			
V_0 (Å^3)	22.36	24.08			
B1 (rocksalt)					
E_{coh} (eV)	8.843	7.037	9.611[a]	7.455[a]	8.489[b]
V_0 (Å^3)	18.84	20.46	18.904[a]	20.502[a]	20.472[b]
B_i (AsTi)					
E_{coh}(eV)	8.703	6.878			
V_0 (Å^3)	18.76	20.22			
$B8_1$ (NiAs)					
E_{coh} (eV)	8.684	6.876			
V_0 (Å^3)	19.06	20.70	19.18[c]		
B_h (WC)					
E_{coh} (eV)	8.423	6.657			
V_0 (Å^3)	19.10	20.76			
B10 (PbO)					
E_{coh} (eV)	8.336	6.654			
V_0 (Å^3)	21.74	25.08			
B2 (CsCl)					
E_{coh} (eV)	7.663	5.895	8.462[a]	6.337[a]	7.357[b]
V_0 (Å^3)	17.94	19.54	18.073[a]	19.785[a]	19.581[b]
B32 (NaTl)					
E_{coh} (eV)	5.772	4.037			
V_0 (Å^3)	19.58	21.54			

[a]Ref. [3]
[b]Ref. [123]
[c]Ref. [120]

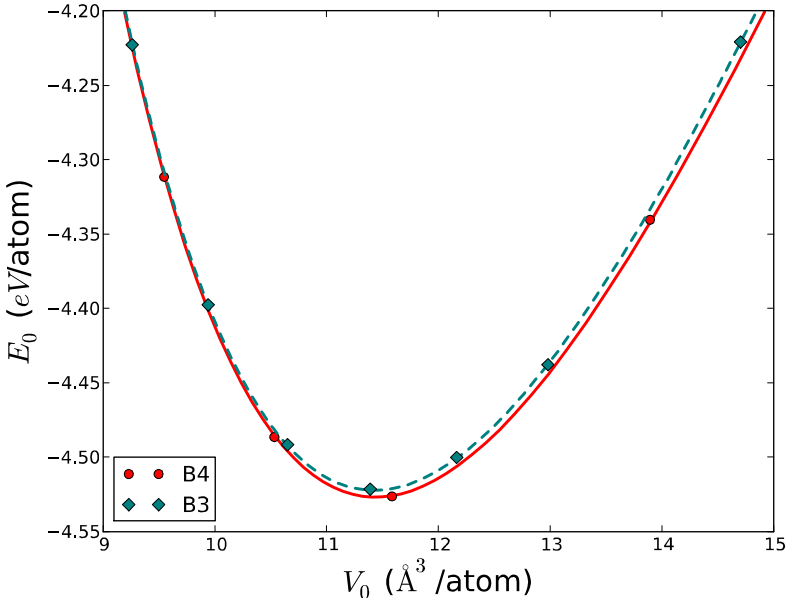

(a) LDA

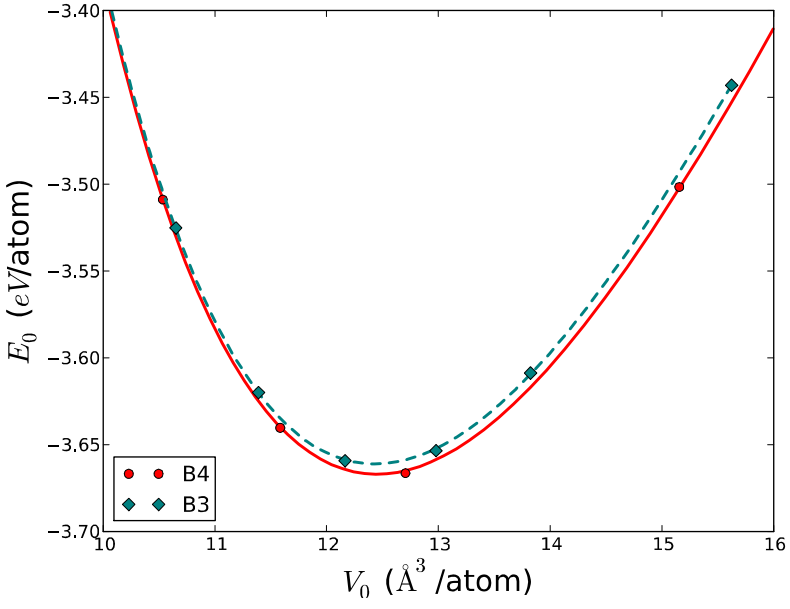

(b) GGA

Figure 6.2: Cohesive energy versus volume per atom for the wurtzite (B4) and zinc blende (B3) phases of ZnO calculated with the (a) LDA and (b) PBE-GGA functionals. B4 is the lowest energy structure, hence the most stable phase at equilibrium.

In agreement with previous theoretical results [3, 6, 126], Fig. 6.1 shows the fact that B4 (wurtzite) is the most energetically stable phase at equilibrium amongst all the phases considered. The NaTl (B32) structure is shown to be less stable than all the other structures at equilibrium. The energy ordering of these phases predicted by both LDA and GGA is $E_{B4} < E_{B3} < E_{B_k} < E_{B1} < E_{B_i} < E_{B8_1} < E_{B_h} < E_{B10} < E_{B2} < E_{B32}$, with B4 and B32 phases being respectively, the most stable and less stable at equilibrium. It is worth noting that most of the phases lie quite close in energy. However, at zero temperature and pressure the other phases may be unlikely to be synthesized.

The cohesive energy and equilibrium volume are compared where available, with theoretical results in table 6.3. The results demonstrate the LDA's typical overestimation of cohesive energies, while volumes are typically underpredicted. In contrast to LDA, the GGA is known to decrease cohesive energies while overestimating the volumes. On the other hand we find excellent agreement between our calculated equilibrium volumes and those reported by Jaffe and coworkers [3] using both LDA and GGA. The calculated cohesive energies agree to within 10 % in the B4, B3, B1 and B2 phases.

6.3 Phase Transition Pressures

In table 6.4, we summarize phase transition pressures obtained by applying the common tangent method on the cohesive energy versus volume plots as explained in section 4.5. However, the enthalpy-pressure phase diagram is a reliable indicator for the phase stability. The lowest-enthalpy structure at a specific pressure is the most stable phase. For ease of data interpretation, we obtain the transition pressure by plotting the enthalpy difference of the structures with respect to one of the phases

under consideration, so that the phase transitions occur at those pressures where the enthalpy difference of two phases coincide. This procedure gives physically equivalent results to the common tangent construction but is numerically more accurate. As shown on table 6.4, values from the enthalpy versus pressure curves (shown in parentheses) agree very well with those obtained from the energy-volume curves. The only available experimental phase transition data in ZnO to date is for the B4→B1 transition.

The LDA predicts a transition from the tetrahedrally coordinated B4 to the six-fold coordinated B1 structure at about 9.20 GPa, which is very close to the experimental [89] value of 9.1 GPa. Above the B4→B1 transition, the B1 structure remains stable over a wide pressure range until a transition (B1→B10) into the tetragonal PbO-type B10 structure is achieved at pressures around 261.5 GPa. The B10 phase then transforms into the eight-fold coordinated B2 structure at a much higher pressure of about 296.5 GPa. The transition sequence B4→B1→B10→B2 is shown on Fig. 6.3.

In the GGA, the B4→B1 transition is predicted at a pressure of 11.51 GPa, in agreement with a similar GGA result of 11.8 GPa reported in reference [127] but larger than 9.32 GPa of reference [3]. Contrary to our LDA result and a recent a*b initio* lattice dynamics GGA calculation by Li *et al* [121], we find no evidence of a B1→B10 phase transition in the GGA. The B1 phase transforms directly to the B2 phase at a pressure of 253.0 GPa, consistent with the corresponding GGA result (256 GPa) of reference [3] without any intermediate phase. This result in B4→B1→B2 transition sequence as shown in Fig. 6.4. In reference [121], the B10 phase is obtained from the B1 phase at 236 GPa while a B1→B10 is obtained at 316 GPa. This discrepancy may be attributed to the different (norm-conserving) pseudopotentials used in their

Table 6.4: Phase transition pressures (GPa) of ZnO obtained by common tangent method. Values from the enthalpy curve crossings are shown in parentheses.

	LDA	GGA	Other LDA / GGA	Exp.
P_T(B4 →B1)	9.08 (9.20)	11.59 (11.51)	6.6 / 9.32 [3]	9.1 [89], 8.7 [117]
V_{B4}(Å^3)	21.72	23.05		
V_{B1}(Å^3)	18.08	19.23		
P_T(B1 →B10)	(261.5)		236 [121]	
V_{B1}(Å^3)	12.00			
V_{B10}(Å^3)	11.49			
P_T(B10 →B2)	(296.5)		/ 316 [121]	
V_{B10}(Å^3)	11.17			
V_{B2}(Å^3)	11.08			
P_T(B1 →B2)	268.3 (267.0)	253.2 (253.0)	260 / 256 [3]	
V_{B1}(Å^3)	11.94	12.45		
V_{B2}()Å^3	11.34	11.84		
P_T(B4 →B$_k$)	27.66 (27.75)	24.35 (24.65)		
V_{B4}(Å^3)	20.08	21.60		
V_{B_k}(Å^3)	19.37	20.87		
P_T(B$_k$ →B$_h$)	30.6 (30.2)	32.36 (32.85)		
V_{B_k}(Å^3)	19.20	20.18		
V_{B_h}(Å^3)	16.90	17.80		
P_T(B$_h$ →B2)	156.9 (156.25)	144.4 (144.8)		
V_{B_h}(Å^3)	13.32	14.01		
V_{B2}(Å^3)	12.67	13.37		
P_T(B$_k$ →B$_i$)	12.19 (12.13)	16.56 (16.53)		
V_{B_k}(Å^3)	20.76	21.69		
V_{B_i}(Å^3)	17.92	18.81		
P_T(B$_i$ →B2)	248.2 (248.0)	213.5 (213.2)		
V_{B_i}(Å^3)	11.86	12.84		
V_{B2}(Å^3)	11.53	12.32		
P_T(B4 →B8$_1$)	17.93 (17.70)	19.60 (19.52)		
V_{B4}(Å^3)	20.08	22.11		
V_{B8_1}(Å^3)	17.72	18.77		
P_T(B8$_1$ →B2)	196.05 (195.70)	183.40 (183.25)		
V_{B8_1}(Å^3)	12.77	13.41		
V_{B2}(Å^3)	12.12	12.73		
P_T(B4 →B32)	230.20 (229.1)	218.9 (219.1)		
V_{B4}(Å^3)	14.08	14.50		
V_{B32}(Å^3)	12.21	12.72		

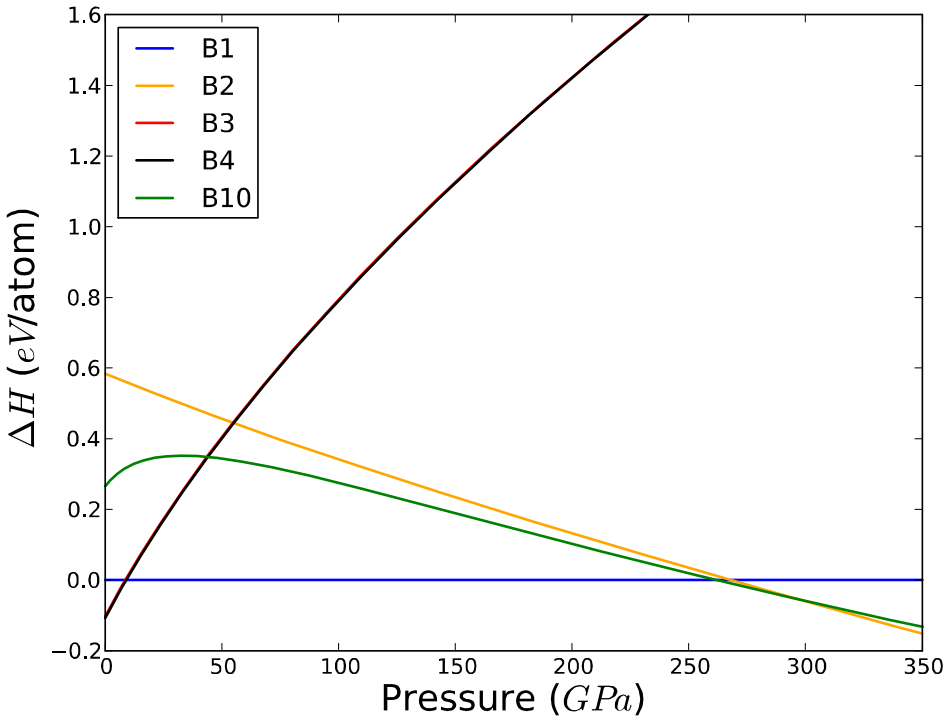

Figure 6.3: The LDA enthalpy differences of B4, B3, B1, B10 and B2 phases of ZnO as a function of pressure showing the B4→B1→B10→B2 phase transition. The B1 phase has been taken as a reference. The B3 overlaps with the B4 curve.

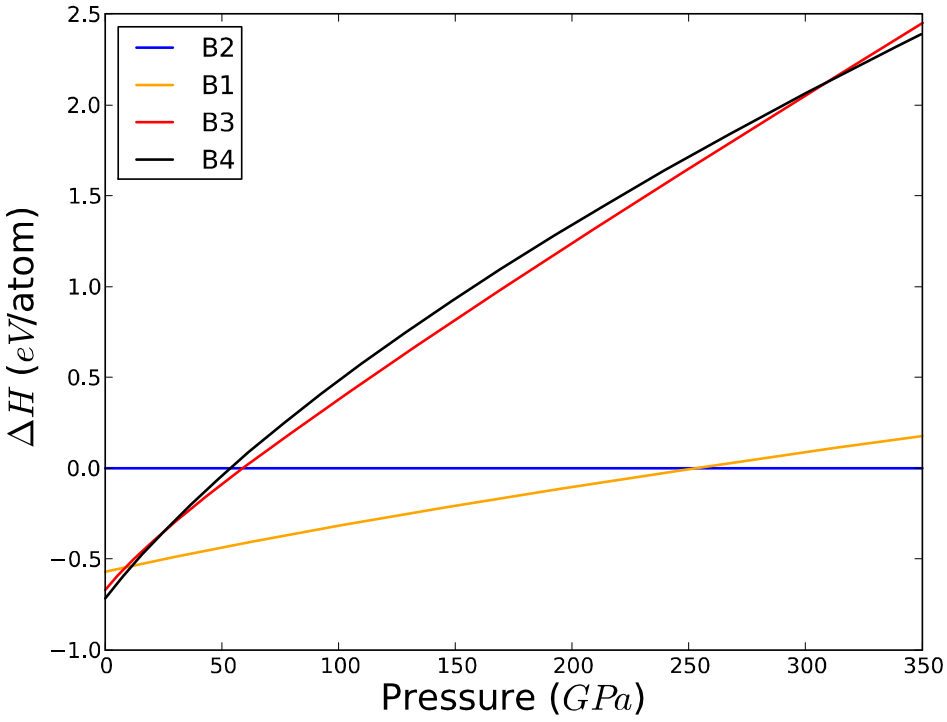

Figure 6.4: The PBE-GGA enthalpy differences of B4, B3, B1 and B2 phases of ZnO as a function of pressure, showing the B4→B1→B2 phase transition. The B2 phase has been taken as a reference.

study.

The B2 phase has never been observed experimentally, perhaps because pressures around 250 GPa are challenging to reach for static high-pressure experimental techniques [128]. Recent angular dispersive x-ray diffraction experiment by Liu *et al.* [118] has shown that the B1 phase of ZnO remains stable under high pressure up to 209 GPa at room temperature, being the maximum pressure attained in any experiment on ZnO to date.

We predict that the low-pressure B4 phase will transform to the high-pressure B2 phase indirectly, with intermediate phases B_k and B_h as pathway, following the

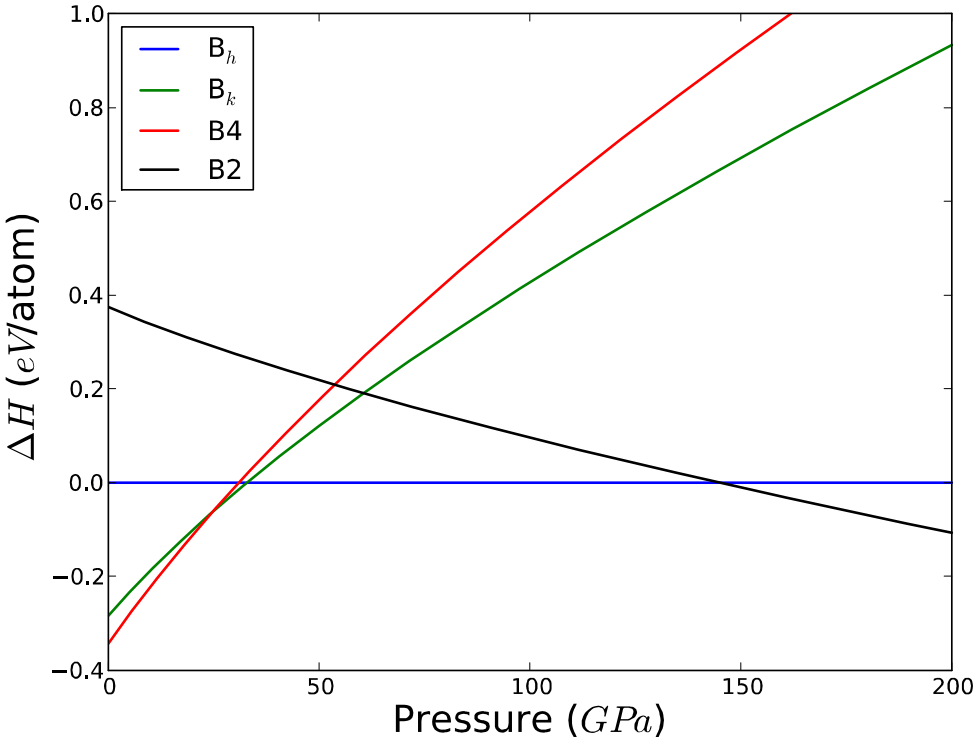

Figure 6.5: The GGA enthalpy differences of B4, B_k, B_h, and B2 phases of ZnO as a function of pressure showing the B4→B_k →B_h →B2 phase transition. The B_h phase has been taken as a reference.

sequence B4→B_k →B_h →B2. These occur at the curve crossings of Fig. 6.5, where ΔH(B4) = ΔH(B_k), ΔH(B_k) = ΔH(B_h) and ΔH(B_h) = ΔH(B2) at about 24.65 GPa, 32.85 GPa and 144.8 GPa respectively, within GGA. It has been reported in reference [129] that covalent materials transform into the higher coordination structures as pressure increases. We find that the B4→B_k transition is characterized by a decrease in coordination number from four to three. However, the B_k phase is stable only within a short pressure range 24.65 - 32.85 GPa.

The results also predict a transition from B_k to B2 phase through the intermediate B_i phase, following the sequence B_k →B_i →B2 with pressures of about 16.56 GPa

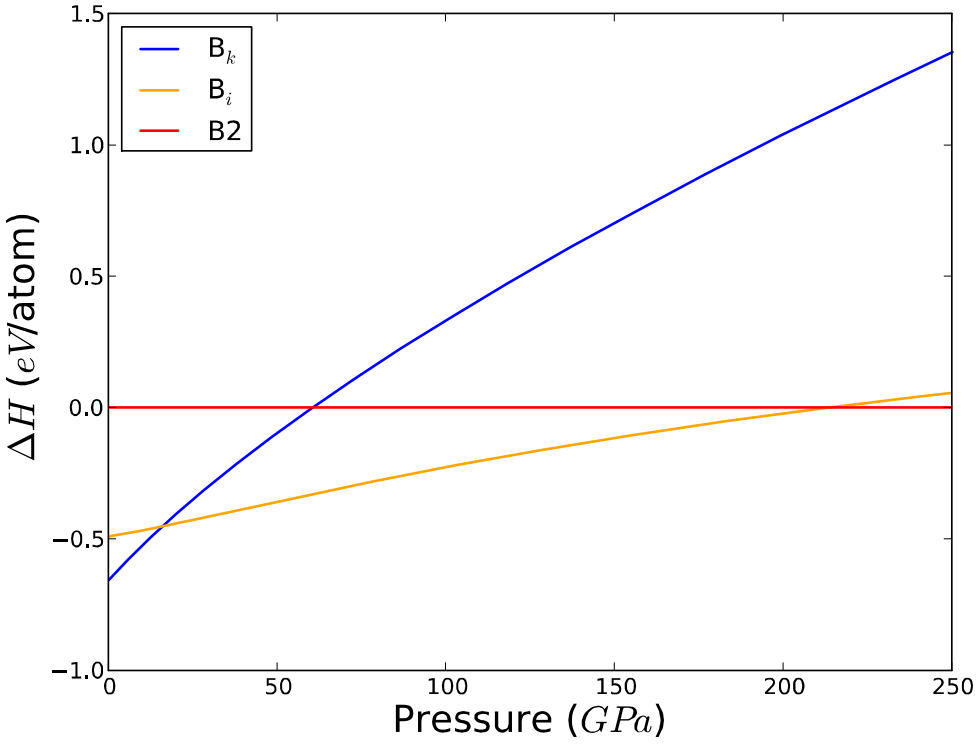

Figure 6.6: The GGA enthalpy differences of B_k, B_i and B2 phases of ZnO as a function of pressure showing the B_k →B_i →B2 phase transition. The high pressure B2 phase has been taken as a reference.

and 213.30 GPa respectively, within GGA or 12.25 GPa and 248.0 GPa respectively within LDA. The phase diagram is shown on Fig. 6.6 for the GGA.

Furthermore, application of pressure on the B4 phase induces a transition to B2 phase, with the six-fold coordinated $B8_1$ as the intermediate phase according to the order B4→$B8_1$ →B2. This is shown on Fig. 6.7 for the GGA. It requires a pressure of about 183.25 GPa for a $B8_1$ →B2 transition, while about 19.52 GPa is required for the preceding B4→$B8_1$ transition, according to the GGA.

Lastly, we predict that the B4 phase undergoes a direct transition to the nine-fold coordinated B32 phase at about 229.1 GPa within LDA or 219.1 GPa within GGA.

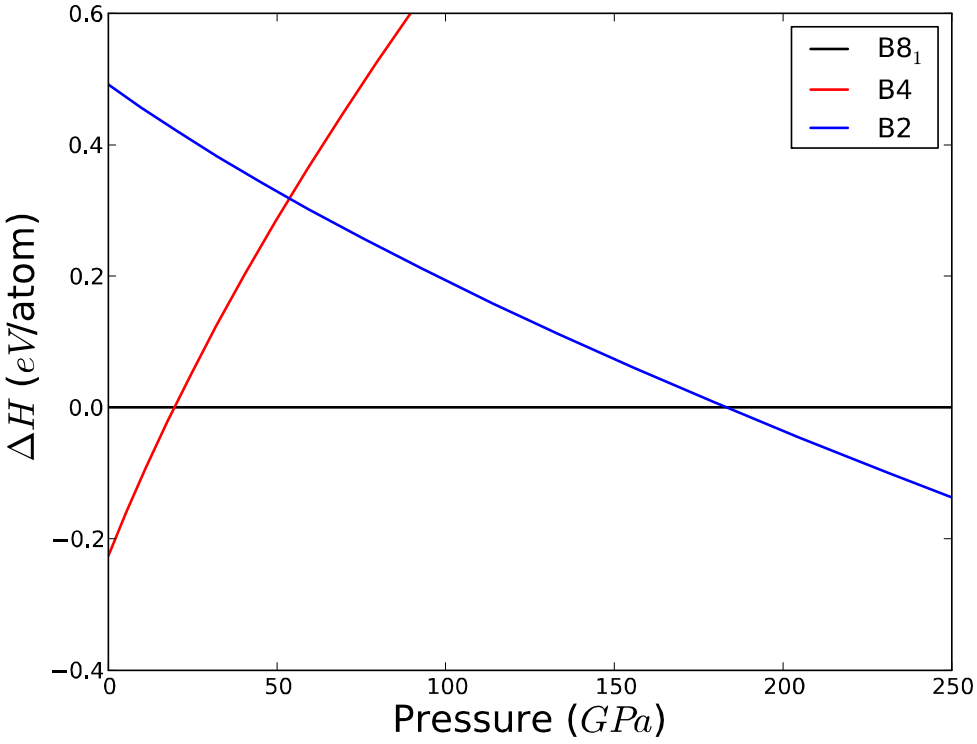

Figure 6.7: The GGA enthalpy differences of B4, B8$_1$ and B2 phases of ZnO as a function of pressure showing the B4→B8$_1$ →B2 phase transition. The intermediate B8$_1$ phase has been taken as a reference.

These results shows that the B2 structure is the most preferred candidate for high pressure phases in ZnO among all the structures considered in this study. As already mentioned, the predicted B2 phase has, however, never been observed experimentally so far due to the difficulties in achieving pressures in the vicinity of 250 GPa.

When comparing the LDA and GGA, we find, as in reference [3] that the GGA corrects the tendency of the LDA to underestimate transition pressures between low-pressure phases. This behaviour is seen in particular for the phase transitions below 35 GPa, with the exception of B4→B_k transition. For high-pressure phases however, the GGA tends to predict smaller values relative to the LDA. This inconsistency is not suprising, since the charge density is less uniform at high pressure and therefore the GGA and LDA are both likely to be less accurate. To our knowledge, other than the widely reported B4→B1→B2 and the recently predicted B1→B10→B2 phase transitions, there is neither experimental nor theoretical data for the other phase transitions in ZnO, and the results presented here can be considered as predictions. To gain insight into the microscopic mechanism underlying the stability of these phases, we look at their electronic structure in the next chapter. Since standard DFT, in principle, cannot describe electronic excitations, it is important to use the GW approximation, which gives a more realistic description of the band gap.

Chapter 7

Electronic Structure of ZnO

Knowledge of the electronic structure and properties of a material is crucial to the understanding of the stability of the different structures at different volumes. Theoretical results in the literature show that understanding of the electronic structure of ZnO turns out to be one of the most challenging tasks. The electronic structure of ZnO in the wurtzite (B4), zinc blende (B3), high pressure rocksalt (B1) and CsCl (B2) structures has been widely studied [7, 120, 125, 130, 131] in the framework of DFT, using the LDA and semilocal GGA. Although the structural properties were accurately predicted, these calculations gave poor account of the optical properties. In particular, the electronic band gap is severely underestimated. For instance, the band gap is predicted to be 0.81 eV in the B4 and 1.10 eV in the B1 phases [130]. The experimental values of the band gap for B4 (3.44 eV) [132] and B1 (2.45 eV) [133] phases are quite large in comparison with this theoretical results.

This is not surprising since DFT is a ground state theory and, in principle, cannot describe electronic excitations. By examining the electronic structure using the Kohn-Sham DFT approach, the excitation aspect is neglected, and hence the resulting energy gaps and interband transition energies are underestimated [103]. Al-

though the fundamental gap is a ground state property, it cannot be described in Kohn-Sham DFT due to the discontinuity in the functional derivative of the exact exchange-correlation functional at integer particle numbers. The value of the derivative discontinuity of the exact functional is not known, which makes it impossible to determine the fundamental gap from the Kohn-Sham energies [8, 95].

As an alternative to conventional (semi) local DFT exchange-correlation functionals, the Heyd-Scuseria-Ernzerhof (HSE) screened hybrid density functional has been proven to yield results in good agreement with experiment for a wide range of solids [47, 57, 62–66]. However, the GW approximation offers a strong physical basis for correlating the band energies obtained using the single-particle Green's function with experimental band gaps. Thus, we present in this chapter the electronic structure of ZnO calculated by the HSE functional and the quasiparticle GW approach and compare with experimental data where available.

7.1 Technical Details

Calculations were performed using the plane-wave projector augmented wave (PAW) method and the HSE06 screened hybrid functional, with the screening parameter fixed at a value of 0.2 $Å^{-1}$ as implemented in the VASP code. The total and projected density of states were obtained using the tetrahedron method and a plane-wave cutoff of 400 eV. The sampling of the Brillouin zone was performed using a Monkhorst-Pack scheme. The applied **k**-point meshes were 8 x 8 x 6 and 9 x 9 x 9 for the hexagonal and cubic structures respectively. Unlike standard DFT calculations which require a very accurate sampling, HSE06 calculations converge rapidly with the number of **k**-points. The band structures were computed on discrete **k**-meshes following high-symmetry directions in the Brillouin zone.

Quasiparticle corrections to the band gap were computed using the GW approximation as implemented in the VASP code [108]. The Kohn-Sham DFT electronic structure calculated with the standard GGA PAW potentials serves as a starting point for the excited state calculations. The standard DFT pseudopotential for Zn atom treats the $3d^{10}$, $4s^2$ as the valence electrons. It has been reported that considering the Zn $3d$ electrons as part of the valence shell (Zn^{+12}) is a necessary step towards a quantitative description of the structure and electronic properties of zinc compounds [134]. In a more recent study of the GW band structure of ZnO by Dixit *et al.* [135] the Zn $3s$, $3p$ states were included as valence electrons, resulting in a more accurate but hard 20-electron pseudopotential for zinc (Zn^{+20}). However, including the $3s$ and $3p$ states in the valence shell is beyond our computing capability. This would require very high plane-wave cutoff and the calculation would become too time consuming within the framework of plane-wave basis expansion. For this reason, we stick to the standard Zn^{+12} PAW potential used in the ground-state DFT calculations.

We have found that about 300 bands and an energy cutoff of 150 eV for the response function are sufficient to converge the GW band gap to within 10^{-2} eV. The calculations reported here were based on the partially self-consistent GW_0 approximation, using DFT PBE eigenvalues and orbitals as inputs [109, 110]. The quasiparticle energies were obtained by iterating G at least 4 times in the self-consistency cycle while keeping W fixed at its initial DFT W_0 value [109, 110, 114] as discussed in sections 5.2 and 5.4. The GW procedure is computationally more demanding than calculations using the local or semilocal exchange-correlation functionals, thus the k-point meshes for the Brillouin zone integrations were restricted to 9 x 9 x 6 for the hexagonal structures and 10 x 10 x 10 for the cubic structures. These result in 47 and 56 k-points in the irreducible part of the Brillouin zone respectively. The final quasi-

particle energies are converged to about 10-20 meV. For the purpose of comparison, we obtain the quasiparticle bandstructure by interpolating the quasiparticle energies through similar k-point paths used for the DFT bands.

7.2 Equilibrium Band Structure and Density of States

In order to understand the behavior of the electronic structure of ZnO under phase transition pressures, we start by looking at the band structure and density of states (DOS) for the experimentally observed phases, i.e. the wurtzite (B4), zinc blende (B3) and rocksalt (B1) phases calculated at equilibrium lattice parameters given on Table 6.1. The resulting energy band-gaps are shown on Table 7.1, together with the binding energies of the d bands.

In the wurtzite phase, the calculated band structure (Fig. 7.1) indicates that ZnO is an insulator or wide-gap semiconductor with a direct fundamental band-gap at the Γ point in the Brillouin zone. As seen on Table 7.1 we obtain from Fig 7.1 (a), an energy band-gap of 2.42 eV for wurtzite ZnO using the screened hybrid HSE functional, in good agreement with the corresponding HSE gap value of 2.46 eV reported in Ref. [66]. This is clearly a significant improvement over conventional DFT calculations, although the value is underestimated compared to 3.44 eV obtained from experiment [132].

Partially self consistent quasiparticle corrections based on GGA eigenvalues improves the band gap of the B4 structure to 2.60 eV, which is an underestimation

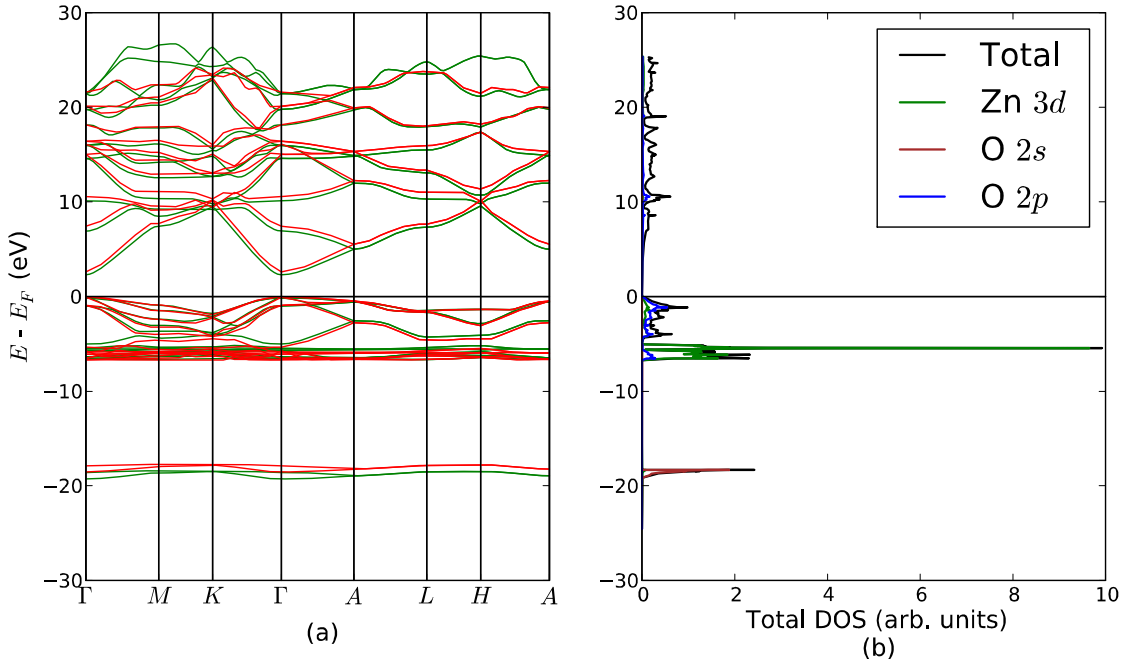

Figure 7.1: (a) The HSE (green lines) and the interpolated GW_0 (red lines) band structure for wurtzite (B4) ZnO at zero pressure. The valence band maximum is placed at 0 eV. (b). The total and projected DOS calculated using the HSE functional.

Table 7.1: The fundamental energy band gaps E_{gap} and the Zn 3d-band binding energies E_{3d} for the B4, B3, and B1 structures calculated within hybrid HSE functional and GW_0 approximation at equilibrium volume. All energies are expressed in eV. Comparison is made with experimental as well as previously reported theoretical data where available.

	This work		Other calculations		Expt.[c]
	HSE	GW_0	HSE[a]	GGA+GW_0 [b]	
B4 (wurtzite)					
E_{gap} $(\Gamma - \Gamma)$	2.42	2.60	2.46		3.44
E_{3d}	5.91	6.89	6.0		(7.5-8.81)
B3 (zinc blende)					
E_{gap} $(\Gamma - \Gamma)$	2.28	2.39		2.54	3.27
E_{3d}	5.88	6.23		6.6	
B1 (rocksalt)					
E_{gap} $(\Gamma - L)$	2.44	2.51			2.45±0.15
E_{3d}	4.53	5.01			

[a]Ref. [66]
[b]Ref. [114]
[c]Refs. [132, 133, 136–139]

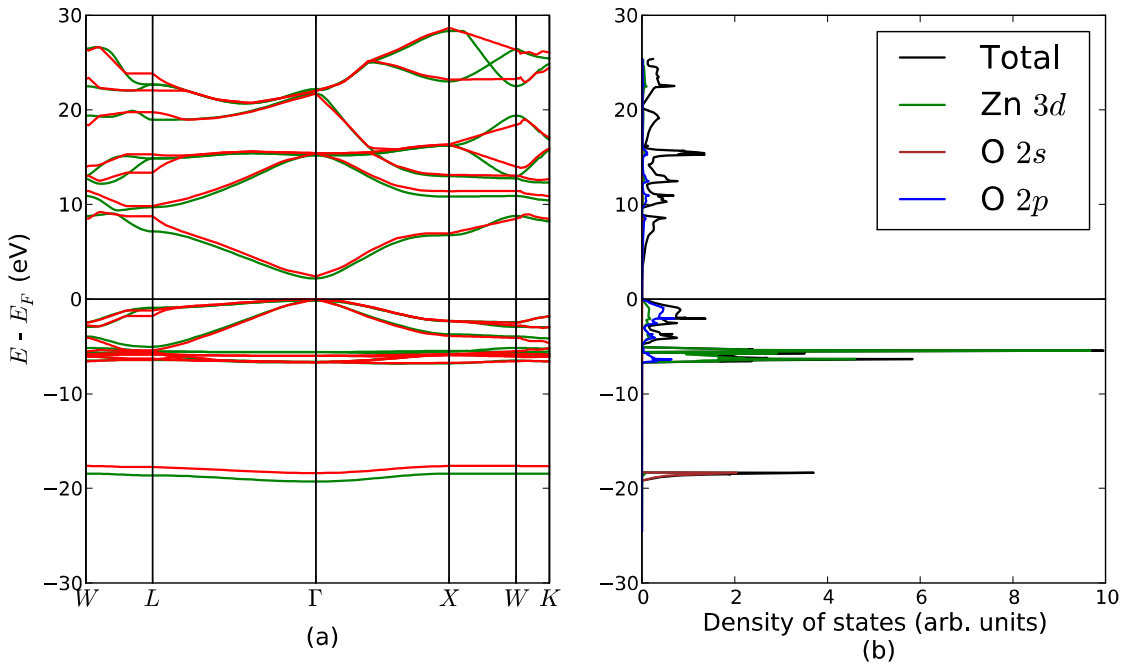

Figure 7.2: (a) The HSE (green lines) and the interpolated GW_0 (red lines) band structure for the zinc blende (B3) ZnO at zero pressure. The valence band maximum is placed at 0 eV. (b) The total and projected DOS calculated using the HSE functional.

of about 25% relative to experiment. A non-self consistent GW band-gap of 2.46 eV [140] has been reported for this structure, whereas an all electron-GW calculation gives a result of 2.44 eV [141]. Recently, Dixit *et al.* [142] reported a LDA+G_0W_0 band gap of 2.49 eV, obtained with a Zn^{+20} pseudopotential, suggesting that the Zn^{+12} pseudopotential gives an insufficient quasiparticle correction due to the inadequate treatment of the exchange interaction in the self-energy.

In a recent Letter, Shih *et al.* [143] reported a band gap for wurtzite ZnO, calculated with the single-shot non-self-consistent G_0W_0 approach based on LDA and LDA+U solutions, that deviated strongly from previous studies and surprisingly agreed well with experiment. They performed calculations with up to 3000 empty bands as well as a dielectric matrix cutoff of up to 80 Ry ($\approx$ 1100 eV), which resulted

in the band gaps of 3.4 eV by LDA+G_0W_0 and 3.6 eV by LDA+U+G_0W_0 approaches. The larger band gap in the latter approach was attributed to the significantly reduced hybridization of the Zn $3d$ states and O $2p$ states by inclusion of the orbital-dependent potential U. It was also demonstrated that the use of too small dielectric cutoff can lead to a false convergence behavior: the band gap converges toward a small value when fewer bands are used. These results therefore suggest that the underestimated values of the wurtzite ZnO GW band gaps obtained herein, and in other all-electron studies [114, 115, 141, 144] (2.12 - 2.60 eV) are largely due to inclusion of fewer bands (200 - 300) and much lower cutoff for the response function.

In response to Shih *et al.*'s letter, Friedrich *et al.* [145] confirmed the result that the GW band gap of ZnO shows a very slow convergence with respect to the number of states used to construct the polarization function and the correlation self-energy. Moreover, it was shown that even with 3000 bands, the band gap is not well converged - hence a hyperbolic fit was used to extrapolate to infinite bands, thus eliminating the linearization error for high-lying states with local orbitals. This produced a band gap of 2.99 eV for wurtzite ZnO, somewhat smaller than the result of reference [143], but considerably larger than those of previous studies [114, 115, 141, 144] and 2.60 eV obtained in this thesis. Both studies therefore suggest a need to thoroughly examine the band convergence in the present and other previously reported GW calculations, with ZnO being the extreme case study.

For the zinc blende structure, we obtain from Fig. 7.2 (a), a direct band gap value of 2.28 eV at the Γ point using the HSE functional. The GW_0 approach yields a slightly improved value of 2.39 eV. This agrees fairly with the corresponding partially self-consistent GW_0 band gap of 2.54 eV reported by Shishkin and Kresse [114]. The difference may be attributed to an estimated convergence error of 0.1 eV the authors

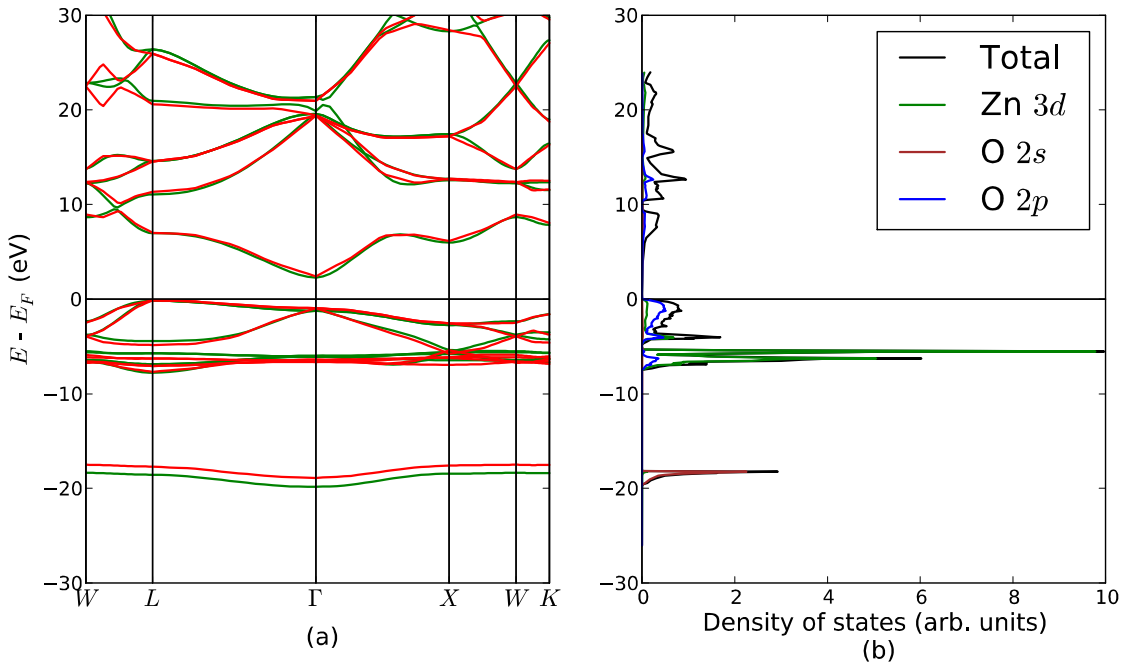

Figure 7.3: (a) The HSE (green lines) and the interpolated GW_0 (red lines) band structure for the rocksalt (B1) ZnO at zero pressure. The valence band maximum is placed at 0 eV. (b) The total and projected DOS calculated using the HSE functional.

used in their work, to correct the eigenvalues for ZnO. However, this value is still not satisfactory as compared to an experimentally estimated value of 3.27 eV [136, 146].

The nature of the fundamental band gap changes from direct to indirect going from the zinc blende (Fig. 7.2) to rocksalt (Fig. 7.3) with the conduction band minimum (CBM) at Γ and the valence band maximum (VBM) at L points in the Brillouin zone. It has been argued [135, 147] that this change can be understood on the basis of the symmetry dependence of the interaction between anion p states and cation d states. The tetrahedrally coordinated B3 phase possess no inversion symmetry center, thus the anion p states and cation d states can mix at any point in the Brillouin zone. On the contrary, the rocksalt phase possess an inversion center at the Γ point so the p and d states do not mix. For the rocksalt phase, we obtain

respectively, an indirect band gap of 2.44 eV and 2.51 eV by the HSE functional and GW_0 method. This value can be compared and is in good agreement with a reported indirect band gap of 2.45 ± 0.15 eV [133] for the rocksalt structure measured from optical absorption.

However, when comparing the calculated gaps with experimental results, it is important to consider the difference of the meaning between the quasiparticle and optical band-gaps. In optically measured gaps, there is a possibility of excitons with binding energies smaller than the single-particle gaps measured in photo-emission experiments [148]. A two-particle Green's function that describes the interaction between particles and holes is required to take account of excitonic effects. The GW_0 calculations reported here are based on single-particle Green's function, which does not provide information on the exciton energies. Strictly speaking, our calculated band gaps should therefore be compared with the photoemission gaps [149].

There are similarities in the atomic origin of the bands for the different polymorphs of ZnO as shown by the HSE projected DOS plots in Figs. 7.1(b) - 7.3(b), despite the different lattice parameters and coordination. The O $2s$ states give rise to weakly dispersive bands that correspond to a peak in the DOS at about $18 - 19$ eV below the VBM. The uppermost valence bands are predominantly characterized by O $2p$ states found in the energy interval from 0 to -4 eV, corresponding to lower peaks in the DOS. For the cubic zinc blende (Fig. 7.2) and rocksalt (Fig. 7.3) structures, the O $2p$ derived bands are three-fold degenerate at the Brillouin zone centre (Γ point), irrespective of the different nature of the fundamental energy gap in these structures. The Zn $3d$ states are located within the energy interval of 5 to 7 eV below the VBM and separated by a huge gap ($11 - 12$ eV) from the O $2s$ states. These give rise to relatively weak dispersion of the energy bands in the wurtzite structure

corresponding to quite high peaks in the DOS as compared to the zinc blende and rocksalt structures.

A further important aspect of electronic structure of ZnO is the binding energy E_{3d} of the semicore $3d$ bands. The binding energies shown on table 7.1, have been obtained from the main peaks of the d-projected density of states without shifting the valence band maximum to zero. For the wurtzite structure, the HSE functional binds the $3d$ bands at 5.91 eV, which is a significant improvement compared to the PBE GGA value of 4.8 eV reported in Ref. [66]. This agrees well with the corresponding HSE value of 6.0 eV found from the aforementioned reference. As expected, the GW_0 approach yields stronger bound d-electrons with a binding energy (6.89 eV) much closer to experiment. We have no experimental data to compare with for the other structures.

From table 7.1, it can be concluded that the HSE hybrid density functional yields improved band gaps for ZnO as compared to the DFT GGA functionals. This improvement is attributed to a better description of the Zn $3d$ states which are more localized and energetically deeper resulting in less hybridization with the O $2p$ states. However, an underestimation (up to 30%) of the band gap with respect to experiment still prevails, pointing towards the need to include more non-local Fock-exchange than the $\frac{1}{4}$ used in the HSE functional. Recently, it has been observed [150] that increasing the fraction of non-local exchange from the original value of $a = 0.25$ justified by pertubation theory, to $a = 0.375$ within HSE increases the energy gap of wurtzite ZnO to 3.43 eV, in excellent agreement with experiment. However, this approach is not well justified; the choice of the fraction a (other than 0.25) is not transferable and it has to be optimized for every material under study, just for the purpose of reproducing the experimental band gap. A recent study on electronic properties of

various oxides by Park *et al.* [151] shows that the optimized values lie between 0.2 and 0.4 depending on the material.

Going beyond DFT, application of GW_0 on top of GGA wavefunctions further improves the energy gaps, underestimating experiments by up to 25%. It has been demonstrated that this underestimation of band gaps in shallow d materials (including GaAs and GaN) is due to an inaccurate description of the static dielectric properties which turns out to be a result of the incomplete cancellation of the Hartree self-energy within the d shell by the GGA functional [37,114]. We believe that choosing the HSE hybrid exchange-correlation functional as a starting point for GW_0 calculations could yield excellent agreement with experiment, however we rely on GGA+GW_0 approach as a reasonably faster method for predicting band gaps. In the next section we look at the effects of applied pressure on the electronic properties for different structural phases of ZnO.

Although the dispersion of the interpolated GW_0 bands is less smoother than the DFT counterpart, the effect of quasiparticle corrections is evident on the band structure plots of Figs. 7.1 - 7.3. The general result, relative to DFT bands is that the conduction bands are pushed further up towards higher energies, while the upper valence bands are shifted down towards lower energies with respect to the valence band maximum. As a result, the band gaps are opened in comparison to the hybrid DFT case. Surprisingly, the band structures revealed by our GW_0 calculations indicate that the O $2s$ bands are higher in energy than in the hybrid HSE case. This is an anomaly, since all occupied bands are expected to be shifted down towards lower energies (i.e., possess negative quasiparticle shifts) in GW approach as in the case of InN [152]. This O $2s$ band anomaly may be one of contributing factors to the underestimated $3d$ binding energies and band gaps in our GW_0 results.

7.3 Pressure Dependent Electronic Structure

In this section we examine the influence of external pressure on the electronic properties of the different structures at the phase transitions reported in chapter 6. In particular, we look at the electronic structure of wurtzite (B4), rocksalt (B1), and the hypothetical CsCl (B2) structures under respective phase transitions pressures P_T(B4 $\rightarrow$B1) (11.5 GPa) and P_T(B1 $\rightarrow$B2) (253 GPa). Table 7.3 shows the calculated energy band gaps, Zn$-$O bond lengths and Bader charge transfer for these phases under different pressures. The electronic band structure and density of states for the intermediate phases are presented in appendix A.

7.3.1 Energy band gap

A comparison of the band structure for wurtzite ZnO in Fig. 7.4(a) shows that when this structure is compressed from 0 to a transition pressure of 11.5 GPa, the valence bands tend to shift to lower energies while the conduction bands shifts to higher energies. This band shift increases the calculated fundamental energy band gap from 2.60 eV at equilibrium to 2.82 eV at the transition pressure. The energy band gaps for the structures in the B4 $\rightarrow$B1 $\rightarrow$B2 phase sequence are summarized on table 7.2. From the band structure of rocksalt ZnO under 11.5 and 253 GPa shown in Fig. 7.4(b), the band shift is more clear as the pressure change is larger. The compression of the rocksalt phase broadens the band gap E_{gap} $(\Gamma - L)$ further from 2.94 eV at 11.5 GPa, to 6.68 eV at 253 GPa, where a transition to the cesium chloride (B2) structure is expected. The fact that the GW_0 approach offers larger band gaps relative to the HSE functional is evident in table 7.2.

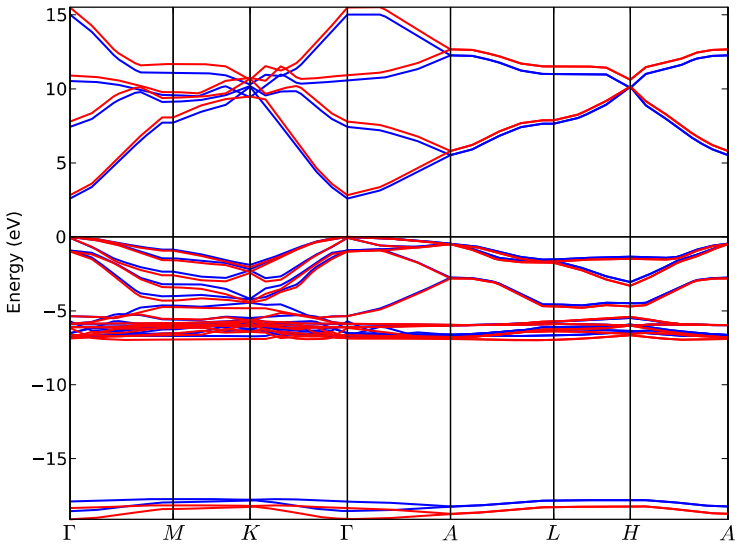

(a) wurtzite

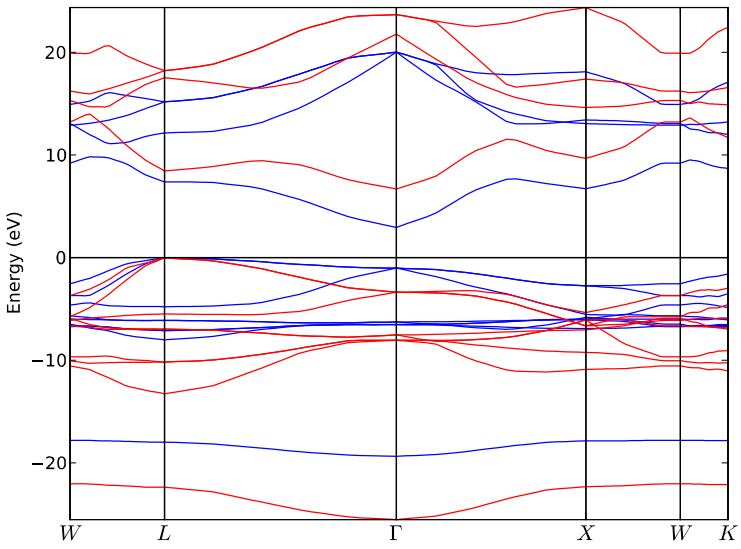

(b) rocksalt

Figure 7.4: The Interpolated GW_0 band structure: (a) Wurtzite (B4) ZnO under zero pressure (blue lines) and phase transition pressure (red lines) of 11.5 GPa (b) Rocksalt (B1) ZnO under phase transition pressure of 11.5 GPa (blue lines) and 253 GPa (red lines).

Table 7.2: The fundamental energy band gaps E_{gap} for the wurtzite (B4), rocksalt (B1), and cesium chloride (B2) structures of ZnO under respective structural phase transition pressures, obtained by the HSE hybrid functional and GW_0 approach.

Phase transition	Structure	Pressure (GPa)	Band gap E_{gap} (eV)	
			HSE	GW_0
B4 →B1	B4	11.5	2.57	2.82
	B1	11.5	2.79	2.94
B1 →B2	B1	253	6.00	6.68
	B2	253	4.28	5.36

The band structure of the hypothetical B2 structure, which has been predicted to be the most favorable high pressure candidate is shown in Fig. 7.5 under pressure of 253 GPa. In comparison with HSE bands (green lines), the interpolated GW_0 bands (red lines) are fairly accurate at least along the $\Gamma - X - M$ path in the Brillouin zone. The B2 structure is shown to be an indirect band gap semiconductor with the conduction band minimum at Γ and valence band maximum at X points in the Brillouin zone. The fundamental band gap is found to be 4.28 and 5.36 eV by the HSE functional and GW_0 approach respectively.

7.3.2 Zn−O bond length

It can be seen from table 7.3 that the Zn−O bond length in these structures is reduced with increasing pressure as expected. For instance, the bond length is significantly reduced from 2.13 to 1.84 Å when the rocksalt structure is compressed from 11.5 to 253 GPa. The neighboring atoms are indeed expected to approach each other when the solid is compressed, as confirmed by the decreasing bond lengths for the wurtzite and rocksalt structures shown in table 7.3. According to the Mott criterion, a material under pressure should tend towards a metalic state as the atoms approach each other.

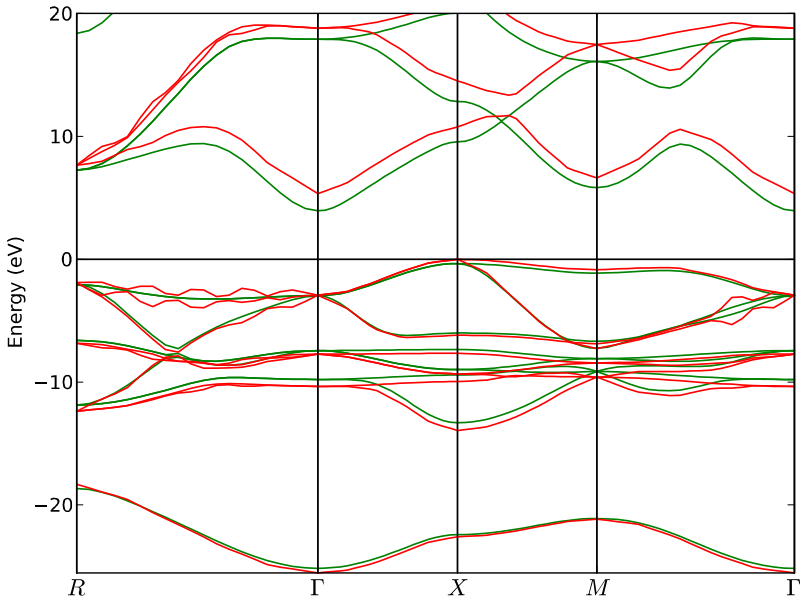

Figure 7.5: The HSE (green lines) and interpolated GW_0 (red lines) band structure for cesium chloride (B2) ZnO under transition (B1→B2) pressure of 253 GPa. The valence band maximum is placed at 0 eV.

Table 7.3: The fundamental energy band gaps E_{gap}, Bond lengths and Bader charge transfer for the wurtzite (B4), rocksalt (B1), and cesium chloride (B2) phases of ZnO under respective structural phase transition pressures. The band gaps obtained by HSE functional are also presented for comparison.

Structure	Pressure (GPa)	Band gap E_{gap} (eV)		Bond length (Å)	Charge transfer δq
		HSE	GW_0		
wurtzite (B4)	0	2.42	2.60	1.99	1.26
	11.5	2.57	2.82	1.95	1.28
rocksalt (B1)	0	2.44	2.51	2.17	1.34
	11.5	2.79	2.94	2.13	1.35
	253	6.00	6.68	1.84	1.37
cesium chloride (B2)	253	4.28	5.36	1.97	1.36

This criterion, describing the critical point of the metal-insulator transition, is $n^{\frac{-1}{3}} < Ca_0^*$, where n is the electron density of the material, C a constant and a_0^* is the effective Bohr radius [153]. In other words, for a sufficiently high electron density, the material should become a metal or otherwise it becomes at insulator. In this work, it found that the Mott criterion is not satisfied for the pressure range considered and hence the band gap increases with increasing pressure. Under high pressure conditions, the wave functions overlap more strongly, producing increased dispersion of the electronic bands in k space as well as increased bandwidths along the energy axis. As a result, the energy band gap is broadened at high pressures. This is more evident on Fig. 7.4(b). However, the nearest neighbor bonds lengthen when there is a phase transition to a structure of increased atomic coordination even though the density is increased. For instance, the phase transition from the four-fold coordinated B4 structure to the six-fold coordinated B1 structure at 11.5 GPa is characterized by an increasing bond length from 1.95 to 2.17 Å.

7.3.3 Charge analysis

In order to obtain insights into the electronic charge density reorganization upon phase transitions, we calculated the charge transfer for the structures at different pressures as shown on table 7.3. Charge transfer from cations to anions is a measure of the ionicity of the crystal. We calculated the amount of charge on constituent Zn and O atoms in the crystals by performing Bader charge analysis as described in section 4.8. The Bader charge transfer δq from Zn to O was then obtained by subtracting the valence charges for free Zn and O atoms from the calculated charge values on the same atoms in Bader volumes.

As expected, it is found that for all structures considered, a significant amount of

charge is transferred from Zn to O atoms due to the difference in electronegativity. The amount of charge transfer tend to increase when the structures are compressed, implying that the Zn−O bonds acquires a more ionic character. However, it is worth noting that quite large changes in pressure lead to very slight changes in the Bader charge transfer. This is clearly seen in the rocksalt where a large compression from 0 to 253 GPa yields a difference of only 0.02 in δq. This suggests the need and importance of well converged calculations in order to study such slight differences. A charge transfer $\delta q = 1.36$ is obtained for the high pressure B2 structure, which is only 0.01 less than that obtained for the B1 structure at the same pressure. Thus, this indicates that upon the B1 →B2 transition the local environments in the B2 structure preserve important electron density features present in the parent (B1) structure.

7.3.4 GW_0 density of states

The projected density of states (PDOS) have also been calculated at the GW_0 level of approximation for the different structures at the their respective transition pressure. Shown in Fig. 7.6 are the PDOS for the wurtzite (B4) and rocksalt (B1) phases corresponding to the GW_0 bandstructures of Fig. 7.4. Figure 7.6(a) and (b) show that when the B4 structure is compressed from 0 to a transition pressure of 11.5 GPa, the Zn $3d$-derived peaks are greatly reduced in height, appears to be split while shifting slightly down to lower energies. The O $2s$-derived peak at the lower valence band is also slightly reduced and shifted down in energy. This small change in PDOS features over 0 to 11.5 GPa is consistent with the small changes observed in the band structure of the wurtzite presented in figure 7.4(a).

When the B1 structure is compressed through the wide pressure range from 11.5 GPa (Fig. 7.6(c)) to 253 GPa (Fig. 7.6(d)), the O $2s$ states broadens and shifts down

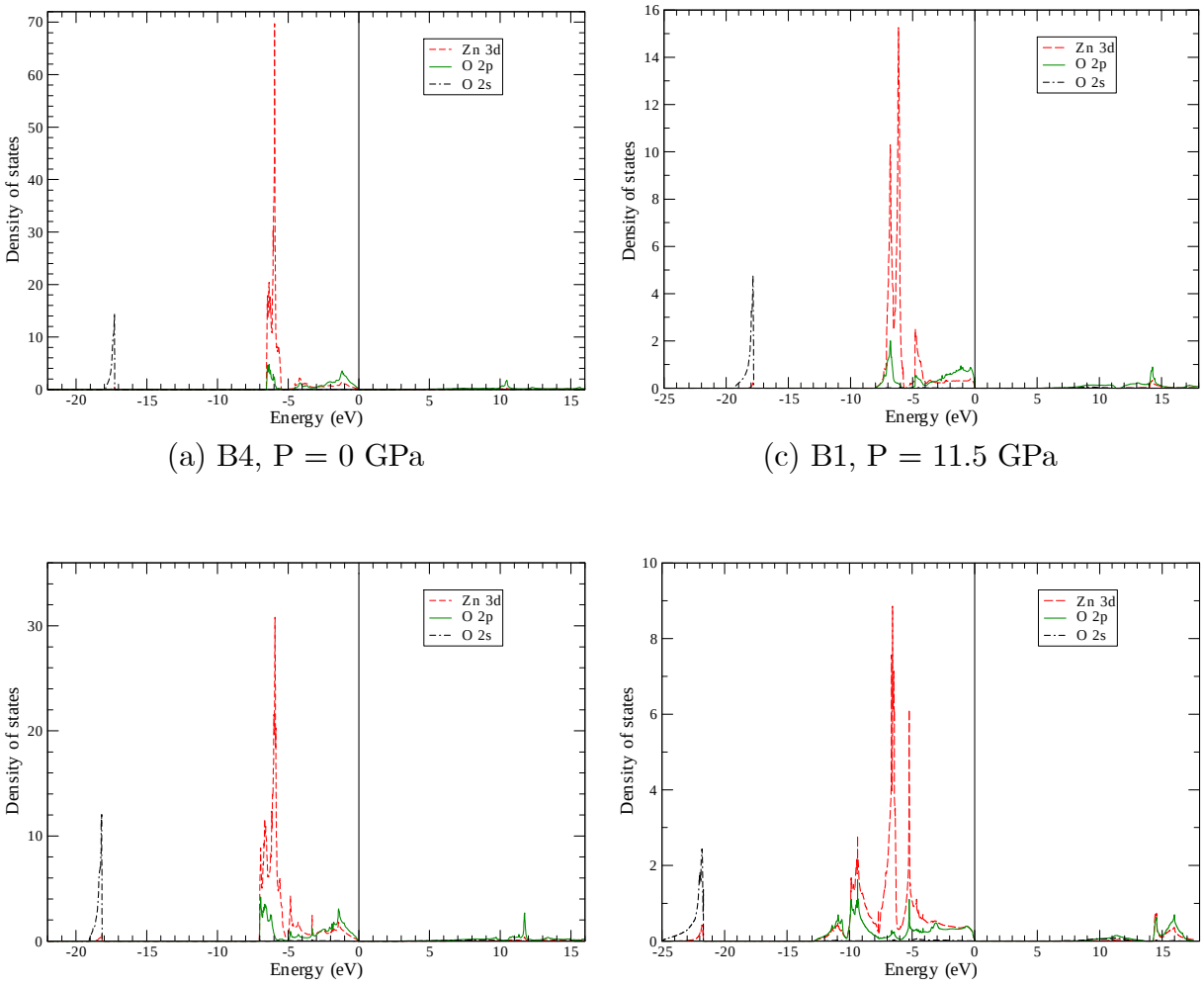

(a) B4, P = 0 GPa

(c) B1, P = 11.5 GPa

(b) B4, P = 11.5 GPa

(d) B1, P = 253 GPa

Figure 7.6: GW_0 projected density DOS for ZnO in the B4 structure at (a) pressure P = 0 GPa, (b) P = 11.5 GPa and the B1 structure at (c) P= 11.5 GPa, (d) P = 253 GPa following the B4→B1→B2 phase sequence. The vertical solid line at 0 eV indicates the valence band maximum.

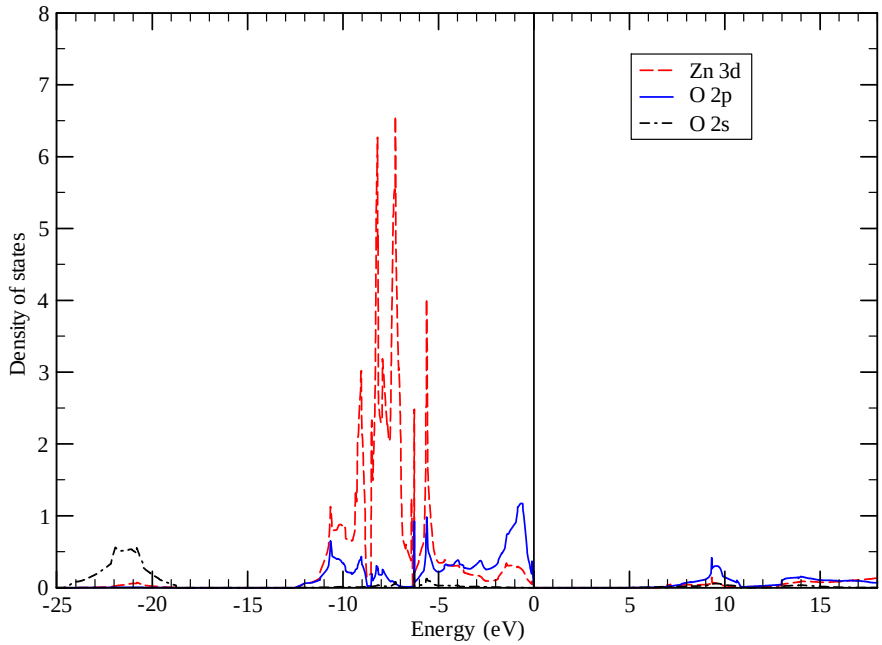

Figure 7.7: GW_0 total and projected density DOS for ZnO in the B2 structure under phase transition (B1→B2) pressure of P = 253 GPa. The vertical solid line at 0 eV indicates the valence band maximum.

in energy. The peaks in the upper valence band also split and broaden greatly while shifting to lower energies. These show stronger hybridization of the O $2p$ and Zn $3d$ orbitals. The overall shift and broadening of the valence states agrees well with the shift in the valence bands observed in the corresponding band structure shown in Fig. 7.4(b).

The DOS changes abruptly upon transition to the high pressure B2 phase as shown in Fig. 7.7. In particular, the splitting of the $3d$ derived peaks shows a large increase and another peak of predominantly O $2p$ reappears near the top of the valence band. The O $2s$ derived peak is greatly reduced in height and broadens further, shifting up in energy and thus reducing the gap between the lower and upper valence bands. This reduction in height of the peaks implies low DOS for the most favorable high pressure B2 phase. Moreover, the Zn $3d$ and O $2p$ orbitals appears to be completely

hybridized and cannot be disentangled. These features have also been observed in DFT calculations available in the literature [3, 7, 131].

Chapter 8

Summary and Conclusion

This thesis has been concerned with the first-principles computational study of the structural properties and pressure induced phase transitions for different polymorphs of ZnO using plane-wave pseudopotential approach within density functional theory (DFT). In addition, the effect of pressure on electronic structure of ZnO has been investigated using hybrid DFT technique as well as the more relevant GW approximation. The main results of this study are an extensive set of data for the structural properties, pressure-induced phase transitions and the electronic properties of the various ZnO structures, which we consider to be a reference for future studies. The NaTl (B32), PbO (B10), WC (B_h), BN (B_k), NiAs ($B8_1$) and AsTi (B_i) crystal structures of ZnO have been considered in addition to the well documented wurtzite (B4), rocksalt (B1), zinc blende (B3) and CsCl (B2) structures.

We find a striking agreement between our calculated lattice parameters in the B4, B3, B1, and B2 structures and those found in the literature, using both the local density and generalized gradient approximations (LDA and GGA) of DFT. Our calculations confirm the LDA's tendency to underestimate the lattice parameters while GGA overestimates them. On the other hand, the LDA is seen to overestimate

the bulk moduli while GGA shows underestimation. These are well known features of these approximations which are present for all structures considered in this work.

We have demonstrated by means of structural phase diagrams that other possible structures of ZnO may exist as candidates for the most stable phase. However, both functionals confirm the hexagonal wurtzite (B4) structure as the most stable low-pressure phase, in agreement with previous experimental and theoretical studies. The cubic cesium-chloride (B2) structure remains the most favorable high-pressure phase in ZnO, although it is yet to be discovered experimentally.

For the structural phase transitions, the results confirm the well-documented phase sequence B4→B1→B2 for solid ZnO under high pressures in the vicinity of 10 and 260 GPa respectively. Apart from this, the present thesis revealed various transition paths from the four-fold coordinated B4 to the eight-fold coordinated B2 structure. In particular, there are phase sequences B4→B_k →B_h →B2 and B4→$B8_1$ →B2, with the B_k, B_h and $B8_1$ structures as intermediate phases. Moreover, it is suggested by the LDA that the B10 structure may be synthesized as an intermediate phase between the B1 and B2 structures, following the sequence B4→B1→B10→B2 at about 260 GPa, although there is no evidence for this transition in the GGA. It has been shown that the GGA corrects the tendency of the LDA to underestimate transition pressures for low-pressure phases, but both approximations are not consistent at higher pressures.

On the electronic structure, we have shown that HSE hybrid functional yields better results for the band gap of ZnO when compared to the standard DFT functionals. Although, the band gap is underestimated by 30% in the wurtzite structure, agreement with experiment is significantly improved. Application of the partially self-consistent GW_0 approximation on top of standard GGA wavefunctions offers a slight improvement in the prediction of band gap relative to the HSE hybrid func-

tional. We propose that applying the GW_0 approximation on top of the hybrid HSE wavefunctions could yield an excellent prediction of the energy gaps, despite the huge computational expense in doing so.

The general effect of increasing pressure on the band structure is the increasing energy gap at the structural phase transitions. The conduction bands shift towards higher energies while the valence bands shift down to lower energies and thus opening the fundamental gap between the valence band maximum and the conduction band minimum.

Using the Bader charge analysis method, it has been shown that a significant amount of charge is transferred from Zn to O atoms when the structures are compressed. This observation is consistent with the decreasing $Zn-O$ bond lengths with increasing pressure.

Appendix A

Band Structure and Density of States for the Intermediate Phases

The energy band structure and total density of states have been calculated within the GW_0 approximation for the intermediate phases B_k, B_h and $B8_1$. These are shown in the following pages. The band gaps for these structures, summarized on Table A.1, were obtained under their respective transition pressures, following the predicted transition paths B4→B_k →B_h →B2 and B4→$B8_1$ →B2. These are summarized in Table A.1. The total density of states for these structures resembles the projected density of states for the physically realized structures discussed in chapter 7, with the single peak at the lowest valence band originating from the O $2s$. The main peaks are predominantly of Zn $3d$ character while the uppermost valence band (0 to -5 eV) peaks resemble the O $2p$ states.

The band structure of the B_k phase shown in Fig. A.1 reveals that the B_k structure is an insulator with a direct gap at point Γ in the Brillouin zone. A band gap of 3.32 eV is obtained for this structure under transition pressure P_T(B4→B_k) of about 24.6 GPa. On transformation to the B_h phase (B_k →B_h) at about 32.8 GPa, the band

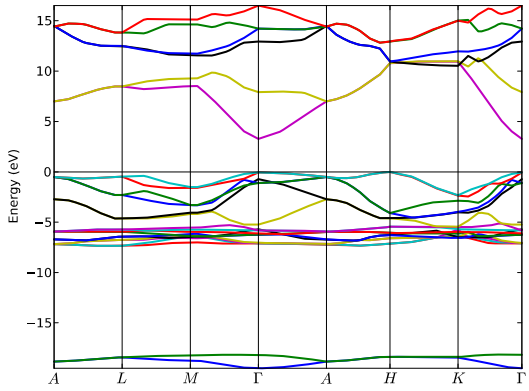

(a) P= 24.6 GPa

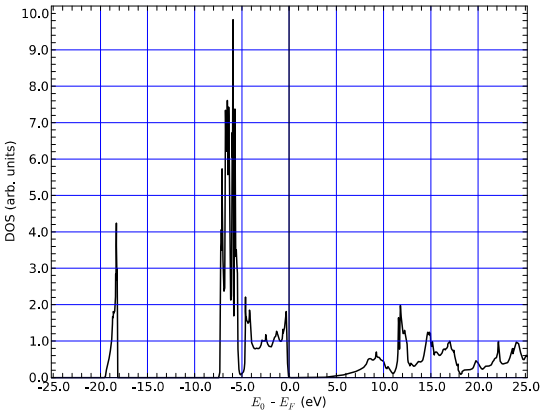

(b) P = 24.6 GPa

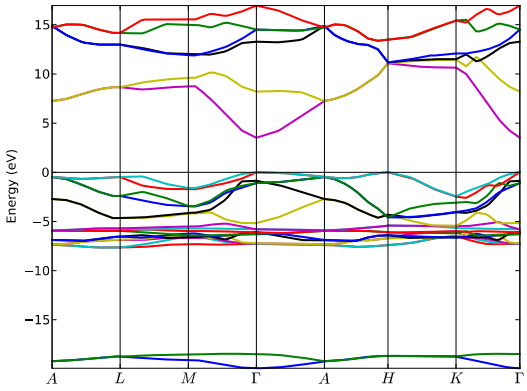

(c) P = 32.8 GPa

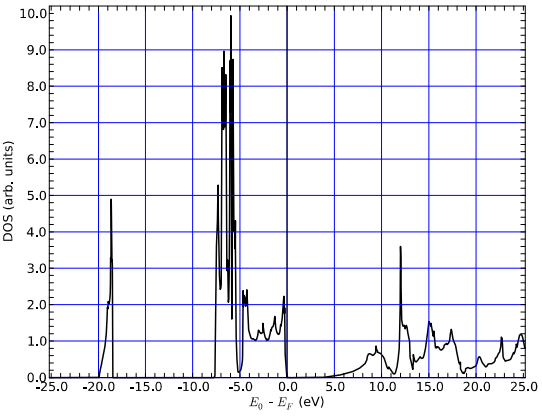

(d) P = 32.8 GPa

Figure A.1: The interpolated GW_0 band structure and total density of states for ZnO in the hexagonal B_k structure under transition pressure $P_T(\text{B4}\rightarrow B_k) = 24.6$ GPa and $P_T(B_k\rightarrow B_h) = 32.8$ GPa. The valence band maximum is placed at 0 eV in each case.

Table A.1: The fundamental energy band gaps E_{gap} for ZnO in the B_k, B_h and $B8_1$ structures under respective structural phase transition pressures, obtained by the GW_0 approximation.

Structure	Pressure (GPa)	E_{gap} (eV)
B_k	24.6	3.32
	32.8	3.49
B_h	32.8	2.34
	144.8	4.21
$B8_1$	19.5	3.15
	183.2	6.46

gap of the B_k slightly increases to 3.49 eV. There are no significant changes in the bands and density of states features over this short pressure range 24.6 GPa (left panel on Fig. A.1) to 32.8 GPa (right panel on Fig. A.1). The density of states peak at the lower valence band marginally shifts to down to lower energy and is enhanced in height.

Figure A.2 shows the band structure and density of states for the B_h structure, induced from the B_k structure at pressure around 32.8 GPa. The B_h is predicted to be an indirect gap semiconductor with the conduction band minimum at point Γ and the valence band maximum at point K in the Brillouin zone. A band gap of 2.34 eV is obtained for this structure at about 24.6 GPa as shown on Table A.1. On transformation to the high pressure B2 phase at 144.8 GPa, the band gap of the B_h structure is significantly increased to 4.21 eV. There is a radical change in the bands and density of states features over the wide pressure range from 32.8 GPa (left panel on Fig. A.2) to 144.8 GPa (right panel on Fig. A.2). In particular, the conduction bands shifts up to higher energies while the valence bands shifts to lower energies with increased dispersion. Hence the band gap is increased. The density of states peaks in the upper valence band broaden, are enhanced in height and shows increased splitting, suggesting a stronger hybridization of the Zn $3d$ and O $2p$ states.

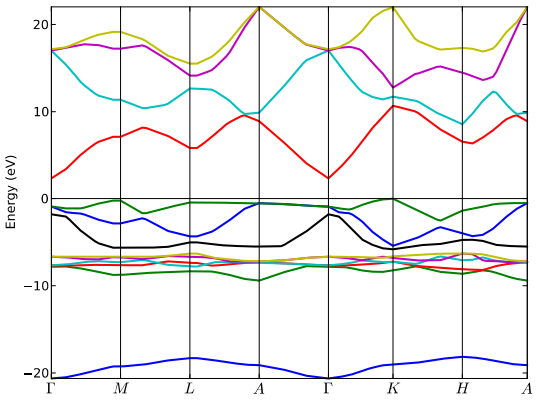

(a) P = 32.8 GPa

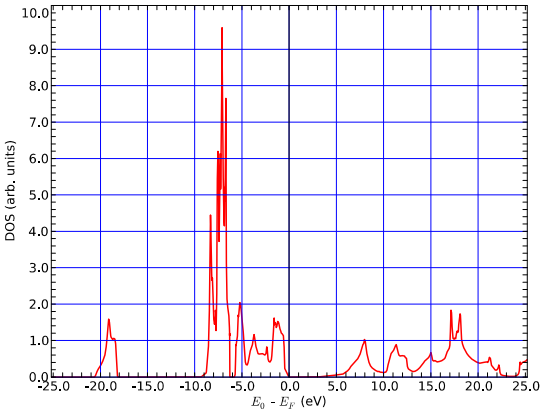

(b) P = 32.8 GPa

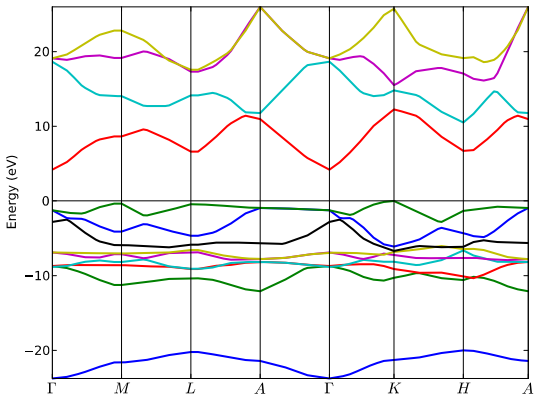

(c) P = 144.8 GPa

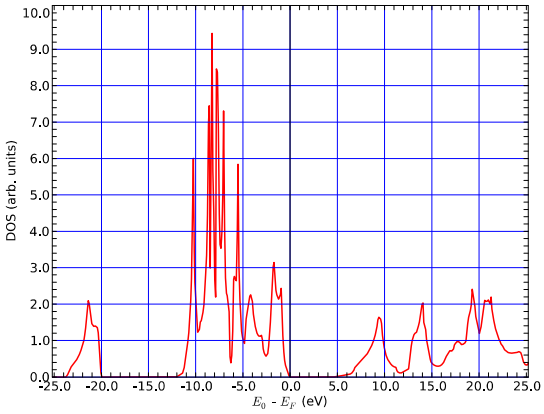

(d) P = 144.8 GPa

Figure A.2: The interpolated GW_0 band structure and total density of states for ZnO in the hexagonal B_h structure under transition pressure $P_T(B_k \rightarrow B_h) = 32.8$ GPa and $P_T(B_h \rightarrow B2) = 144.8$ GPa. The valence band maximum is placed at 0 eV in each case.

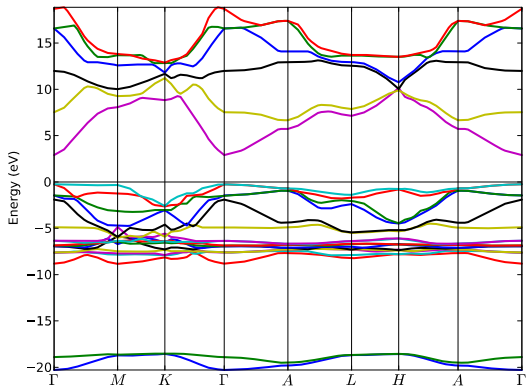

(a) P = 19.5 GPa

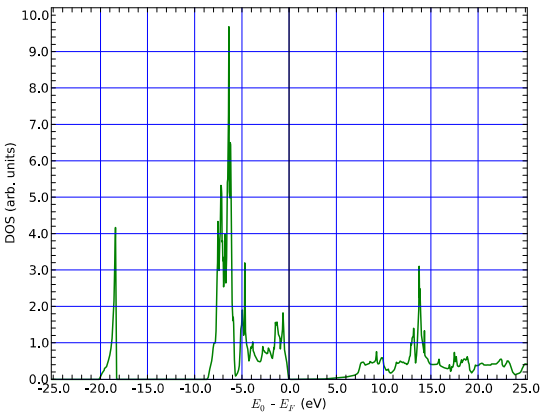

(b) P = 19.5 GPa

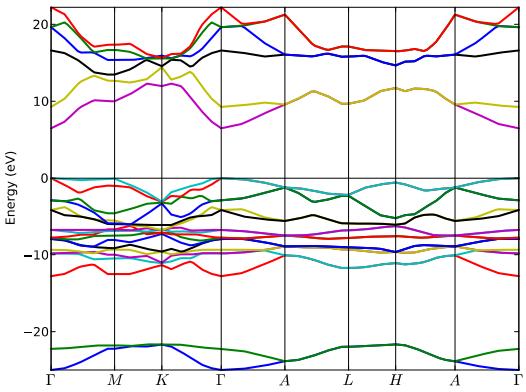

(c) P = 183.2 GPa

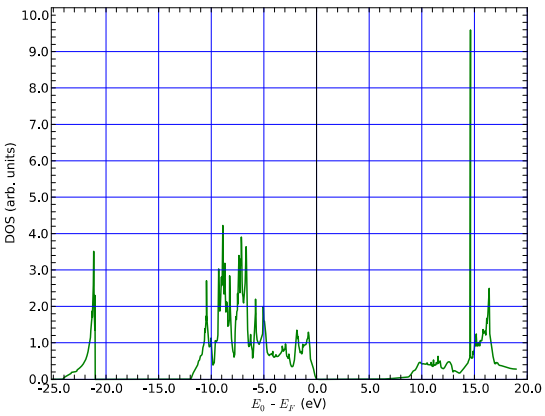

(d) P = 183.2 GPa

Figure A.3: The interpolated GW_0 band structure and total density of states for ZnO in the hexagonal $B8_1$ structure under transition pressure $P_T(B4 \rightarrow B8_1) = 19.5$ GPa and $P_T(B8_1 \rightarrow B2) = 183.2$ GPa. The valence band maximum is placed at 0 eV in each case.

The band structure plots on Fig. A.3 shows that the hexagonal $B8_1$ structure induced from the B4 phase, could be a direct gap insulator with a band gap of 3.15 eV. This energy gap is further increased to 6.46 eV upon transformation to the high-pressure B2 phase. As in the B_h structure (Fig. A.2), the total density of states in the valence band significantly shift to lower energies. However, the main Zn $3d$ peaks in the upper valence band are greatly reduced in height and appears to be completely hybridized with the O $2p$ states.

Appendix B

Crystal Structures of ZnO

The unit cell crystal structures for the different polymorphs of ZnO considered in this work are shown in Figures B.1 - B.3. All structures were visualized using VESTA structure visualization software [154]. In reality, the crystal structures observed for ZnO are the wurtzite (B4), zinc blende (B3), and rocksalt (B1) as shown in Figure B.1. Under ambient conditions, the wurtzite structure is the most thermodynamically stable phase as discussed in chapter 6, and has a hexagonal unit cell with the basal plane lattice parameter a and axial lattice parameter c in the ratio $c/a = 1.633$ for the ideal structure. Its symmetry is given by the space group $P6_3mc$ in the Hermann-Mauguin notation [155]. Each Zn atom in the wurtzite structure is coordinated by 4 O atoms, and vice versa. The structure is built from two interpenetrating hexagonal close-packed (hcp) sublattices displaced with respect to each other along the c axis by an amount $u = 3/8 = 0.375$ (in the ideal wurtzite structure). The internal parameter u is defined as the length of the anion-cation bond parallel to the c-axis (or the nearest-neighbor distance) divided by the c lattice parameter. In a real ZnO crystal, the wurtzite structure deviates from the ideal arrangement, by changing the c/a ratio or the u value [156].

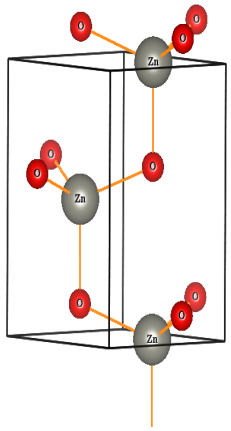

(a) Wurtzite (B4)

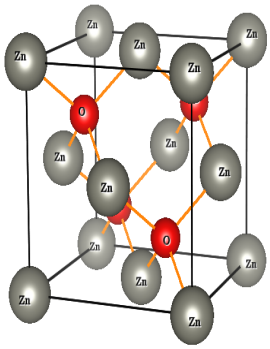

(b) Zinc blende (B3)

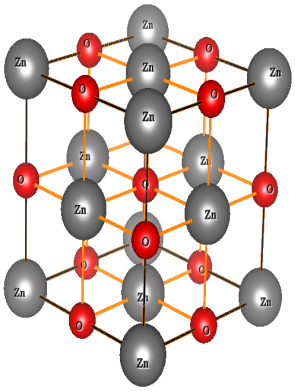

(c) Rocksalt (B1)

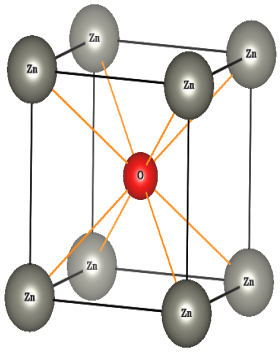

(d) Cesium chloride (B2)

Figure B.1: Stick-and-ball representation of ZnO crystal structures in the (a) hexagonal wurtzite (B4), (b) cubic zinc blende (B3), (c) cubic rocksalt (B1) and (d) cubic cesium chloride (B2) phases. Gray large spheres denote Zn atoms while the red small spheres denote O atoms.

The zinc blende (B3) structure shown on Figure B.1(b), is a cubic analog of the wurtzite structure. Its symmetry belongs to the space group $F\bar{4}3m$ and is comprised of two interpenetrating face-centered cubic (fcc) sublattices shifted along the body diagonal by a quarter of the length of body the diagonal. As in the wurtzite structure, all the atoms in the zinc blende structure have tetrahedral coordination, i.e. each atom's nearest neighbors are four atoms of the opposite type. The 4 nearest neighbors and 12 second-nearest neighbors have the same bond distance in both the wurtzite and zinc blende structures.

The wurtzite ZnO structure has been shown to transform to the rocksalt (B1) structure at external hydrostatic pressures around 10 GPa. The rocksalt structure (Figure B.1(c)) of space group $Fm\bar{3}m$, can be represented as an fcc lattice with a two-atom basis or as two interpenetrating face-centered cubic lattices. The Zn atom is located at each lattice point, and the O atom is located half way between lattice points along the fcc unit cell edge. The coordination number of the atoms in the rocksalt structure is 6, i.e. each O atom is octahedrally coordinated by 6 Zn atoms and vice versa.

The hypothetical cesium chloride structure, CsCl (B2), being the most favorable high pressure phase is based on a simple cubic lattice. The unit cell of B2 phase of ZnO Figure B.1(d) is a simple cube with a Zn ion at each of the corners and O ion at the center. The symmetry of this structure is given by the space group $Pm\bar{3}m$ in Hermann–Mauguin notation. The O ion at the center of the cube is surrounded by eight Zn ions at the corners. Similarly, the Zn ions at the corners of the cube are coordinated to eight O ions at the centers of each of the surrounding cubes. The CsCl structure therefore has an atomic coordination number of 8.

In Figure B.2, we show four more hexagonal modifications of ZnO considered in

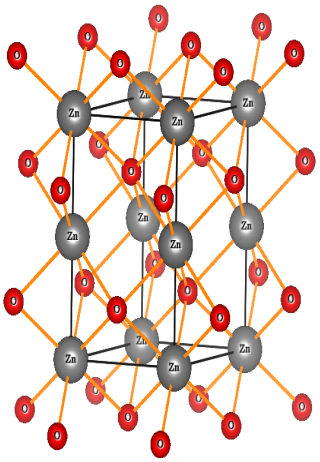

(a) NiAs structure

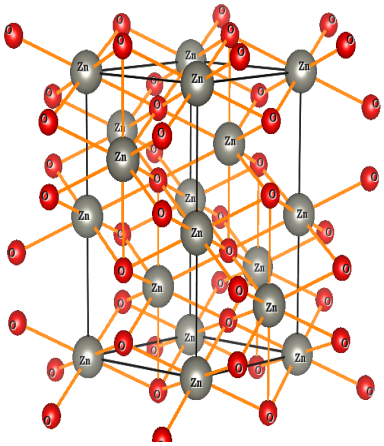

(b) AsTi structure

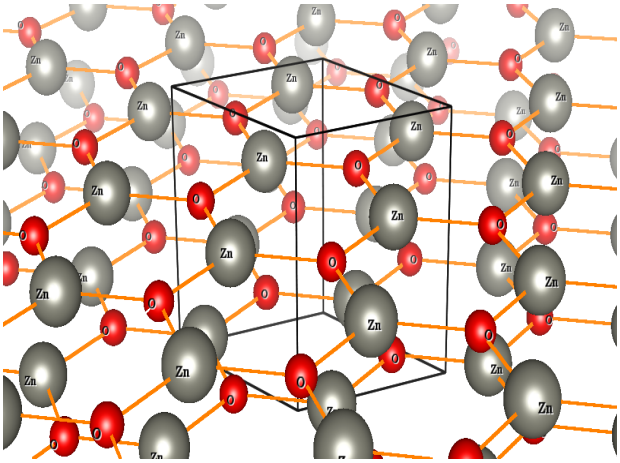

(c) BN structure

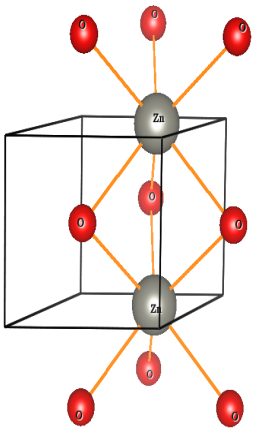

(d) WC structure

Figure B.2: Stick-and-ball representation of ZnO crystals in the hexagonal (a) NiAs-type ($B8_1$), (b) AsTi-type (B_i), (c) BN-type (B_k) and (d) WC-type (B_h) structures. Gray large spheres denote Zn atoms while the red small spheres denote O atoms.

this work. The NiAs ($B8_1$), AsTi (B_i), and BN (B_k) prototypes belong to the same Hermann–Mauguin space group $P6_3/mmc$, while the WC (B_h) prototype belongs to the space group $P\bar{6}m2$. By contrast with the hexagonal wurtzite structure in which the anions and cations are both tetrahedrally coordinated, the local coordination of the Zn O atoms on the NiAs-type structure (Fig. B.2(a)) is different. There are 6 Zn atoms (gray) arranged in a trigonal prism around the central O atom (red), while there are 6 O atoms octahedrally arranged around the Zn atom.

The AsTi-type structure shown on Figure B.2(b), is similar to the NiAs, except that the local coordination of anions and cations is the same. That is, in the AsTi modification of ZnO, there are 6 Zn atoms octahedrally arranged around the O atoms, and vice versa. In the hexagonal BN-type structure (B.2(c)) the Zn and O atoms are three-fold coordinated. The 3 Zn atoms are arranged in a triangular layer around a central O atom. Similarly, 3 O atoms are arranged in a triangle around a Zn atom.

The hexagonal WC-type structure of ZnO is shown on Figure B.2(d). The atomic coordination in this structure is also six-fold, as in the NiAs and AsTi structures. However, both the Zn and O atoms are trigonal prismatic, i.e. the Zn atom is located at the center of a trigonal prism formed by O atoms and vice versa.

Finally, Figure B.3 shows modifications of ZnO in the tetragonal PbO-type and cubic NaTl-type structures. The NaTl (B32) structure belongs to the space group $Fd\bar{3}m$, same as for the diamond structure. The fcc unit-cell of this NaTl-type structure uniquely consists of eight small cubes, alternatively centered either with Zn or O atoms. Each of these centered sites has eight nearest neighbors: four like and four unlike. The Zn and O atoms lie on diamond sublattices, which are separated by a quarter of the body diagonal of the unit cell [157]. More details including the crystallographic vectors and basis for the prototypes of these structures can be obtained at

(a) PbO (B10)

(b) NaTl (B32)

Figure B.3: Stick-and-ball representation of ZnO crystal in the tetragonal PbO-type ($B10$) and cubic NaTl-type (B32) structures. Gray large spheres denote Zn atoms while the red small spheres denote O atoms.

the Crystal Lattice Structures Web page, http://cst-www.nrl.navy.mil/lattice/, provided by the Center for Computational Materials Science of the United States Naval Research Laboratory.

Bibliography

[1] M. C. Payne, M. P. Teter, D. C. Allan, T. A. Arias, J. D. Joannopoulos, *Rev. Mod. Phys* **64**, 1045 (1992).

[2] R. M. Martin, Physics of matter at high pressure (and temperature) - theoretical perspectives (2008). Lecture notes presented for participants of the African School on Electronic Structure Methods and Applications (ASESMA2008), held at Cape Town - South Africa.

[3] J. E. Jaffe, J. A. Synder, Z. Lin, A. C. Hess, *Phys. Rev. B* **62**, 1660 (2000).

[4] A. Seko, F. Oba, A. Kuwabara, I. Tanaka, *Phys. Rev. B* **72**, 024107 (2005).

[5] D. Kasinathan, Computational study of materials under presure, Ph.D. thesis, University of California Davis (2006).

[6] J. Uddin, G. E. Scuseria, *Phys. Rev. B* **74**, 245115 (2006).

[7] Y. Saeed, A. Shaukat, N. Ikram, M. Tanveer, *J. Phys. Chem. Solids* **69**, 1676 (2008).

[8] L. J. Sham, M. Schlüter, *Phys. Rev. Lett.* **51**, 1888 (1983).

[9] A. D. Becke, *J. Chem. Phys.* **98**, 1372 (1993).

[10] R. G. Parr, W. Yang, *Density Functional Theory of Atoms and Molecules* (Oxford University Press, New York, 1989).

[11] D. Joubert, ed., *Density Functionals: Theory and Applications* (Springer, 1998).

[12] L. H. Thomas, *Proc. Cambrige Phil. Roy. Soc* **23**, 542 (1927).

[13] E. Fermi, *Z. Phys.* **48** (1928).

[14] P. A. M. Dirac, *Proc. Cambridge Phil. Roy. Soc.* **26**, 376 (1930).

[15] R. M. Martin, *Electronic Structure Basic Theory and Practical Methods* (Cambridge University Press, 2004).

[16] P. Hohenberg, W. Kohn, *Phys. Rev.* **136**, B864 (1964).

[17] W. Koch, M. C. Holthausen, *A Chemist's Guide to Density Functional Theory* (Wiley-VCH New York, 2001), second edn.

[18] M. Levy, *Phys. Rev. A* **26**, 1200 (1982).

[19] E. H. Lieb, *Physics as Natural Philosophy: Essays in honor of Laszlo Tisza on his 75th Birthday* p. 111 (1982).

[20] W. Kohn, L. J. Sham, *Phys. Rev* **140**, A1133 (1965).

[21] J. F. Dobson, G. Vignale, M. P. Das, eds., *Electronic Density Functional Theory, Recent Progress and New Directions* (Plenum Press, New York, 1998).

[22] R. M. Dreizler, E. K. U. Gross, *Density Functional Theory: An Approach to the Quantum Many-Body Problem* (Springer-Verlag, 1990).

[23] R. O. Jones, O. Gunnarson, *Rev. Mod. Phys.* **61**, 689 (1989).

[24] D. M. Ceperly, B. J. Alder, *Phys. Rev. Lett* **45**, 566 (1980).

[25] G. P. Srivastava, *Theoretical Modelling of Semiconductor Surfaces: Microscopic Studies of Electrons and Phonons* (World Scientific, Singapore, 1999).

[26] J. M. Seminario, *Modern Density Functional Theory: A Tool for Chemistry* (ELSEVIER, 1995).

[27] J. P. Perdew, Y. Wang, *Phys. Rev. B* **45**, 13244 (1992).

[28] J. P. Perdew, *Phys. Rev. B* **33**, 8822 (1986).

[29] J. P. Perdew, Y. Wang, *Phys. Rev. B* **33**, 8800 (1986).

[30] S. Kurth, J. P. Perdew, P. Blaha, *Int. J. Quantum Chem.* **75**, 889 (1999).

[31] J. Perdew, K. Burke, Y. Wang, *Phys. Rev. B* **54**, 16533 (1996).

[32] E. Engel, S. H. Vosko, *Phys. Rev. B* **47**, 13164 (1993).

[33] G. Ortiz, *Phys. Rev. B* **45**, 11328 (1992).

[34] S. Moroni, D. M. Ceperly, G. Senatore, *Phys. Rev. Lett* **75**, 689 (1995).

[35] J. P. Perdew, K. Burke, M. Ernzerhof, *Phys. Rev. Lett.* **77**, 3865 (1996).

[36] J. P. Perdew, *Electronic Structure of Solids* (Akademie Verlag, Berlin, 1991).

[37] J. Hafner, *J. Comput. Chem.* **29**, 2044 (2008).

[38] O. Gunnarsson, B. I. Lundqvist, *Phys. Rev. B* **13**, 4274 (1976).

[39] D. C. Langreth, J. P. Perdew, *J. Phys. F: Met. Phys.* **15**, 2884 (1977).

[40] J. Harris, *Phys. Rev. A* **29**, 1648 (1984).

[41] A. D. Becke, *J. Chem. Phys.* **88**, 1053 (1988).

[42] A. D. Becke, *J. Chem. Phys.* **98**, 5648 (1993).

[43] A. D. Becke, *Phys. Rev. A* **38**, 3098 (1988).

[44] P. M. W. Gill, B. G. Johnson, J. A. Pople, M. J. Frisch, *Int. J. Quantum Chem. Quantum Chem. Symp.* **26**, 319 (1992).

[45] C. Lee, W. Yang, R. G. Parr, *Phys. Rev. B* **37**, 785 (1988).

[46] P. J. Stevens, F. J. Devlin, C. F. Chablowski, M. J. Frisch, *J. Phys. Chem.* **98**, 11623 (1994).

[47] J. Paier, M. Marsman, G. Kresse, *J Chem Phys* **127**, 024103 (2007).

[48] S. H. Vosko, L. Wilk, M. Nusair, *Can. J. Phys* **58**, 1200 (1980).

[49] M. Ernzerhof, *Chem. Phys. Lett* **263**, 499p (1996).

[50] M. Ernzerhof, J. P. Perdew, K. Burke, *Int. J. Quantum Chem.* **64**, 285 (1996).

[51] J. P. Perdew, M. Ernzerhof, K. Burke, *J. Chem. Phys.* **105**, 9982 (1996).

[52] M. Ernzerhof, G. E. Scuseria, *J. Chem. Phys.* **110**, 5029 (1999).

[53] C. Adamo, V. Barone, *J. Chem. Phys.* **110**, 6158 (1999).

[54] J. Heyd, G. E. Scuseria, *J, Chem. Phys.* **118**, 8207 (2003).

[55] J. Heyd, G. E. Scuseria, M. Ernzherof, *J. Chem. Phys.* **124**, 219906 (2006).

[56] J. Paier, R. Hirschl, M. Marsman, G. Kresse, *J. Chem. Phys.* **122**, 234102 (2005).

[57] J. Paier, M. Marsman, K. Hummer, G. Kresse, *J Chem Phys* **124**, 154709 (2006).

[58] F. Gygi, A. Baldereschi, *Phys. Rev. B* **34**, 4405 (1986).

[59] V. N. Staroverov, G. E. Scuceria, J. Tao, J. P. Perdew, *J. Chem. Phys.* **119**, 12129 (2003).

[60] J. Jaramillo, G. E. Scuseria, M. Ernzerhof, *J. Chem. Phys.* **118**, 1068 (2003).

[61] J. Heyd, G. E. Scuseria, *J. Chem. Phys.* **121**, 1187 (2004).

[62] A. V. Krukau, O. A. Vydrov, A. F. Izmaylov, G. E. Scuseria, *J. Chem. Phys.* **125**, 224106 (2006).

[63] J. Heyd, J. E. Peralta, G. E. Scuseria, R. L. Martin, *J. Chem. Phys.* **123**, 174101 (2005).

[64] M. Marsman, J. Paier, A. Stroppa, G. Kresse, *J. Phys.: Condens. Matter* **20**, 064201 (2008).

[65] J. Paier, M. Marsman, G. Kresse, *Phys. Rev. B* **78**, 121201 (R) (2008).

[66] J. Wrobel, K. J. Kurzydlowski, K. Hummer, G. Kresse, J. Piechota, *Phys. Rev. B* **80**, 155124 (2009).

[67] J. Kohanoff, *Electronic Structure Calculations for Solids and Molecules* (Cambridge University Press, 2006).

[68] K. Schwarz, *International Tables for Crystallography* (2006), vol. D, chap. 2.2, pp. 294–313.

[69] H. J. Monkhorst, J. D. Pack, *Phys. Rev. B* **13**, 5188 (1976).

[70] D. R. Hamann, M. Schlüter, C. Chiang, *Phys. Rev. Lett.* **43**, 1494 (1979).

[71] P. E. Blöchl, *Phys. Rev. B* **41**, 5414 (1990).

[72] G. B. Bachelet, D. R. Hamann, M. Schluter, *Phys. Rev. B* **26**, 4199 (1982).

[73] N. Troullier, J. L. Martins, *Phys. Rev. B* **43**, 1993 (1991).

[74] A. M. Rappe, J. D. Joannopolous, *Computer Simulation in Materials Science* (Dordrecht: Kluwer, 1991).

[75] J. S. Lin, A. Qteish, M. C. Payne, V. Heine, *Phys. Rev. B* **47**, 4174 (1993).

[76] D. Vanderbilt, *Phys. Rev. B* **41**, 7892 (1990).

[77] K. Laasonen, A. Pasquarello, R. Car, C. Lee, D. Vanderbilt, *Phys. Rev. B* **47**, 10142 (1993).

[78] D. J. Singh, L. Nordstrom, eds., *Planewaves, Pseudopotentials, and the LAPW Method* (Springer, 2006), second edn.

[79] O. K. Andersen, *Phys. Rev. B* **12**, 3060 (1975).

[80] G. Kresse, D. Joubert, *Phys. Rev. B* **59**, 1758 (1999).

[81] P. E. Blöchl, *Phys. Rev. B* **50**, 17953 (1994).

[82] P. E. Blöchl, J. Kästner, C. J. Först, *arXiv:cond-mat* **1**, 0407205 (2004).

[83] *VASP User Guide*, http://cms.mpi.univie.ac.at/vasp/vasp/vasp.html.

[84] G. Kresse, J. Hafner, *J. Phys.: Condens. Matter* **6**, 8245 (1994).

[85] J. K. Dewhurst, Computer modelling of superhard metal dioxides, Ph.D. thesis, Faculty of Science, University of the Witwatersrand (1999).

[86] P. Vinet, J. H. Rose, J. Ferrante, J. R. Smith, *J. Phys.: Condens. Matter* **1**, 1941 (1989).

[87] F. D. Murnaghan, *American Journal of Mathematics* **59**, 235 (1937).

[88] F. Birch, *Phys. Rev.* **71**, 809 (1947).

[89] S. Desgreniers, *Phys. Rev. B* **58**, 14102 (1998).

[90] M. P. Marder, *Condensed Matter Physics* (John Wiley and Sons, 2000).

[91] K. Umemoto, R. M. Wentzcovitch, P. B. Allen, *Science* **311**, 983 (2006).

[92] N. D. Spencer, J. H. Moore, *Encyclopedia of Chemical Physics and Physical Chemistry* (Taylor and Francis, 2001).

[93] S. Adachi, *Properties of Group - Iv, Iii-V and Ii-Vi Semiconductors* (John Wiley and Sons, 2005).

[94] C. Fiolhais, F. Nogueira, M. Marques, eds., *A Primer in Density Functional Theory*, Lecture Notes in Physics (Springer-Verlag Berlin Heidelberg, 2003).

[95] J. P. Perdew, R. G. Parr, M. Levy, J. L. Balduz, *Phys. Rev. Lett.* **49**, 1691 (1982).

[96] W. Knorr, R. W. Godby, *Phys. Rev. B* **50**, 1779 (1994).

[97] W. Knorr, R. W. Godby, *Phys. Rev. Lett.* **65**, 639 (1992).

[98] R. S. Mulliken, *J. Chem. Phys.* **23**, 1833 (1995).

[99] R. F. W. Bader, *Atoms in Molecules - A Quantum Theory* (Oxford University Press, Oxford, UK, 1990).

[100] R. F. W. Bader, *Can. J. Chem.* **76(7)**, 1082 (1998).

[101] N. Bork, N. Bonanos, J. Rossmeisl, T. Vegge, *J. Appl. Phys.* **109**, 033702 (2011).

[102] L. J. Sham, W. Kohn, *Phys. Rev.* **145**, 561 (1966).

[103] M. S. Hybertsen, S. G. Louie, *Phys. Rev. B* **34**, 5390 (1986).

[104] M. S. Hybertsen, S. G. Louie, *Phys. Rev. Lett.* **55**, 1418 (1985).

[105] R. W. Godby, M. Schlüter, L. J. Sham, *Phys. Rev. B* **35**, 4180 (1987).

[106] R. W. Godby, M. Schlüter, L. J. Sham, *Phys. Rev. Lett.* **56**, 2415 (1986).

[107] L. Hedin, *Phys. Rev.* **139**, A796 (1965).

[108] M. Shishkin, G. Kresse, *Phys. Rev. B* **74**, 035101 (2006).

[109] U. von Barth, *Phys. Rev. B* **54**, 8411 (1996).

[110] E. L. Shirley, *Phys. Rev. B* **54**, 7758 (1996).

[111] A. Fetter, J. D. Walecka, *Quantum Theory of Many-Particle Systems* (Dover Publications, Mineola, 2003).

[112] J. Solyom, *Fundamentals of the Physics of Solids: Normal, Broken-Symmetry, and Correlated Systems* (Springer, 2011), vol. 3, chap. 29, pp. 61–80.

[113] M. Shishkin, G. Kresse, *Phys. Rev. Lett.* **99**, 246403 (2007).

[114] M. Shishkin, G. Kresse, *Phys. Rev. B* **75**, 235102 (2007).

[115] M. van Schilfgaarde, T. Kotani, S. Faleev, *Phys. Rev. Lett.* **96**, 226402 (2006).

[116] C. H. Bates, W. B. White, R. Roy, *Science* **137**, 993 (1962).

[117] H. Karzel, *et al.*, *Phys. Rev. B* **53**, 11425 (1996).

[118] H. Liu, J. Tse, H. Mao, *J. Appl. Phys.* **100**, 093509 (2006).

[119] A. Zaoui, W. Sekkal, *Phys. Rev. B* **66**, 174106 (2002).

[120] Y. Azzaz, S. Kacimi, A. Zaoui, B. Bouhafs, *Physica B* **403**, 3154 (2008).

[121] Z. Li, Y. Xu, G. Gao, T. Cui, Y. Ma, *Phys. Rev. B* **79** (2009).

[122] L. Gerward, J. S. Olsen, *J. Synchroton Radiat.* **2**, 233 (1995).

[123] J. Wrobel, J. Piechota, *Phys. Stat. Sol. (b)* **244**, 1538 (2007).

[124] R. J. Guerrero-Moreno, N. Takeuchi, *Phys. Rev. B* **66**, 205205 (2002).

[125] A. Schleife, F. Fuchs, J. Furthmuller, F. Bechstedt, *Phys. Rev. B* **73**, 245212 (2006).

[126] J. E. Jaffe, A. C. Hess, *Phys. Rev. B* **48**, 7903 (1993).

[127] B. Meyer, D. Marx, *Phys. Rev. B* **67**, 035403 (2003).

[128] H. Liu, *et al.*, *Phys. Rev. B* **70**, 094114 (2004).

[129] S. Limpijumnong, S. Jungthawan, *Phys. Rev. B* **70**, 054104 (2004).

[130] B. Amrani, I. Chiboub, S. Hiadsi, T. Benmessabih, N. Hamdadou, *Solid State Commun.* **137**, 395 (2006).

[131] S. Cui, W. Feng, H. Hu, Z. Feng, Y. Wang, *J. Alloys Compd.* **476**, 306 (2009). Doi: 10.1016/j.jallcom.2008.08.052.

[132] A. Mang, K. Reimann, S. Rubenacke, *Solid State Commun.* **94**, 251 (1995).

[133] A. Segura, J. A. Sans, F. J. Manjon, A. Munoz, M. J. Herrera-Cabrera, *Appl. Phys. Lett.* **83**, 278 (2003).

[134] P. Schroer, P. Kruger, J. Pollman, *Phys. Rev. B* **49**, 17092 (1994).

[135] H. Dixit, R. Saniz, D. Lamoen, B. Partoens, *J. Phys.: Condens. Matter* **22**, 125505 (2010).

[136] A. B. M. A. Ashrafi, *et al.*, *Appl. Phys. Lett.* **76**, 550 (2000).

[137] L. Ley, R. A. Pollack, F. R. McFeely, S. P. Kowalczyk, D. A. Shirley, *Phys. Rev. B* **9**, 600 (1974).

[138] W. Gopel, J. Pollmann, I. Ivanov, B. Reihl, *Phys. Rev. B* **26**, 3144 (1982).

[139] D. Vogel, P. Krüger, J. Pollman, *Phys. Rev. B* **52**, R14316 (1995).

[140] T. Kotani, M. van Schilfgaarde, S. V. Falleev, *Phys. Rev. B* **76**, 165106 (2007).

[141] M. Usuda, N. Hamada, *Phys. Rev. B* **66**, 125101 (2002).

[142] H. Dixit, R. Saniz, D. Lamoen, B. Partoens, *Computer Physics Communications* **Article in press** (2011).

[143] B.-C. Shih, Y. Xue, P. Zhang, *Phys. Rev. Lett.* **105**, 146401 (2010).

[144] F. Fuchs, J. Furthmuller, F. Bechstedt, M. Shishkin, G. Kresse, *Phys. Rev. B* **76**, 115109 (2007).

[145] C. Friedrich, M. C. Müller, S. Blügel, *Phys. Rev. B* **83**, 081101(R) (2011).

[146] A. Ashrafi, C. Jagadish, *J. Appl. Phys.* **102**, 071101 (2007).

[147] S.-H. Wei, A. Zunger, *Phys. Rev. B* **37**, 8958 (1988).

[148] M. Oshikiri, F. Aryasetiawan, *Phys. Rev. B* **60**, 10754 (1999).

[149] M. Oshikiri, F. Aryasetiawan, *Jpn. J. Phys. Soc* **69**, 2113 (2000).

[150] F. Oba, A. Togo, I. Tanaka, J. Paier, G. Kresse, *Phys. Rev. B* **77**, 245202 (2008).

[151] S. Park, B. Lee, S. H. Jeon, S. Han, *Curr. Appl. Phys.* **11**, S337 (2011).

[152] J. Furthmüller, P. H. Hahn, F. Fuchs, F. Bechstedt, *Phys. Rev. B* **72**, 205106 (2005).

[153] C. Kittel, *Introduction to solid state physics* (John Wiley & Sons, 2005).

[154] K. Momma, F. Izumi, *J. Appl. Crystallogr.* **44**, 1272 (2011).

[155] T. Hahn, ed., *International Tables for Crystallography* (Dordrecht: Kluwer Academic, 1989). BRIEF TEACHING EDITION OF VOLUME A, SPACE-GROUP SYMMETRY. EDITED BY THEO HAHN. PUBLISHED FOR THE INTERNATIONAL UNION OF CRYSTALLOGRAPHY BY KLUWER ACADEMIC.

[156] H. Morkoç, Ümit Özgür, *Zinc Oxide: Fundamentals, Materials and Device Technology* (WILEY-VCH Verlag GmbH & Co. KGaA, 2009).

[157] T. F. Fassler, ed., *Zintl Phases: Principles and Recent Developments* (Springer-Verlag, Berlin Heidelberg, 2011).